CHARLES UNIVERSITY

and

HASSELT UNIVERSITY / tUL

Doctoral dissertation

Collagen structures from cell culture to intact tendon

Author: Daniel Hadraba

Promoters: Assoc. Prof. Karel Jelen | Charles University
Prof. Marcel Ameloot | Hasselt University

Co-promoters: Dr. Frantisek Lopot | Charles University
Prof. Virginie Bito | Hasselt University

CHARLES UNIVERSITY

and

HASSELT UNIVERSITY / MASSTRICHT UNIVERSITY

TRANSNATIONAL UNIVERSITY LIMBURG

Doctoral dissertation

Collagen structures from cell culture to intact tendon

Doctoral dissertation submitted to obtain the degrees of

Doctor of Biomechanics at Charles University

Doctor of Biomedical Sciences at Hasselt University / tUL

Annotation list

Author:	Ing. Mgr. Daniel Hadraba
Doctoral thesis title:	Collagen structures from cell culture to intact tendon
Year:	2010 – 2017
Doctoral program:	Doctor of Biomechanics at Charles University Doctor of Biomedical Science at Hasselt University / transnational University Limburg
Departments:	Dept. Anatomy and Biomechanics | Faculty of Physical Education and Sport | Charles University Dept. Biophysics | Hasselt University
Promoters:	Assoc. Prof. Karel Jelen | Dept. Anatomy and Biomechanics | Faculty of Physical Education and Sport | Charles University Prof. Marcel Ameloot | Hasselt University / transnational University Limburg
Co-promoters:	Dr. Frantisek Lopot | Dept. Anatomy and Biomechanics | Faculty of Physical Education and Sport | Charles University Prof. Virginie Bito | Hasselt University / transnational University Limburg
Bibliography details:	Pages 102 Figures 30 Tables 2 Equations 17
Keywords:	tendon, collagen, crimps, orientation, aging, label-free microscopy, second harmonic generation, fluorescence lifetime imaging microscopy, and biomechanics

Preface

Biomechanics applies interdisciplinary tools to explore biological systems. These systems are often based on hierarchical units that create an organization of great complexity. Frequently, to describe the complexity, a global perspective is the solution. Then any discipline, not only biology or mechanics, can contribute to the knowledge. Therefore, examining the problem from different angles and at different scales, not forgetting the context, often brings the answer to the hypotheses. Finally, one should never neglect any information or ignore any opinions. However, the interpretation should be treated with critical thinking and ethical qualities.

The contribution of this thesis comprise the investigation on type I collagen from its synthesis *in vitro* to its multi-hierarchical function in connective tissue. The investigations were mainly conducted by using the label-free microscopy methods, for instance, second harmonic generation, polarized second harmonic generation or fluorescence lifetime imaging, which all have a strong potential for *in vivo* imaging with subcellular resolution. In Chapter 1, we summarize the knowledge on collagen synthesis and a role of collagen in tendon. We also introduce the most common methods for collagen visualisation and give a brief overview of collagen mechanical properties. In Chapter 2, we establish the methods for quantitative and qualitative collagen identification *in vitro*. In Chapter 3, we clarify the impact of sample fluorescent immunostaining to collagenous structures in microtome sections and compare it with the label-free microscopy methods. In Chapter 4, we introduce an objective automatic analysis for returning the collagen fibre orientation regularity from a single microtome section image. In Chapter 5, we examine the intact tendon samples and development of the crimp pattern with age. In Chapter 6, the response of crimps to mechanical loading is measured in intact tendon samples. In addition to that, we measure the change in the helical pitch angle for load-free and stretched intact tendon samples as well as the amount of cross-linkers in tendon. For this purpose, we designed a miniaturized uniaxial tensile testing device that enables to conduct mechanical tests and microscopy simultaneously. Finally, in Chapter 7, we summarize the most important results and offer further perspective on the connective tissue topic.

Author's declaration

I hereby declare that this doctoral thesis is my independent original work. Completing this doctoral thesis, I have been advised by or cooperated with the individuals mentioned in Acknowledgements and used the referenced literature.

I also authorize the above mentioned institutions to lend this thesis to other institutions or individuals for the purpose of academic research.

Prague 20th January 2017 Daniel Hadraba

Acknowledgement

I would like to thank to my promoters Assoc. Prof. Karel Jelen and Prof. Marcel Ameloot and co-promoters Dr. František Lopot and Prof. Virginie Bito for the critical mentoring. I also have to thank to my current leader, Dr. Jiří Janáček - department of Biomathematics, for supporting and mentoring me in the fields of signal processing and geometry. I also want to thank to all my colleagues at Charles University, Hasselt University, Czech Technical University, and the Institute of Physiology, the Czech Academy of Sciences for inspiring me. This work would not be possible without the support of The Charles University Grant Agency no. 956213 and the support by the Flemish government and Hasselt University.

Table of content

Table of content

List of Figures

List of Tables

List of Equations

List of Abbreviations

AA	ascorbic acid
AGEs	advanced glycation end products
AOBS	acousto-optical beam splitter
BD	backward direction
CARS	coherent anti-Stokes Raman scattering
CCD	charge-coupled device
CMOS	complementary metal–oxide–semiconductor
CSA	cross-sectional area
CT	computed tomography
DNA	deoxyribonucleic acid
DNEM	Dulbecco's Modified Eagle Medium
ECM	extracellular matrix
FD	forward direction
FEM	finite element method
FFT	Fast Fourier Transform
FLIM	fluorescence-lifetime imaging microscopy
FWHM	full width at half maximum
GAGs	glycosaminoglycans
Gly	glycine
HP	hydroxylysyl pyridinoline
HPA	helical pitch angle
HSV	hue-saturation-value colour scheme
HWP	half wave-plate
IS	immunostaining
IR	infrared
LP	lysyl pyridinoline
MMP	matrix metalloproteinase
MPD	mean percentage difference
MRI	magnetic resonance imaging

NA	numerical aperture
NDD	non-descanned direction
PBS	phosphate-buffered saline
PCR	polymerase chain reaction
PMT	photomultiplier tube
PSHG	polarized second harmonic generation
QWP	quarter wave-plate
RGB	red-green-blue colour scheme
RNA	ribonucleic acid
SEM	scanning electron microscope
SHG	second harmonic generation
TEM	transmission electron microscopy
TPEF	two-photon excitation fluorescence
TPEM	two-photon excitation fluorescence microscopy
TTI	tester tensile instrument
VIC	cardiac valve interstitial cells

List of Symbols

$\boldsymbol{P}$	dielectric polarization density
$\boldsymbol{E}$	electromagnetic field
$\boldsymbol{\omega}$	frequency
$\boldsymbol{\varepsilon}$	permittivity
$\boldsymbol{\chi}$	electric susceptibility
$\boldsymbol{\pi}$	irrational mathematical constant
$\boldsymbol{\Phi}$	orientation angle of fibre
$\boldsymbol{\theta}$	helical pitch angle
$\boldsymbol{\alpha}$	incident beam polarization angle
$\boldsymbol{\lambda}$	electromagnetic wave wavelength
A	crimp amplitude

List of Symbols

Λ	crimp wavelength
τ	fluorescence lifetime

Chapter 1

1 Introduction

1.1 Collagen

1.1.1 Historical overview

There are not many proteins that affect the biomechanical properties of structures in vertebrates as much as fibrillar collagen[1]. Therefore, collagen usage as medical sutures is dated about 5,000 years ago, and since that, its structure and utilization have been studied in multiple directions[2]. The modern history of discovery starts with introducing collagen in histological papers in the nineteen century. At that time, glue [kola in Greek] was produced [genos in Latin] by boiling animal hide for engineering applications[3]. Since the adhesive gelatine earned its name, several fields, for instance leather industry or biochemistry, have worked on revealing its structural composition and properties.

Early studies reported data on collagen solubility and hydrolysis products[2]. It soon led to the results which revealed some basics of the multi-hierarchical fibrous assembly. In the early years of the 20th century, X-ray diffraction started serving as a powerful analytical tool. On biological materials, the technique was pioneered by the Herzog's group. Their measured the diffraction patterns of cellulose fibres, wool, and silk[4,5]. The knowledge progressed with the Astbury's (1930s) study on hair which published varying X-ray photographs for stretched and unstretched keratin fibres[4]. In 1940, Astbury and Bell proposed the presence of amino acid chain in collagen molecule[6]. Other significant contributions to collagen knowledge were made in the 1950s when Pauling and Corey described the collagen as a triple helical conformation that is held together by hydrogen bonds[5]. In 1954, the Ramachandran's group established the molecular model[7] by refining geometric isomerism, and in 1955, Rich and Crick published a marginally[7] refined structure that is accepted today[8]. Simultaneously the collagen molecular periodicity, symmetry, length, and other morphological features were observed with electron microscopy[2]. Furthermore, a number of reports were published on relatively slow metabolism of collagen[3]. In the 1960s, the studies continued with the collagen synthesis and investigation of the collagen polypeptide chains and cross-link formation[3]. This area opened the

investigation on collagen and its dysfunctions. These physiological and pathological conditions are related to severe disorders, for instance, Osteogenesis imperfecta, Ehlers-Danlos syndrome[9], or scurvy that are caused or pronounced by collagen abnormalities at any hierarchical level. In the 1970s, distinct types of collagen were first identified[2] in granulation tissue and skin. The discovered number of collagen types is still growing nowadays. In the 1980s, the amount of biomechanical studies on the hierarchical structure of collagen started increasing greatly. They targeted varying levels from tropocollagen monomers to fibers and tendons[6]. The studies have demonstrated a massive variation in the mechanical properties for different levels, types, and tissues[10]. Recent studies on collagen diverge massively and mainly concentrate on molecular and supramolecular structure[3]; synthesis, assembly[11,12], and stability[13]; multi-hierarchical biomechanics[10,11,14,15]; collagen types occurrence and ratio variations[16]; cross-linking[15,17] and cross-linkers[18]; and pathologies[19,20].

1.1.2 Intracellular collagen assembly

The collagen family includes molecules that consist of three polypeptide chains (α chain) that contain at least one Gly-X-Y repeat sequence per constituent chain[19] where X is usually proline (Pro) and Y is 5-hydroxyproline (Hyp). The variability in the polypeptide chains defines each of the 28 discovered collagen types. The collagen types are usually divided into subcategories by certain criteria. Type I collagen belongs to the fibril-forming category, although the type I collagen fibres often contain small portions of types III, V, and XII[19,21]. Type I collagen is heterotrimeric structure composed of two α1 chains and one α2 chain. Each chain contains about 1050 amino acids[22]. The assembly starts from nuclear transcription of type I collagen genes (COL1A1, COL1A2) into pre-mRNA. Then the pre-mRNA undergoes post-transcriptional modification, and the mature RNA is transported into the cytoplasm and translated into preprocollagen at the rough endoplasmatic reticulum[23]. In the endoplasmatic reticulum, the signal peptides are removed, and the procollagen chains are enzymatically modified in multiple steps. These steps include hydroxylation of proline (ascorbic acid required) and lysine residues and beginning of glycosylation of hydroxylysyl residues[24].

In the next stage, the fibrillar type I procollagen is transported through the Golgi complex, aggregated in the secretory vesicles and exported into the extracellular space (Fig. 1.1).

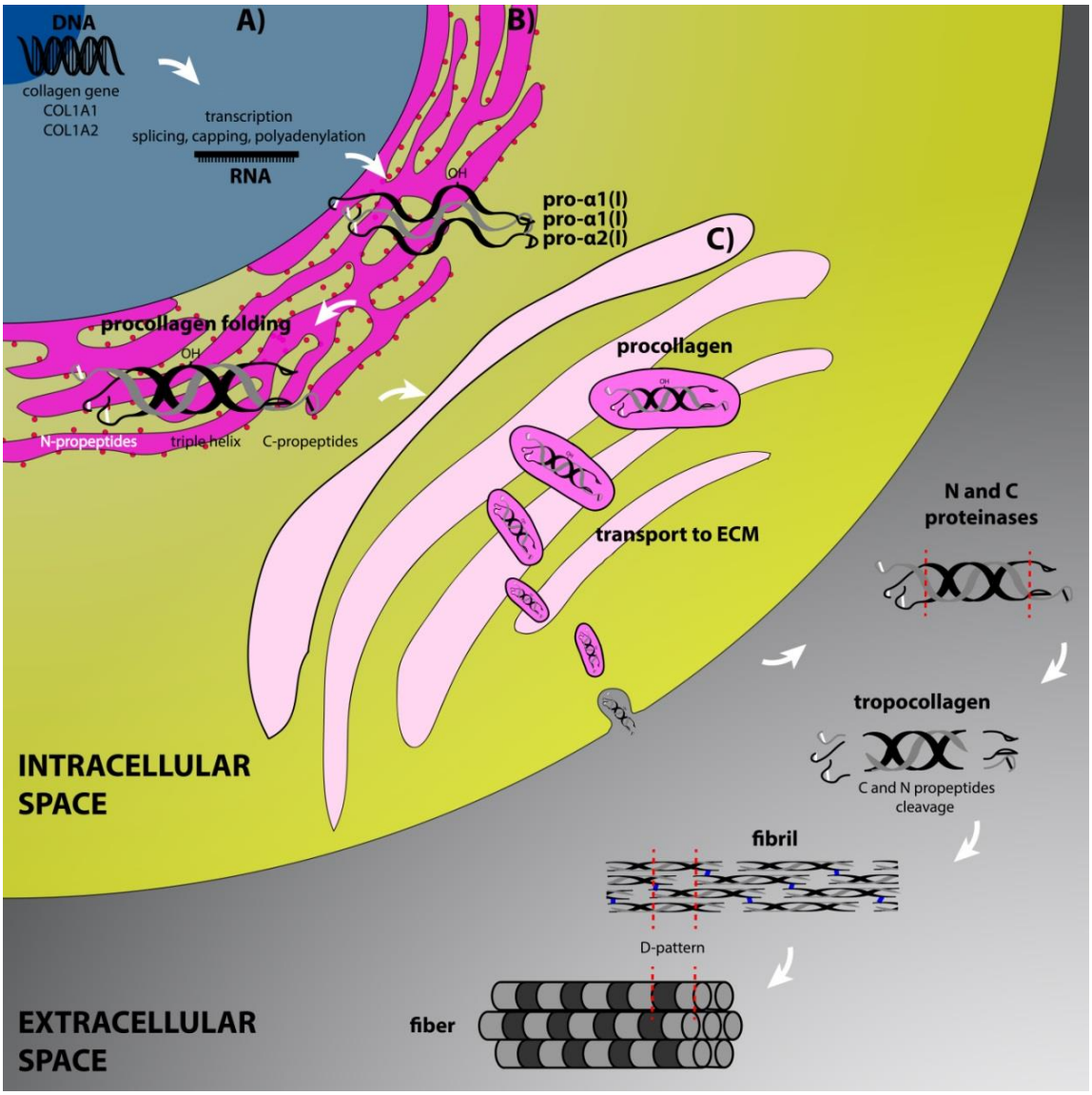

Fig. 1.1 Collagen intracellular and extracellular biosynthesis. The collagen biosynthesis is mostly studied on *in vitro* experiments. The self-assembly starts at **(A)** nucleus, and the regulation varies among the cell types[21]. The production is directly or indirectly controlled by growth factors, vitamins, hormones[23], mechanical forces, and other stimuli, but these mechanisms are not completely understood[25]. The procollagen assembly occurs in the **(B)** endoplasmic reticulum[26]. The triple helix is formed from three pro-α chains, where each chain includes the Gly-X-Y sequence repetition. After that, the procollagen helices enter the **(C)** Golgi, align side-by-side in parallel and form large aggregates[26]. There are several models that explain the extracellular assembly[21], however, the complete cascade and mechanisms are still unknown.

1.1.3 Extracellular collagen assembly

In the extracellular space, procollagen is undergoing its final translations such as the completion of the N and C propeptides cleavage[19], and formation of the collagen microfibrils with their typical 67nm periodic D-pattern[27]. The final stage involves the formation of fibrils, their supramolecular stabilization through the head-to-tail enzymatic cross-linking by lysyl oxidase and formation of type I collagen fibers[19,28]. The cross-linking prevents sliding of molecules under mechanical load[29]. For further reading about biosynthesis and molecular structure of collagen see references[6,19,21-23,26,28,30-33].

1.1.4 Collagen tissue

Collagen is present in organs in order to provide a biomechanical stability, and it also influences the biochemical activity as the ECM regulates the cellular behaviour and cellular differentiation[21]. The role differs among connective tissues from being a supporting structure (type I) to a regulator (type III, type V)[34]. In general, collagen actually forms 1/3 of the total extracellular protein number, and its fibril-forming types I, II, III, V and XI (XXIV, XXVII[19]) are the most abundant types[32]. Type I collagen mostly occurs in bone, ligaments, tendon, skin, cornea, dentin, lung, and vasculature[9,28,35]. The associated fibrillar types, for example, type III and V usually coexist[28] with type I, and the type ratios are often analysed as markers of optimum composition[36,37]. The final fibril formation is strongly influenced by the types of tissue. For instance, in tendon, type I collagen fibrils are aligned parallel to each other but in skin the pattern follows more isotropic orientation. The fibrillar orientation, diameter, and mass in tissue is not stationary and remodel during ontogeny[38]. The remodelling is strongly related to the matrix metalloproteinase (MMP) family that can unwind and cleave the triple-helical structure in normal and abnormal tissue turnover[39]. Therefore, the properties of tissue change with disease, physical activity, or age.

1.1.5 Collagen tissue aging

The physiological changes in collagen tissue with age are frequently associated with the collagen types ratio, cross-link formation, and cross-linkers ratio at the molecular level[17,40]. In tendon, the mostly investigated cross-links are the mature non-reducible products of

enzymatic cross-linking; hydroxylysyl pyridinoline (HP), lysyl pyridinoline (LP)[18] that seem to be more tissue than species specific[29] and products of non-enzymatic cross-linking; advanced glycation end products' (AGEs)[41] markers, for example, fluorescent pentosidine[42], fructosamine[25], and glucosepane[43] (Fig 1.2). To a certain extent, cross-links stabilize the network and improve many of mechanical properties. However, extensive cross-linking with increasing age (particularly non-enzymatic cross-linking) often causes several drawbacks to the tissue. The fiber-tissue becomes stiffer[25] and more brittle[44]. The fiber structural ordering is modified[45], the speed of extracellular matrix remodeling and collagen turnover is reduced[6,46], and the healing ability and injury resistance is also decreased[17]. For all that, there is no general agreement. For example, Veres et al. reported that additional cross-linking do not significantly alter the mechanical properties of tendon[47]. It was also published that the AGEs cross-links forming rate is the highest in slow metabolism[29].

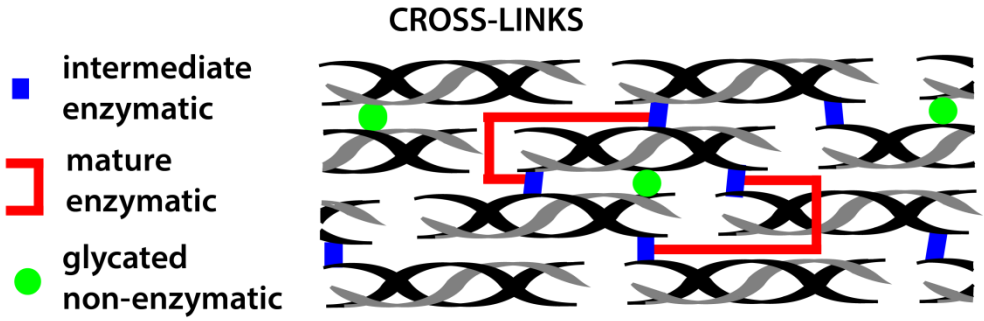

Fig. 1.2 Collagen interfibrillar cross-linking. The immature intermediate cross-links are normally located at the head-to-tail position, and the mature transverse interfibrillar cross-links provide the mechanical strength. The position of non-enzymatic cross-links is still a subject of discussion mainly because of the difficulties in detecting individual AGEs representatives. However, the results indicate that these cross-links are involved in the interfibrillar cross-linking[29].

Lastly, the above mentioned symptoms of aging are linked with other stimuli such as physical activity or diet, and therefore these stimuli can be used for cross-linking regulation. For instance, Kjaer stated that endurance training decreases the level of cross-linking and tissue stiffness[25]. This can be due to immediately elevated levels of both type I collagen synthesis and MMP after physical activity[29]. The diet problem was targeted by Goldberg who stressed the presence of AGEs in foods for different preparation methods – temperature[48].

It is obvious that the aging mechanism is very complex and still not fully understood. The current studies are reporting difficulties to uniformly describe some investigated phenomena. The mostly pronounced are the impact of cross-link formation and cross-linker ratios which are more unpredictable with age, and also correlations on stiffness and cross-linking are sometimes inconsistent between different tissue types and diseases[18,20,46,49,50], therefore the aging mechanism needs to be further investigated. For further reading about aging and collagen cross-linking see references[29,40-43,46,51,52].

1.2 Tendon

Tendon is a crucial component in the musculoskeletal system. Together with the intramuscular ECM, it transfers tensile forces from the skeletal muscle cells to bone. Its junction with muscle is placed at fascia and with bone, directly or indirectly, at the attachment site called enthesis. Surprisingly, the features of tendon have been studied less than the muscle and bone ones[25,53], although tendon injuries cover over 16.4 million cases in the United States[54]. This fact indicates that more investigation on tendon is required in order to understand the whole musculoskeletal system, its development, and injury prevention.

1.2.1 Hierarchical structure and composition

Tendon is a multi-hierarchical structure that is primarily built of type I collagen molecules, fibrils, fibre bundles, and fascicles (Fig 1.3)[55]. The 1 nm molecules[44] are constructed into the typical right-handed triple helix[28]. This rope-like rod structure of type I procollagen is 300 nm long and 1 – 2 nm in diameter, although the dimensions vary among tendons and species[56]. These procollagen rods are cleaved, cross-linked and then aggregated into microfibrils, fibrils, and fibres[57]. The fibres reach a diameter of up to 500 nm and length in the centimetre range in fascicles and tendons[6,27], and they occupy 60 – 80 % of the dry mass[14,57,58]. The fibers often appear with a typical structural crimp pattern[59-61], the origin, development, and function of which is still a subject of discussion[60,62]. The fibers and fascicles are bound together by endo- and epitenon, respectively, that contain blood vessels, lymphatics, and nerves[55]. This connective tissue allows sliding in an almost frictionless manner[57]. Although type I collagen comprises 95 % of collagen tissue, other types are usually present in tendon. Type III

dominates (2 ~ 3 %) among the minority, and it is usually found in healing or aging tendons in disorganized order[55,63]. There are also other collagen types V, VI, XII, XIV, and XV[57], which, for instance, contribute to control of fiber diameter (type V) or lubrication (type XII)[54]. Not only the presence of different types but also their ratios affect tissue properties[16]. Besides the collagenous proteins, the tendon ECM includes other components.

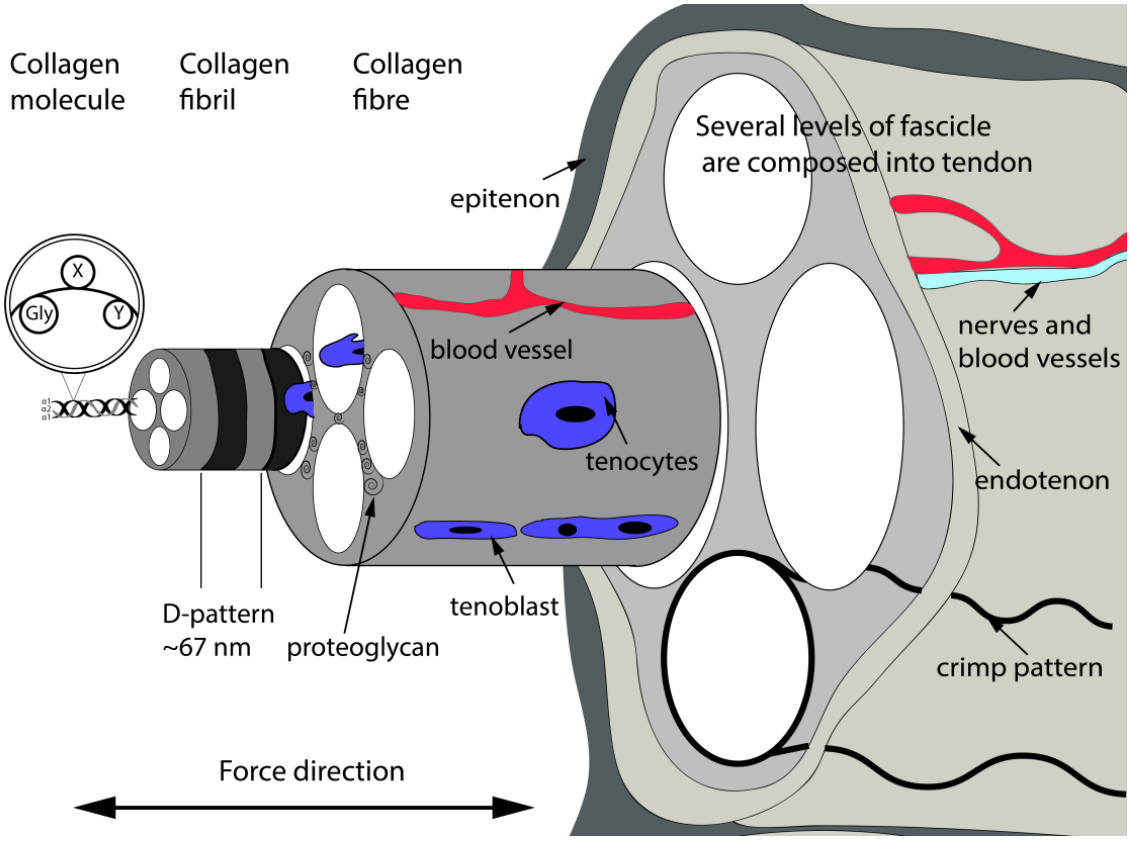

Fig. 1.3 Tendon structural architecture. Tendon is soft tissue which properties differ at each hierarchical level. Its structure consists of predominantly parallel fibres which lie within the tendon's long axis (force direction). This guarantees an efficient transfer of tensile mechanical load. The elastic fibres and a less stiff ground substance are not visualized but are attributed for viscoelastic behaviour. Tendon is not as rigid in activity as seems to be, however, the remodelling, for example, after the injury happens within months[57].

The elastic component is represented by elastic fibre which are also believed to be responsible for crimp pattern restoration after stretching[57]. The hydrophilic component that ensures viscous nature of tendon is called a ground substance. The ground substance is composed of hyaluronan, glycoproteins (e.g., aggrecan and decorin), proteoglycans

(compression-bearing region ~ 3.5 %, tension bearing region 0.2 – 0.5 %[55]), and other molecules including water (60 – 80 %)[57]. The last component is cell – tenoblast, tenocytes, synovial cells, chondrocytes, and vascular cells. Tenoblasts are fibroblast-like cells with elongated nuclei and thin cytoplasm that align in row between the fibres. Tenocytes are round cells that transform into tenoblast with age. The ratio of these cells affects the activity and response of tendon[64].

1.2.2 Mechanical properties and tests

From the mechanical point of view, tendon is a non-linear, inhomogeneous, and anisotropic material[1] that is exposed to a wide range of mechanical stimuli. These stimuli depend on physical activity and the location of tendon[54]. According to the location, tendons are sometimes divided into two biomechanical groups; high stress (energy storing) tendons and low stress (positioning) tendons. The location together with physical activity determines tendon morphology and mechanical properties[65]. This fact makes tendons mechanosensitive and mechanoresponsive[54] which results in continuous remodelling of tendon at various hierarchical levels. Predictably, a certain stimulus is favourable, however, overload can lead to tendinopathy[66]. In addition to mechanical stimuli and location, other factors such as age, disease, injury, or diet alter the material properties and functionality[40]. To reveal the complex material properties of collagen tissue, two approaches are usually adopted; experiment or simulation.

These approaches are both used to examine the tissue at different levels (molecule, fibril, fibre, fascicle, and tendon), by different testing protocols (e.g. quasistatic, dynamic, cyclic, or discontinued) and various environmental conditions (temperature, humidity). They also often target different tendon features (e.g. specific collagen types, proteoglycans, glycosaminoglycan (GAGs), or cross-linkers) and mechanical measures (elasticity, viscosity). The experimental testing of tendon is mostly acquired *ex vivo* using tensile uniaxial tests, which are sometimes accompanied by a visualisation method or for the molecular level by using atomic force microscopy, nanoindentation, and optical trap/Laser tweezers[67]. The *in vivo* testing is usually conducted using ultrasound techniques and electromyography. The obtained results are then displayed in the stress-strain curve and represented by a mathematical model.

The tendon stress-strain curve typically has "toe", "heel", linear, and failure regions (Fig. 1.4)[68]. From these regions, the resulting tendon characteristics are consequently quantified by intensive properties, for instance, yields strength, energy storage, energy dissipation, or Young's modulus[69].

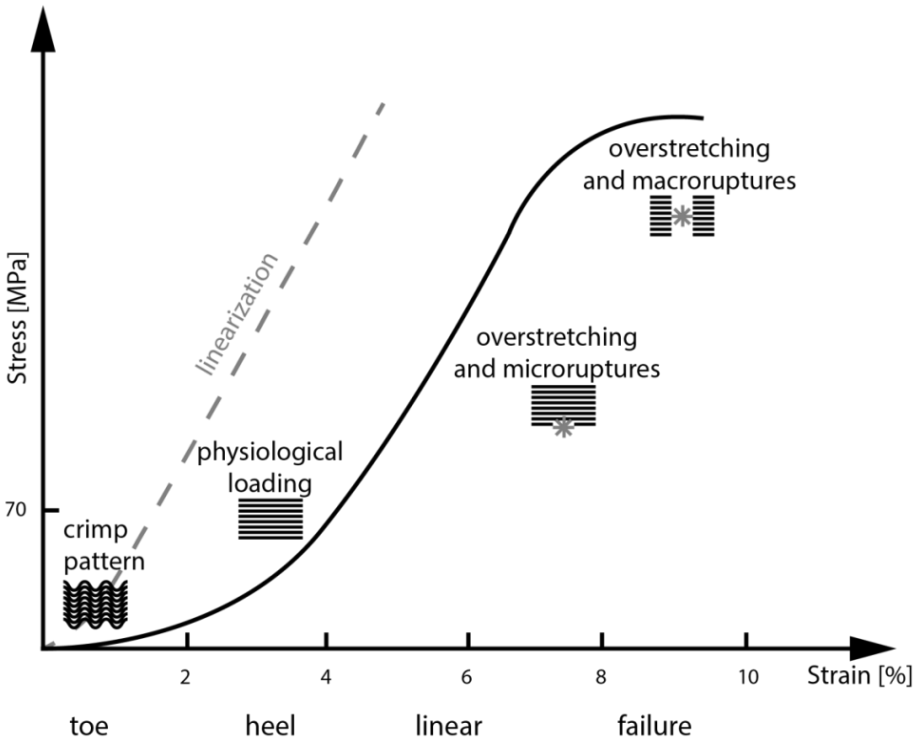

Fig. 1.4 Tendon stress-strain curve. The toe region contains strains below 2 % and the curve profile is probably influenced by the macroscopic crimp pattern parameters (wavelength, amplitude)[54,68]. The physiological limits reach up to 4% strain. In this region, a structural reorganization occurs within the inferior hierarchical orders, e.g. molecular kinks. Higher strains lead to additional stretching of collagen triple helixes and/or cross-links[68]. The macroscopic fractures appear at 10% strain. Some studies suggests that the physiological limit is even lower and remains in the toe region[70], and the ruptures occur at larger strains about 14 %[71]. The linearization of the curve and an increase of mechanical strength have been reported, for instance, with an increasing age, due to cross-linking[29], or decreasing water content in tendon[10].

Young's modulus is sometimes difficult to estimate because it is calculated as a tangent value to the linear region in the highly non-linear stress-strain curve, and therefore, multiple moduli are often stated along the stress-strain curve[40,44]. Tendon also shows time-dependant strain[72,73]. This characterises the tissue as viscoelastic. It means that with an increasing strain

rate the tissue response is closer to the dashed linearization curve in Figure 1.4. In addition, the viscoelastic properties are also affected by the testing temperature[74].

Another pitfall is a correct identification of the geometrical dimensions (Fig. 1.5) such as the tendon cross-sectional area (CSA) and the sample length. For instance, the CSA often varies greatly (more than 50 %) along the length of the Achilles tendon. Although there are very accurate techniques to map the tendon topography before conducting the tensile test (micro-computed tomography[75]), only one CSA value is usually used for the stress-strain calculation[53]. This fact questions the accuracy of the stress-strain curve and complicates the actual evaluation of the force transfer through tendon[76].

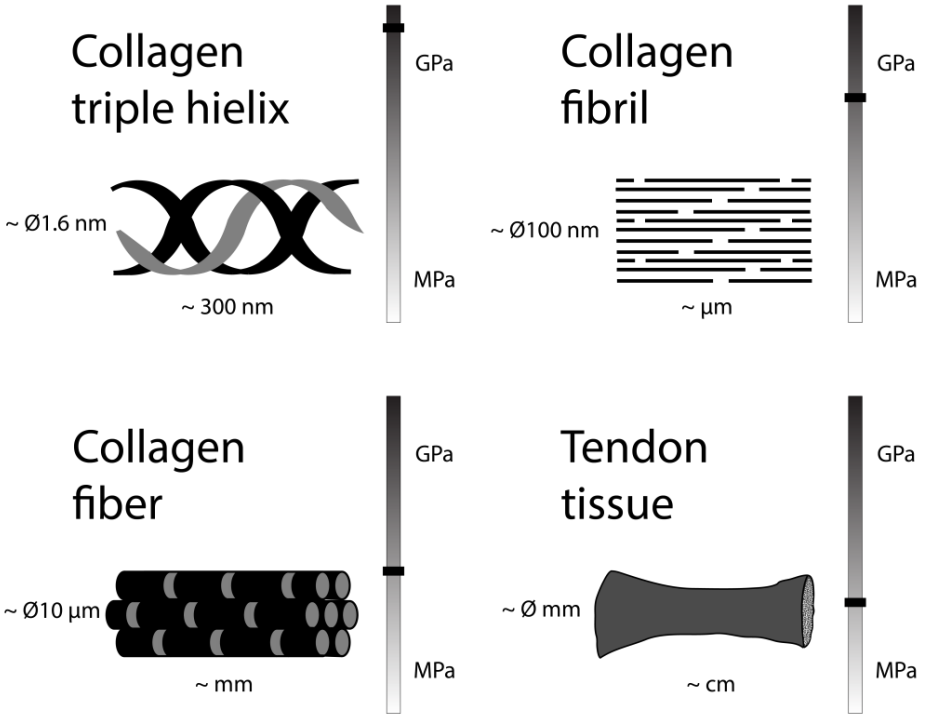

Fig. 1.5 Tendon hierarchical dimensions and mechanical properties. The geometrical dimensions of type I collagen fibrils vary among physical activity[77], anatomical locations, species, and age[56]. In addition, the length and continuity of individual fibrils, fibers also engender a lot of controversy[78]. It has been suggested that the smaller fibrils resist creep and the larger withstand high tensile forces[79]. In general, an individual tropocollagen molecule has the highest Young's modulus (~4.8 ± 2.0 GPa[10] (SD)) of all the hierarchical levels[6,72]. The value decreases for fibrillar collagen; however, there is a significant variation that depends on the used method, applied strain (small from 0.2 GPa vs. large to 38 GPa), cross-linking level[44], or environmental states (ambient vs. wet vs. dry)[10]. Young's modulus for tendon varies between 200 MPa and 1 GPa and it is highly dependent on the tendon's region[70,80]. The maximum tendon strain also varies among studies[70] as indicated in Figure 1.4.

The force is mostly introduced in the tendon's long axis during the tensile test, and it does not mimic the direction of the force transfer *in vivo*. This simplification can cause a significant error, especially for an investigation that includes tendons from more-headed muscles. For example, *musculus triceps surae* acts at the insertion tendon non-uniformly. This theoretically results in internal shear stress and probable tendon layers sliding[53] and/or helix uncoiling[40]. If the sliding is facilitated by the proteoglycans coat on the fibril and fibre surfaces[81], which is in disagreement with Svensson's findings[82], then proteoglycans contribution to the material response is partly neglected in such uniaxial tensile tests. In a recent study, Legerlotz et al. stated that the GAGs depletion may after all influence the mechanical properties by decreasing the failure stress. This phenomenon might be hypothetically related to the sample hydration or intermolecular bridges[66]. This example shows that the interactions among tendon building components and their mechanical behaviour *in vivo* are still poorly understood, which consequently conceals the origin of the tendon material response. Therefore, there is still missing a universally accepted model of tendon mechanical behaviour[83]. Although a universal soft tissue mechanics law does not exist, literature is full of approaches that try to interpret the mechanical behaviour of soft tissue, for example, tendon. The approaches often differ according to their final application.

The approaches can mostly be classified into two major categories, analytical or numerical, e.g. Finite Element Method (FEM)[84]. These approaches usually balance between accuracy and computational time and their applicability has obvious limitations[85]. *In vivo* FEM application, for instance, is challenging because of the definition of boundary conditions, large deformations and real-time computation cost. On the other hand, the analytical models (linear elastic, non-linear elastic or viscoelastic) are often complex with several parameters that have to be established and which can significantly influence the accuracy of the model. However, it seems that some of the analytical models (Elastic, Kelvin-Voigt, Kelvin-Boltzmann, Maxwell, Hunt–Crossley or Fractional) can be feasible for tool-tissue position/force control in robotic surgery[84], and the numerical methods are currently suitable for simulations and design validation in tissue engineering or custom replacement surgery[86].

As the section above has demonstrated, to identify and validate mechanical properties of tendon is highly challenging. First, the research usually targets one particular aspects of this multi-composite biomaterial. Second, the tendon properties differ among species, location, region, and age. When some other variations are added, for example, modifications in loading protocol, testing environmental condition, sample processing, and mathematical apparatus, the comparison among different studies becomes highly difficult. This complicates the usage of the data in the field of surgery, tissue engineering or regenerative medicine. Finally, for further reading about soft tissue and tendon mechanical properties see references[14,55,68,83,87-90].

1.2.3 Visualisation methods

To obtain the knowledge and results mentioned in Section 1.1.3 and 1.2.1, there exist several groups of detection methods and techniques. One of the groups uses radiation. The type of radiation defines a theoretical achievable resolution and consequently the hierarchical level of connective tissue which is possible to observe. Unfortunately, the individual hierarchical levels are not usually available separately, and therefore the tissue state and sample preparation steps influence the visualisation. For instance, tendon is usually imaged *ex vivo* by preparing microtome sections and performing immunostaining.

Initial tendon visualisation is usually acquired by a simple optical CCD/CMOS camera. This macroscopic investigation is used to reveal basic information on surface and geometry. By adding another camera, the setting can be transformed into a 3D stereo-camera analyzer that detects spatial deformation[91]. For *in vivo* application, this method requires large tissue opening, and therefore ultrasound imaging[92,93], magnetic resonance imaging (MRI)[94], or computed tomography (CT)[95] are more convenient. However, the spatial resolution and specificity of these methods are often insufficient, and then surgical opening is still necessary. To reduce the surgical intervention, an optical device can be design into an endoscope[96] or a capsule[97]. In essence, these *in vivo* probes are miniature microscopes that use optical principles to acquire images. The principles can be divided into the groups of linear or non-linear optics[96].

The linear optics includes phenomena when the induced dielectric polarization vector field of the isotropic material $\vec{\boldsymbol{P}}(\omega)$ response linearly to the strength of the optical vector field $\vec{\boldsymbol{E}}(\omega)$. This relationship can be simply written as

$$\vec{\boldsymbol{P}}(\omega) = \varepsilon_0 \boldsymbol{\chi}^{(1)} \vec{\boldsymbol{E}}(\omega), \tag{1.1}$$

where ε_0 represents the vacuum permittivity and $\boldsymbol{\chi}^{(1)} = \boldsymbol{\varepsilon_r} - 1$ the frequency (ω) dependant first-order electric susceptibility of the material[98]. Based on this behaviour, linear absorption, transmission, reflection, or fluorescence/phosphorescence are utilized for the contrast enhancement optical techniques, for instance, phase contrast, brightfield, differential interference contrast, total internal reflection, polarized light microscopy, confocal microscopy, or widefield fluorescence/autofluorescence microscopy. For more details on optical microscopy and the techniques see the reference[99]. In general, when using optical microscopy, mature tendons are visualised by polarized light microscopy to examine tendon fascicles and their crimp pattern[65,100]. Sometimes, other optical techniques such as phase contrast microscopy and interference microscopy can be combined to reveal the origin of the crimp pattern[101]. For *in vitro* experiments, a combination of methods is often adopted, for instance, differential interference contrast with widefield fluorescent imaging[102]. To advance the common excitation methods which rely on one-photon absorption or scattering, non-linear optical methods are currently becoming the choice for studying biological materials[103].

For the non-linear optical methods, the linear relationship between dielectric polarization of anisotropic materials $\vec{\boldsymbol{P}}_i(\omega)$ and the strength of the optical field $\vec{\boldsymbol{E}}(\omega)$ does not hold anymore and dielectric polarization can be written as a power series

$$\vec{\boldsymbol{P}}_i(\omega) = \vec{\boldsymbol{P}}_i^{(1)}(\omega) + \vec{\boldsymbol{P}}_i^{(2)}(\omega) + \vec{\boldsymbol{P}}_i^{(3)}(\omega) + \cdots =$$
$$\varepsilon_0[\boldsymbol{\chi}_{ij}^{(1)} \vec{\boldsymbol{E}}_j(\omega) + \boldsymbol{\chi}_{ijk}^{(2)} \vec{\boldsymbol{E}}_j(\omega)\vec{\boldsymbol{E}}_k(\omega) + \boldsymbol{\chi}_{ijkl}^{(3)} \vec{\boldsymbol{E}}_j(\omega)\vec{\boldsymbol{E}}_k(t)\vec{\boldsymbol{E}}_l(\omega) + \cdots], \tag{1.2}$$

where $\boldsymbol{P}_i$ is the component of the i^{th} polarization and $\boldsymbol{\chi}^{(2)}$ and $\boldsymbol{\chi}^{(3)}$ represent the second- and third-order susceptibility. The higher orders represent the non-linear response of the material.

For example, the second-order susceptibility $\boldsymbol{\chi}^{(2)}$ is a third-order tensor witch matrix consists of 27 Cartesian components in the coordinate system x, y, and z (Eq. 1.3)[98].

$$\boldsymbol{\chi}^{(2)} = \boldsymbol{\chi}_{ijk}^{(2)} = \begin{bmatrix} \chi_{xxx}^{(2)} & \chi_{xxy}^{(2)} & \chi_{xxz}^{(2)} \\ \chi_{xyx}^{(2)} & \chi_{xyy}^{(2)} & \chi_{xyz}^{(2)} \\ \vdots & \vdots & \vdots \\ \chi_{zzx}^{(2)} & \chi_{zzy}^{(2)} & \chi_{zzz}^{(2)} \end{bmatrix} \tag{1.3}$$

According to the symmetrical rules, the tensor $\boldsymbol{\chi}^{(2)}$ is zero for crystals with inversion symmetry, and therefore, the sum frequency generation (second harmonic generation (SHG)) are forbidden in such media[104]. On the other hand, several biological structures, for instance, type I and II collagen[105-109], myosin[110] or microtubules[111], lack the symmetric structural centre. For this reason, these non-centrosymmetric structures (harmonophores) are favourable for label-free SHG microscopy[112]. Unlike the linear optical methods, SHG microscopy does not require exogenous labelling, does not suffer from photobleaching, decreases photodamage, guarantees confocality and allows deep tissue optical sectioning[103,113]. In addition, the method is often combined with other methods such as two-photon excited fluorescence (TPEF)[113,114], two-photon excited autofluorescence[115-117], fluorescence lifetime imaging microscopy (FLIM)[118], coherent anti-Stokes Raman scattering (CARS)[119,120], or polarized SHG microscopy (PSHG)[107,110,121-124]. Although these methods are still limited by diffraction, i.e. ~250 nm laterally and > 450–700 nm axially[125], they can retrieve sub-diffraction information about the studied structures, for instance, the helical pitch angle of collagen molecule[110,123,124], discrimination of type I and type II collagen[106], or metabolism activity[126,127]. For more details on non-linear optics and non-linear microscopy see the references[22,98,104,128-130].

To visualize smaller features of tendon such as individual fibrils or even collagen at the molecular level, the methods of atomic force microscopy[131], X-ray diffraction[33,132,133], or electron microscopy (TEM/SEM)[62,83,134] are the most common choices[67]. Unfortunately, these methods require complex multi-step sample processing, e.g. freezing, cutting, staining, and fixing that can cause a significant bias to results[135].

Chapter 2

2 Production of type I collagen *in vitro* and detection techniques

2.1 Introduction

Collagen is considered to be one of the key markers for tissue development, organisation, and dysfunction[136]. Therefore its precise tracing through newly synthesized tissue helps with the quantification and subsequent optimization of *in vitro* constructs. A convenient cell type for such a methodological investigation seems to be cardiac valve interstitial cells (VIC) as they share morphological and functional characteristics of fibroblasts, smooth muscle cells, and myofibroblasts[137]. This predetermines these cells for strong production and remodelling of extracellular matrix (ECM) proteins, especially synthesis and secretion of the type I collagen protein.

The quality of the collagen protein and its assembly into fibrils and fibres are controlled by numerous cofactors. These cofactors act intracellularly[24] and extracellularly[19], for instance, the intracellular hydroxylation of proline that is crucial for stabilizing the collagen triple helix[138] would not be possible without ascorbic acid (AA)[139]. Considering the hydroxyproline production, it reduces distinctly when the concentration of AA is less than 6 µg/ml in tissue, although the normal concentration was established to be approx. 60 µg/ml[140] or 50 µM in plasma[141], and the saturation level is about 70 µM in plasma[142]. The reduction below the minimum level results in defected hydroxyproline, and therefore collagen instability[143].

This instability is projected in the lower amount of extracellular type I collagen when examined by immunostaining[144]. However, no immunostaining provides qualitative information on the type I collagen assembly. In sharp contrast to immunostaining, non-linear label-free methods, for example, second harmonic generation (SHG) microscopy, provide powerful complementary information[145] for an accurate diagnosis on pathological conditions[146]. Unfortunately, no complete agreement has been reached on the peptide groups which contribute to the SHG signal, the second-order susceptibility tensor of collagen molecule, respectively[122,147]. Nevertheless, it was proposed that hydroxyproline strongly contributes to the second-order susceptibility tensor of collagen molecule[107], and therefore its instability should impair the generation of the second harmonic signal.

Production of type I collagen in vitro and detection techniques

In this chapter, the *in vitro* model is constructed and validated with the conventional methods that target the expression levels of type I collagen gene or visualise type I collagen intracellularly and/or extracellularly, or by non-linear label-free methods such as SHG microscopy. After that, the validated *in vitro* model is produced without AA, and the same evaluation methods are performed on the culture. This approach will provide more information on the model as well as confirm whether the generation of the second harmonic signal is impaired by the AA insufficiency and hydroxyproline defect, respectively.

2.2 Material and Methods

2.2.1 Isolation of VICs

First, the laboratory pig was spent by injecting thiopental and potassium chloride. Second, the preparation of the surgical field was performed. Mediastinum was accessed via median sternotomy. Pericardium was rigorously dissected in order to gain as much pericardial tissue as possible for further investigation. Pericardium was then excised en bloc. The heart was exposed and explanted. The dissection continued into the region of the aortic root. Transverse aortotomy was performed and an excision of the valve was carried out. The valvular tissue was stored in a preservation solution. Third, the valves were cut into small pieces and incubated in Dulbecco's Modified Eagle Medium (DMEM, D5648, Sigma, USA) containing 40 μg/ml of gentamicin, collagenase, type 3 (149 U/ml, LS004208, Worthington Biochemical Corp., USA), collagenase, type 2 (492 U/ml, LS004204, Worthington Biochemical Corp., USA), neutral protease (0.56 U/ml, LS02104, Worthington Biochemical Corp., USA), deoxyribonuclease I (0.1 mg/ml, LS002060, Worthington Biochemical Corp., USA), hyaluronidase (0.2 mg/ml, 499 USP/NF U/mg, LS005474, Worthington Biochemical Corp., USA), and antibiotic-antimycotic solution 2.5% (Sigma, USA) for 4 hours. Finally, the cell suspension was centrifuged at 1,000 rpm for 5 min, the cells were resuspended in DMEM medium with 10% fetal bovine serum, centrifuged again and cultured in DMEM with 10% FS at 37°C in humidified atmosphere with 5% CO_2. This isolation of VICs was performed from three different pigs during the period of the proceeding experiments.

2.2.2 Cultivation of VICs

The cells in passage 3 – 5 were seeded at a density of 5,000 per cm^2 on sterile coverslips, placed in 24-well plates (TPP) and incubated in the growth medium at 37°C in humidified atmosphere with 5% CO_2 for 3 days. Production of collagen was induced by adding AA (Sigma, USA) to the cell culture medium for 7 days in a daily concentration of 50 µg/ml; control cells were kept in the growth medium only. A different coverslip was used for each method, but the cells were cultivated together and treated the same way. Each cell passage was considered as an independent experiment.

2.2.3 Staining of VICs

For the staining of collagen in the permeabilized cells, the cell culture was rinsed with PBS, fixed with 70% cold ethanol and blocked with 1% bovine serum albumin in PBS for 20 min. The ethanol fixing of the cell culture caused permeabilisation of the cells which provide immunostaining of both extracellular and intracellular collagen. The primary antibody (Anti-Type I Collagen, rabbit, dilution 1:200 in PBS, Cosmo Bio, Japan) was applied overnight at 4°C.

For the staining of collagen in the non-permeabilized cells, the 24-well plate with living cells in their cell culture medium was placed on ice for 10 min, then washed twice with ice-cold wash solution (PBS with 5% FBS). The primary antibody (Anti-Type I Collagen, rabbit, dilution 1:200 in ice-cold wash solution, Cosmo Bio, Japan) was applied for 30 min on ice. The cell culture was washed twice with ice-cold wash solution and then fixed with 2% paraformaldehyde in PBS. After the fixation, the cell culture was removed from ice, washed twice with PBS and blocked with 1% FBS in PBS for 20 min at ambient temperature. After that, the cell culture was again washed with PBS.

After the washing with PBS, both the permeabilized and non-permeabilized cell cultures were incubated with the secondary antibody (Goat anti-rabbit Alexa Fluor 488 conjugate, dilution 1:400 in PBS, Invitrogen, USA) for 1 hour at ambient temperature. The cells were then rinsed with PBS. To identify the location of cells, several samples were counterstained with Hoechst 33342 (0.5µg/ml, Life Technologies, USA) to mark the nuclei or with

CellTracker™ Green CMFDA (Molecular Probes, USA) to mark the cells' cytoplasm. These stains were used according to the manufacturer's protocol.

2.2.4 Microscopy of VICs culture

The fluorescence microscopy images were obtained using the inverted IX 51 epifluorescence microscope equipped with the LCPLFL 20x/0.4 objective (image resolution 1360x1024 pixels, pixel size 315 nm) and the DP 70 digital camera (all manufactured by Olympus, Japan).

The SHG and (two-photon excitation microscopy) TPEM images were acquired using the Leica TCS SP2 AOBS confocal laser scanning head mounted on the inverted Leica DMIRE2 microscope (Leica, Germany) and equipped with the mode-locked Ti:Sapphire Chameleon Ultra laser (Coherent Inc., USA), tunable from 690 to 1040 nm. The femtosecond pulse laser was tuned to 860 nm and the incident beam reached the samples through an objective (Leica HCX PL APO 63x NA 1.2, water immersion, image resolution 1024x1024 pixels, and pixel size 233 nm). Because of the SHG nature, a half wavelength response signal, i.e. 430 nm, was detected in backward, in non-descanned mode (green channel). The signal was collected directly behind the objective; passing an IR filter (703HSP, Laser Components GmbH, Germany) and a bandpass filter (HQ430/20 M-2P, Chroma, USA) before reaching a standard PMT4 detector (Leica, Germany). Two-photon excitation microscopy (TPEM) was used to image the immunofluorescence signal from the stained samples. The excitation wavelength remained the same as for the SHG imaging (860 nm) and the green fluorescence of the samples was detected by using the internal PMT2 detector (540 ± 50 nm; red channel; filter-free AOBS system) (Fig. 2.1). The samples were optically sectioned from the top to the bottom with a 1μm step. All the images were acquired on 7-day culture.

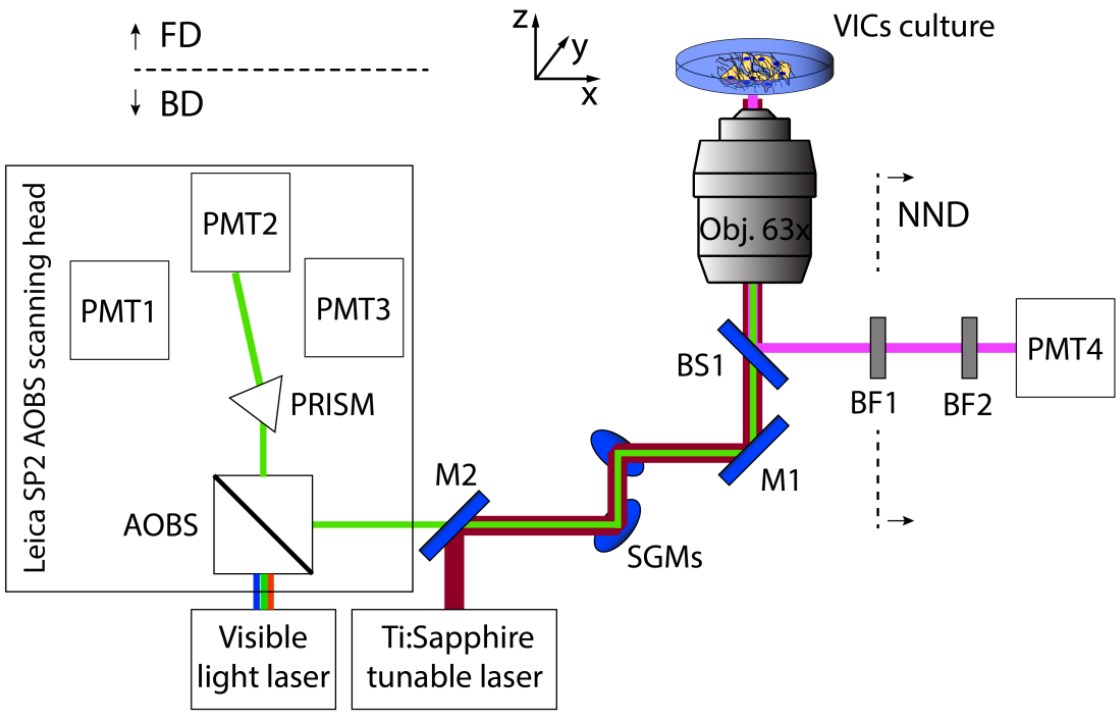

Fig. 2.1 Schematic of optical setup. **FD** and **BD** point to the forward and backward direction from the focal plane of the objective. **AOBS** is the Acousto-Optical Beam Splitter. **M1** and **M2** are the reflecting mirrors. **SGMs** are the scanning galvanometer mirrors. **BSl** is the beam splitter. **BF1** represents the IR filter and **BF2** the band-pass filter. **NND** points toward the non-descanned direction. **X** axis is identical with the horizontal direction.

2.2.5 Correlation analysis of VICs culture images

The co-localization was sought between the TPEM and SHG channels for both the permeabilized and non-permeabilized stained cell cultures. Before running the correlation analysis, each image was segmented for collagen features enhancement. First, the image was processed using a 2-D median filter 4 x 4 to remove noise, then the histogram equalization was applied, and the image was transformed into the binary mask. Then each original image was multiplied with its mask, and the resulting pairs of images were compared using a 2-D correlation analysis. For each pair of images, one correlation coefficient was obtained and assigned to the permeabilized or non-permeabilized group, respectively. Finally, the two groups ($n_1 = n_2 = 38$) of the correlation coefficients were compared for a statistical difference (Shapiro-Wilk test and independent samples t-test). The image processing, correlation analysis (*corr2* function), and statistical comparison was run in Matlab 2015a (Mathworks, USA).

2.2.6 Collagen quantification

The amount of collagen deposited in the extracellular matrix was determined together with intracellular collagen with the Sircol kit (Biocolor, UK). Before the determination, the collagen was recovered from the cell layer by acidic pepsin digestion. The cell layers were rinsed with PBS and were harvested with a cell scraper in PBS and centrifuged. The cell pellets were resuspended in a pepsin solution (0.1 mg/ml in 0.5 M acetic acid) and were lysed for 24 hours on ice. The lysates were centrifuged and supernatants were concentrated according to the Sircol kit manufacturer's protocol. The amount of collagen in the samples was then determined, together with the standard curve, by Sirius red dye binding according to the manufacturer's protocol. The results were normalized by the DNA content of the parallel samples. The experiment was performed in triplicate and repeated three times.

2.2.7 Real-time polymerase chain reaction (PCR)

Total RNA was extracted from the cell layers with RNAzol (Molecular Research Center, USA) according to the manufacturer's protocol. Reverse transcription was performed using oligo-dT primers with the ProtoScript M-MuLV First Strand cDNA Synthesis Kit (New England Biolabs, USA) according to the manufacturer's protocol. Real-time PCR reactions were performed using FastStart Universal SYBR Green Master Mix (Roche, Switzerland) on the iQ5 Multicolor Real-Time PCR Detection System (BioRad, USA). The Real-time PCR parameters were: 40 cycles, 95°C for 10 sec and 60°C for 1 min; the reactions were carried out in duplicate. The Real-time PCR data were analysed in BioRad iQ software and CFX Manager software using the $\Delta\Delta C_T$ method, including the efficiencies of particular primer pairs (Tab. 2.1) in order to increase the accuracy of the results.

Table 2.1 Real-time PCR primers that were used for the higher accuracy of the method.

Gene	Primer sequences (5'-3')	Product length [bp]	Efficiency [%]
Type I collagen[148]	CAGCCGCTTCACCTACAGC TTTTGTATTCAATCACTGTCTTGCC	83	92.5
GAPDH[149]	TGCACCACCAACTGCTTAGC GGCATGGACTGTGGTCATGAG	87	93.3

The expression level of type I collagen gene was normalized to the expression of the GAPDH gene which was the most reliable among other tested genes (18s RNA, RPL27, beta-actin) and related to the expression level of the cells harvested on day 0. The experiments were performed in duplicate and repeated three times.

2.2.8 DNA content quantification

The cell layers were rinsed with PBS and lysed in 0.05% SDS in Tris-EDTA (TE) solution at room temperature with shaking for 30 min. The lysates were diluted 10 times with TE, and the total DNA content in the lysates was determined together with the standard curve using the Quant-iT™ PicoGreen® dsDNA Kit (Invitrogen, USA) according to the manufacturer's protocol. The experiment was performed in triplicates and repeated three times.

2.3 Results

2.3.1 In vitro model of collagen synthesis

The fluorescent images of the fixed and immunostained VICs cultures revealed a coherent layer with type I collagen structures deposited in both cultures (Fig. 2.2).

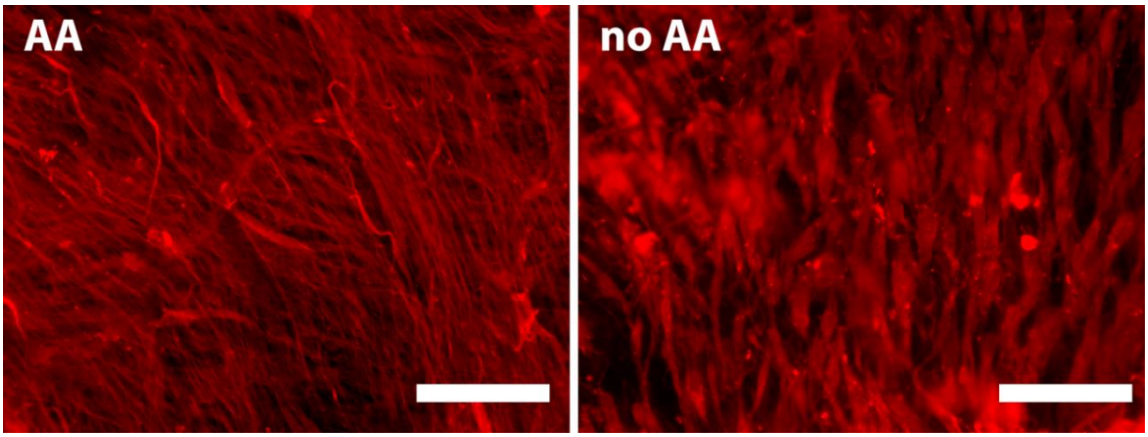

Fig. 2.2 Immunofluorescent images of collagen in cultures. Both (**AA**) and (**no AA**) images of the cell cultures were positive for type I collagen staining, although it seemed that the ECM collagen fibrils were more pronounced in the cell culture with AA treatment. Scale bar: 100 µm.

The results based on the DNA amount showed that the cell growth was significantly higher in the culture with AA treatment than in the culture without AA treatment (Fig. 2.3A). Also

the amount of collagen deposited in the cell layer was markedly higher compared to the cell culture without AA treatment after 7 days (Fig. 2.3B). On the contrary, the expression levels of type I collagen gene reached similar values for both the cultures during 7 days (Fig. 2.3C).

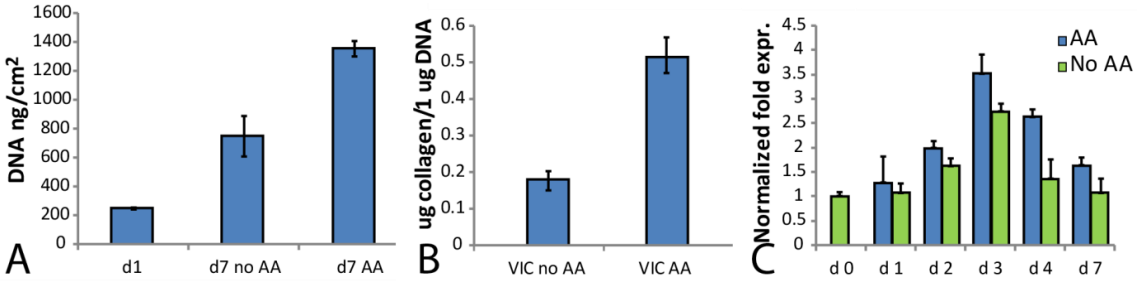

Fig. 2.3 Collagen expression quantification. (**A**) Characterisation of cell growth in conditions with and without AA treatment represented by the amount of DNA on day 1 and 7 (PicoGreen assay). (**B**) Quantification of the collagen protein in the cell layer on day 7 (Sircol assay). (**C**) Quantification of type I collagen mRNA - RT-PCR (culture with and without AA treatment). The box plots represent mean and the whiskers standard deviations.

2.3.2 Staining extracellular type I collagen

It was proved that the ethanol fixing of the cell culture caused permeabilisation of the cells and consequently collagen staining was detectable in both the extracellular and intracellular space (Fig. 2.5 top). On the other hand, only extracellular type I collagen fibres were revealed in the non-permeabilized cell culture (Fig. 2.5 bottom), however, the staining appeared weaker. In both staining approaches, i.e. permeabilized and non-permeabilized, the SHG signal was detected, but for the non-permeabilized cell culture group the SHG and TPEM images returned a significantly higher correlation coefficient (Fig. 2.4).

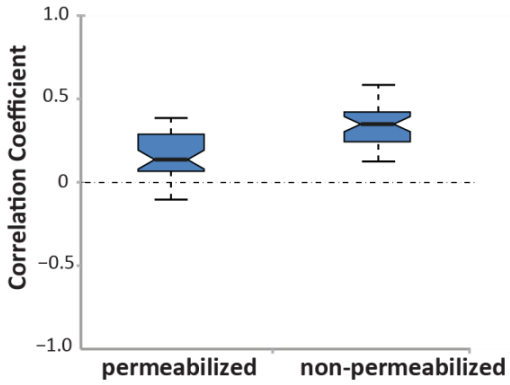

Fig. 2.4 Correlation coefficients between SHG and TPEM images. The p-value for comparing permeabilized and non-permeabilized groups was set ≤ 0.01. The box-and-whisker plot; the centre line highlights median, the notch boxes 25th and 75th percentile, and the black whiskers maximum/minimum.

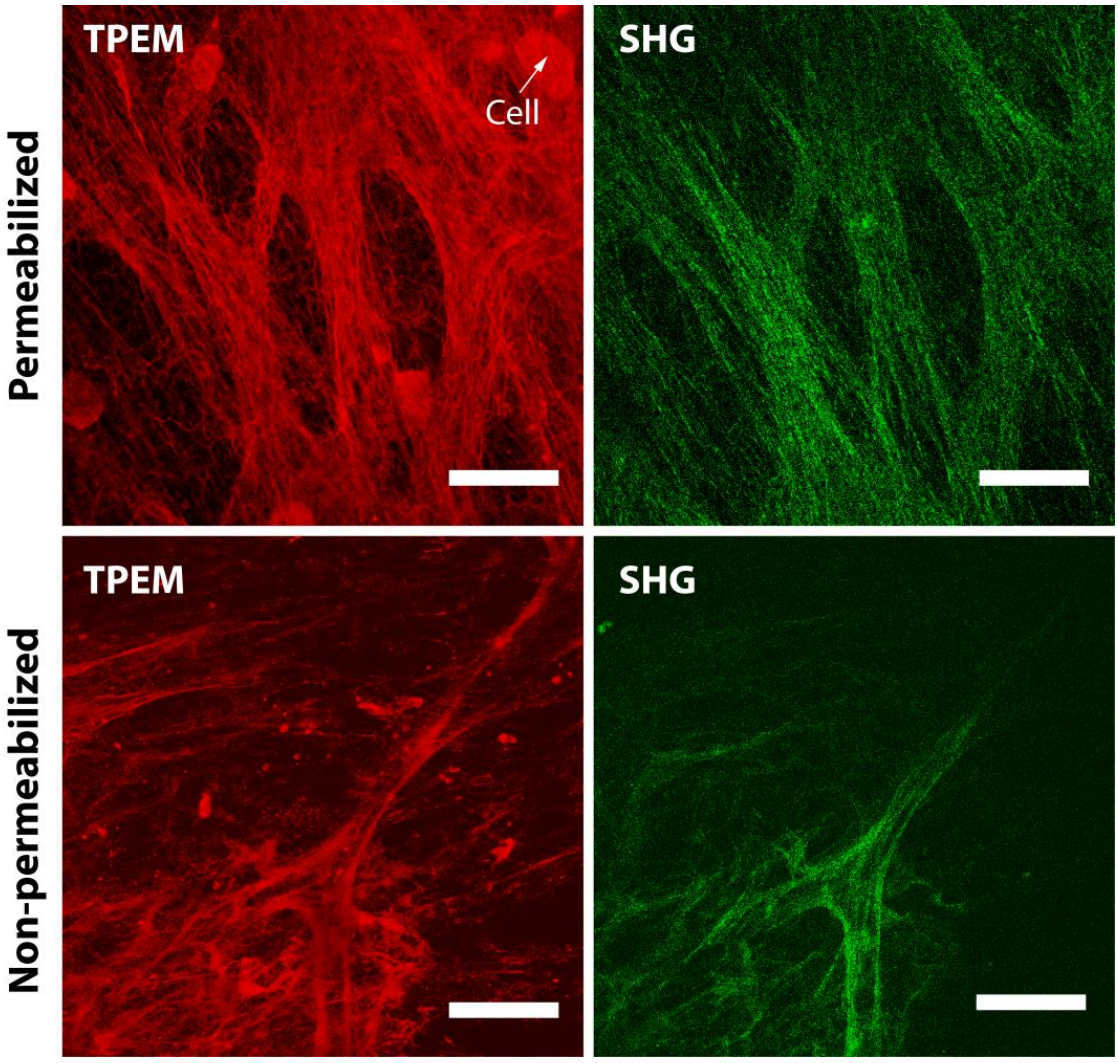

Fig. 2.5 SHG and TPEM (non-)permeabilized culture images. The images above represent the difference in staining the permeabilized and non-permeabilized cell cultures (TPEM – red). The same samples were also investigated by SHG microscopy (green). Scale bar 50 µm.

2.3.3 Collagen fibres deposition without AA treatment

The images with counterstained cell nuclei showed the position of the cells present in both the cell cultures. In addition, a distinctive ECM fibrillar network was visible in both the cell cultures, however, the fibres were less numerous and clustered in the cell culture without AA treatment (Fig. 2.6). When examining the cultures with SHG microscopy, the fibrillar structures were detected only in the cell culture with AA treatment (Fig. 2.7).

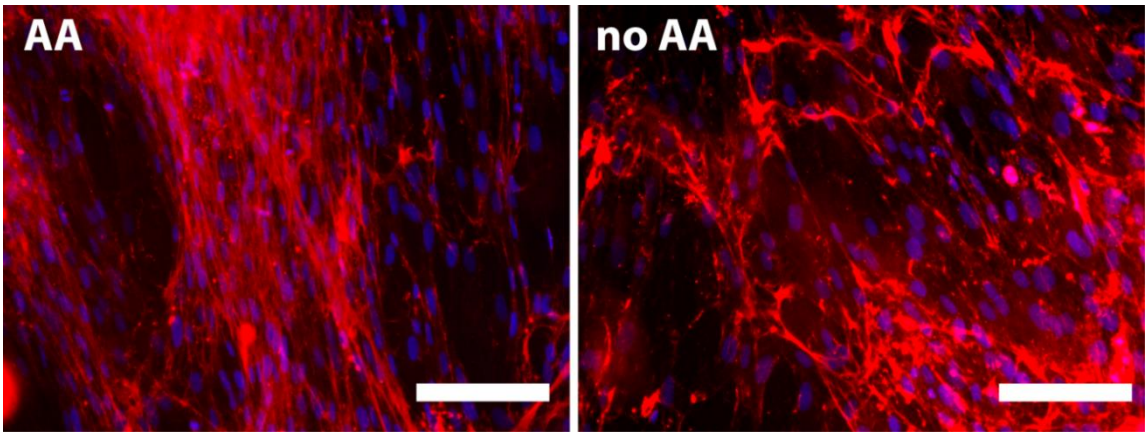

Fig. 2.6 Nuclei stain and non-permeabilized culture collagen antigen. The cell nuclei (blue) and the extracellular collagen (red) were counterstained in the cell cultures treated with AA (**AA**) and without AA (**no AA**). Scale bar: 100 µm.

The images of the cell cultures with no AA treatment contained no or low-to-detect SHG signal. The CellTracker^{TM} staining added the information about the shape of embedded cells (Fig. 2.7).

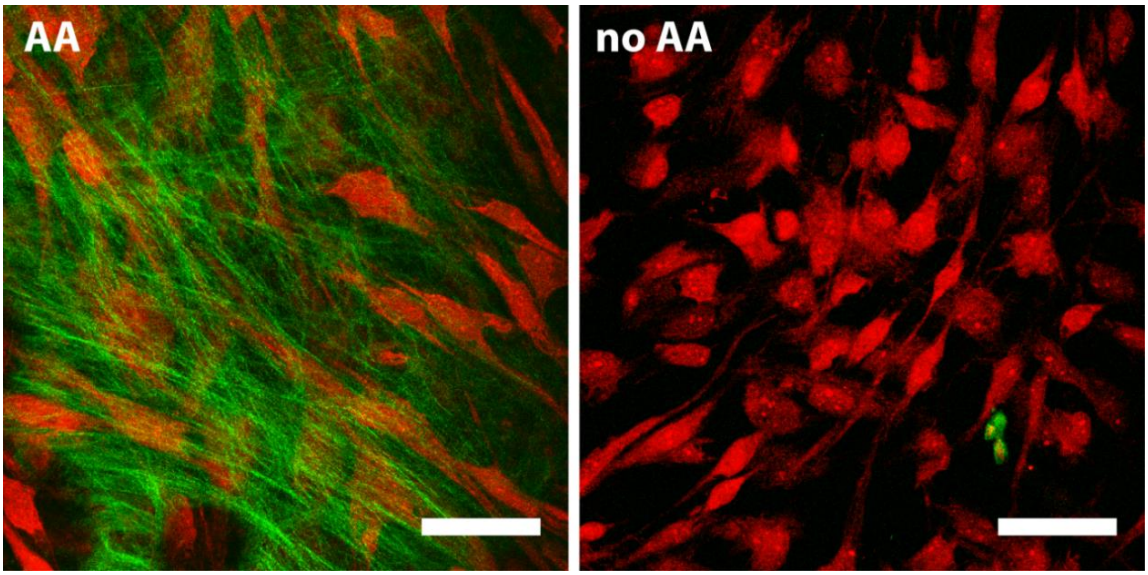

Fig. 2.7 SHG and TPEM cultures images (CellTracker^{TM}). **(AA)** The red color represents TPEM signal coming from cells cytoplasm (CellTracker^{TM}), and the green color represents the SHG signal generated by collagen molecules. **(no AA)** The image overlay of the TPEM and SHG channels for the cell culture with no AA treatment. Scale bar: 50 µm.

In the case of the non-permeabilized cell culture with AA treatment, the SHG signal was generated by the collagen fibres. In contrast, there was again no SHG signal detected for the cell culture without AA treatment (Fig. 2.8).

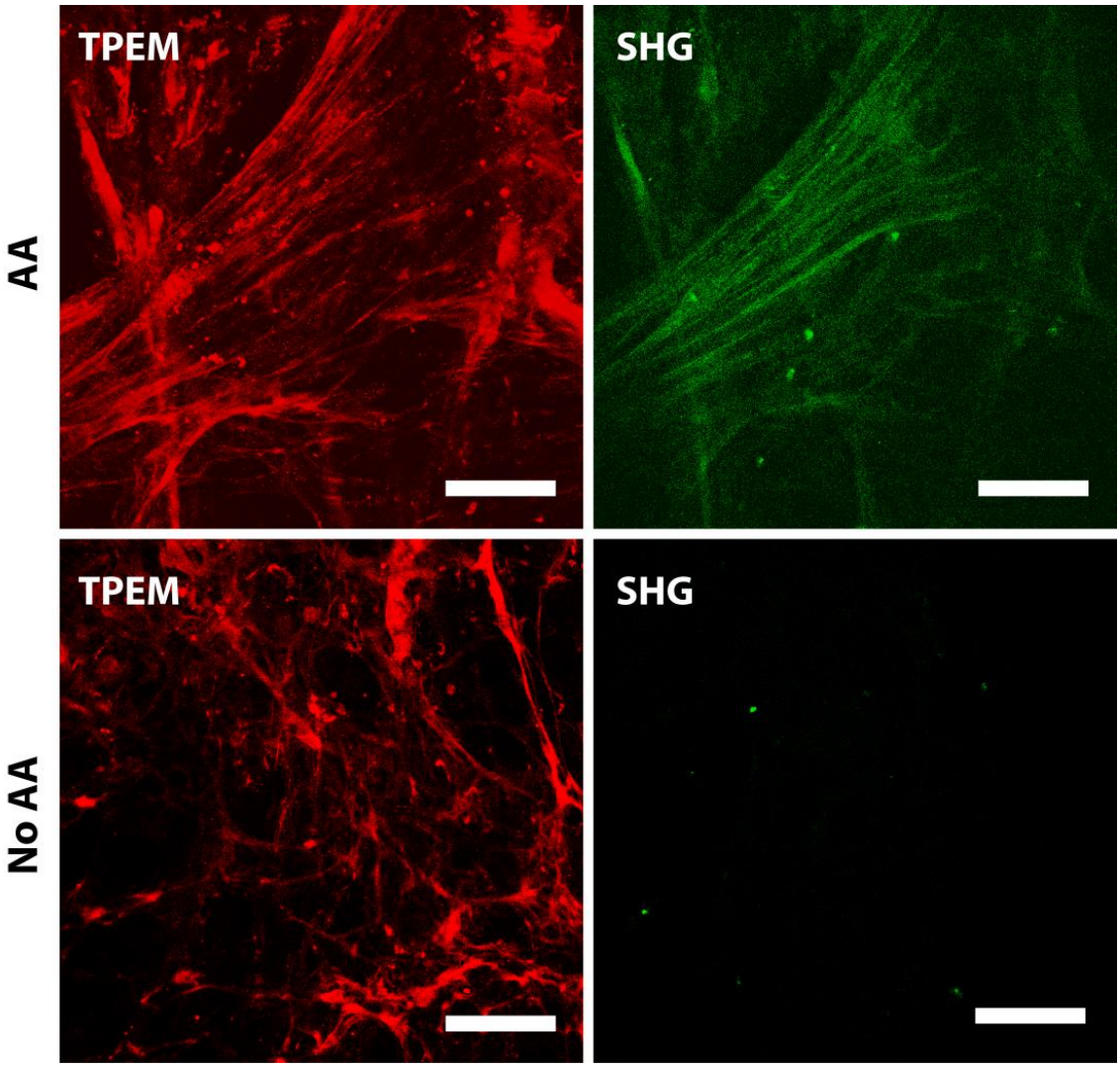

Fig. 2.8 TPEM and SHG images for AA/no AA cultures. Both non-permeabilized cell cultures treated with AA and without AA were immunostained for extracellular collagen fibres (red) and imaged by SHG microscopy (green). Scale bar: 50 µm.

2.4 Discussion and conclusion

In order to access the intracellular space, the cell layer was fixed by ice-cold ethanol. These permeabilized cell cultures appeared with labelled intracellular and extracellular collagen. In contrast, no intracellular collagen was labelled in the non-permeabilized cell cultures when the primary antibody was applied directly on living cells. In addition, according to Glynn and McAllister, the primary antibody should be applied to the cell cultures at ambient temperature[150]. Unfortunately, this method does not take into account the endocytosis and retrograde vesicle transport, which can deliver the antibody from the cell surface inside the cells[151]. Therefore the cell cultures were placed on ice in our protocol before and during applying the primary antibody. Another marking difference to Glynn and McAllister's protocol is the fixation after applying the primary antibody and washing. This fixation of the cell culture preserves the structures at the time point of staining and does not allow additional changes to morphology due to the following staining procedures. Overall, this protocol seems to be ideal for labelling the cell surface and extracellular antigens, even if they also occur intracellularly. This protocol can also be followed by cell permeabilisation and additional staining of intracellular antigens.

The extracellular type I collagen network appeared clearly in the cell culture with or without AA treatment when monitored with immunofluorescence staining. Kubow et al. published similar result highlighting a lower amount of collagen fibres in the ECM when 3T3 fibroblasts were cultivated without AA treatment[144]. The collagen network presence was even more pronounced when the staining was performed on the non-permeabilized cell culture. This result can lead to an assumption that the collagen fibres are expressed and assembled correctly in such cell cultures. This assumption was rejected when the cell cultures were examined by SHG microscopy; no SHG signal was detected in the cell culture without AA treatment. This result confirmed the models of second-order susceptibility tensor $\chi^{(2)}$ in which hydroxyproline plays the crucial role for generating the SHG signal. In general, some collagen can be produced and even deposited into ECM without AA treatment but the assembly into fibres is inefficient[152]. With AA treatment, the SHG signal was evidently detectable from fibres in the cell culture and due to a longer excitation wavelength (860 nm), it did not coincide with the ECM autofluorescence[114]. The positive influence of AA treatment

was also demonstrated on cell growth and deposited collagen. Higher fibre deposition was also reported by Contard et al.[153] as well as higher expression levels of collagen by Graham et al.[154]. Furthermore, both the permeabilized and non-permeabilized cell cultures with AA treatment generated some SHG signal but, as expected when compared with the TPEM images, the correlation coefficient was significantly higher for the non-permeabilized cell culture. This staining approach combined with SHG microscopy helps to clearly distinguish between intracellular and extracellular type I collagen and avoids issues with scoring and specificity of commercially available antibodies[155].

Overall, a successful procedure for isolating the VICs from the pig pericardium and their culturing was completely described in this chapter. Furthermore, the collagen staining and quantification techniques highlighted some disadvantages and possible sources of a scientific bias. To reduce this bias, SHG microscopy was used as a qualitative method for objective type I collagen observation. This microscopy method confirmed the failure of collagen assembly without AA, and additionally confirmed the importance of hydroxyproline for generation of the second harmonic signal by type I collagen. For the further perspectives, the VICs culture does not have to serve only as a model for testing collagen identification techniques, but due to the excellent ECM production dynamics, it can also be used as a cell component of vascular tissue engineering constructs[156].

2.5 Acknowledgement

The study was approved by the Ethics Committee of the Institute for Clinical and Experimental Medicine and Thomayer Hospital in Prague, approval Nos. G 09-12-30, C.j. 2401/09, and G14-08-63, proved on 13th August 2014. The preparation of source pig tissue and cell isolation was primarily conducted by Dr. Elena Filova, prof. Jan Pirk, and Miroslav Konarik. The cell cultures, staining and quantification of collagen expression levels was conducted by Dr. Jana Liskova.

Chapter 3

3 Connective dense tissue: benefits of SHG over fluorescence microscopy

3.1 Introduction

Unlike cell cultures *in vitro*, tissue sections usually represent much thicker and denser specimens. Although the specimens can be observed using conventional light and/or electron microscopy, x-ray diffraction, biochemical analysis, or histological techniques, which often help to reveal important information about collagen, their major disadvantages are related to the destructive multi-step sample preparation[157] and the inability to observe the structures in an intact state or even *in vivo* condition. The multi-step preparation usually includes not just sectioning but also staining, rinsing, (de)hydrating, or fixation with chemicals, which precede data acquisition. These techniques are useful when general information is needed but insufficient for unbiased characterization of 3-D morphology in bulk tissue[135,158]. The inner morphology in bulk tissue is difficult to reveal mainly because of radiation scattering while using light microscopy. For this reason, the investigation is often restricted to superficial imaging[159]. To overcome the superficial limitation, microtome sections must be prepared. Commonly, these microtome sections are histochemically or immunochemically stained (IS). Although IS is a conventional method, the limited penetration of antibodies causes a non-uniform staining intensity through the depth of the sample[160]. Therefore, to guarantee the penetration of antibodies, the experiment requires sections thinner than 40 μm[161]. For very dense tissue, this number can be even smaller. On the other hand, the methods based on multiphoton excitation offers the penetration of a 100μm order into the sample[157] as near infrared (IR) light significantly extends imaging depth[117,147]. Consequently, microtone sections can be thicker, and thus the observed intact sample volume becomes larger. These methods also cause less photodamage to samples as there is no photobleaching and photoxicity out of focus and do not require a pinhole compared to single photon confocal microscopy[121]. To avoid the staining completely, SHG microscopy is a perfect label-free approach for some biological structures (see Chapter 1)[113]. This advantage dramatically helps to decrease the number of sample preparation steps.

Connective dense tissue: benefits of SHG over fluorescence microscopy

In this chapter, common single photon fluorescent microscopy is qualitatively compared with label-free microscopy (SHG and PSHG) on collagenous structures in the stained microtome sections.

3.2 Material and methods

3.2.1 Animal studies: microtome sections

Eight 20µm microtome sections from a 31-month-old New Zealand white rabbit tendon (*tendo calcaneus communis*) were fixed with acetone for 10 minutes. The same number of microtome sections was left unfixed. Then all the samples were rinsed with phosphate-buffered saline (PBS) and left in 10% TWEEN for 20 minutes. After that, the microtome sections were incubated overnight with a primary antibody (Anti Type I Collagen, rabbit, dilution 1:200 in PBS, Cosmo Bio Co., Japan) or left only in PBS as a control group (4 microtome sections in total) at 2 – 8°C. On the next day, all the microtome sections were washed twice in PBS, incubated with the secondary antibody Alexa Fluor® 488 (goat anti-rabbit, dilution 1:400 in PBS, A11070, Invitrogen, USA) for one hour and again rinsed twice with PBS. The fluorescent immunostained microtome sections were measured the second day after the slaughter according to Section 3.2.2.

3.2.2 Sections visualization using fluorescence and SHG microscopy

The system was identical to the one in Chapter 2, Section 2.2.4, Figure 2.1. It consisted of a confocal scanning head (Leica TCS SP2 AOBS, Germany) mounted to an inverted microscope (DMIRE2, Leica, Germany). For SHG microscopy of the microtome sections, a femtosecond tunable pulse laser (Ti:Sapphire Chameleon Ultra, Coherent Inc., USA) was set to 860 nm and the linearly polarized incident beam reached the sample through an objective (Leica HC PL APO 20x/0.7 IMM CS, image resolution of 1024x1024 pixels, and pixel size of 732 nm). The detection of the SHG signal was in backwards, non-descanned mode. To guarantee the SHG selectivity, an IR blocking filter (703HSP, Laser Components GmbH, Germany) and a single band-pass filter (HQ430/20 M-2P, Chroma, USA) were placed before a photomultiplier tube (PMT4) detector. For single photon fluorescence microscopy, the microtome sections were excited by Argon-ion laser at 488 nm, and the signal was detected in

descanned mode. The internal PMT2 detector was set from 490 nm to 570 nm (filter-free AOBS system). For both methods, the microtome sections were measured under three polarization angles (0° – horizontal x axis, 60°, and 120°) of the incident laser beam. The polarization was changed by using a half wave-plate at the excitation path.

3.3 Results

3.3.1 Immunostaining and polarized SHG microscopy

The fluorescently stained 20µm sections appeared fuzzy with no details even under polarized light microscopy (Fig. 3.1(b)). When comparing the images obtained by both fluorescence microscopy and label-free SHG microscopy, SHG exhibited excessive advantages. Unlike for IS, the individual fibers were detectable (Fig. 3.2), and due to the incident polarization dependency of collagen structures, it was possible to reveal the local fiber orientation (Fig. 3.1(a)).

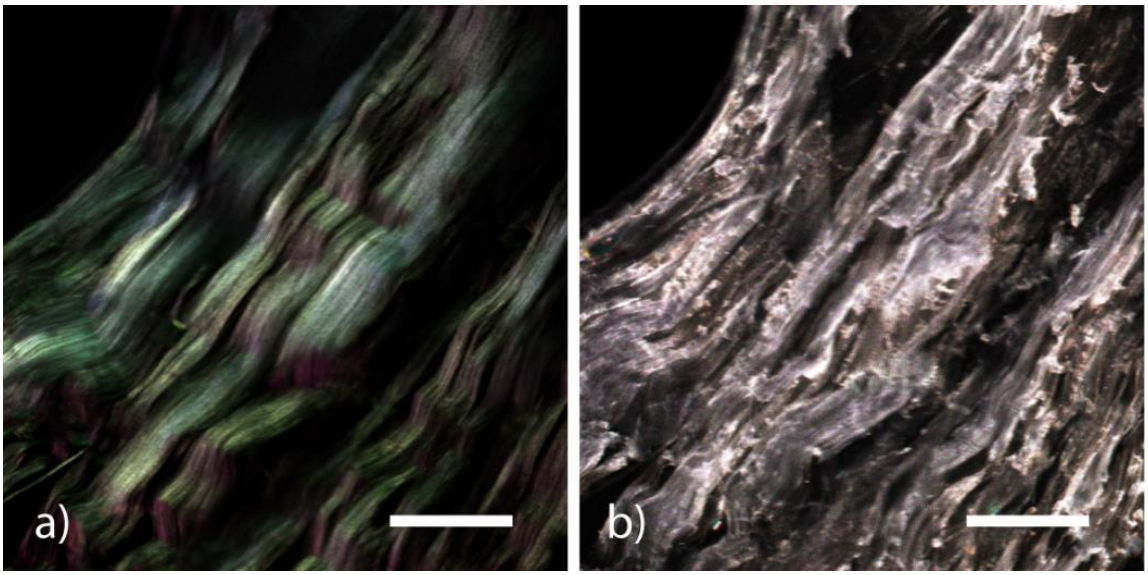

Fig. 3.1 Polarized SHG and IS images of tendon microtome sections. The comparison between a composition of three polarized images of (a) SHG and (b) IS images. The pixel color and intensity reflects the type I collagen presence at certain incident beam polarization. For the red (0° polarization), green (60°), blue (120°) color scheme, the pixel color independent on the polarization angles appears white. The SHG images showed clear polarization dependency. Scale bar = 100 µm.

Additionally, the sample fixing did not improve the staining as the images from the fixed and unfixed sections were alike. The SHG signal was also not affected by the fixing protocol or the storage/preparation time and was clearly detectable the second day. Undesirably, there was even a dim signal acquired from the images of the fluorescently stained control group. This was mainly caused by the difficulty to completely rinse the secondary antibody out of the dense tissue.

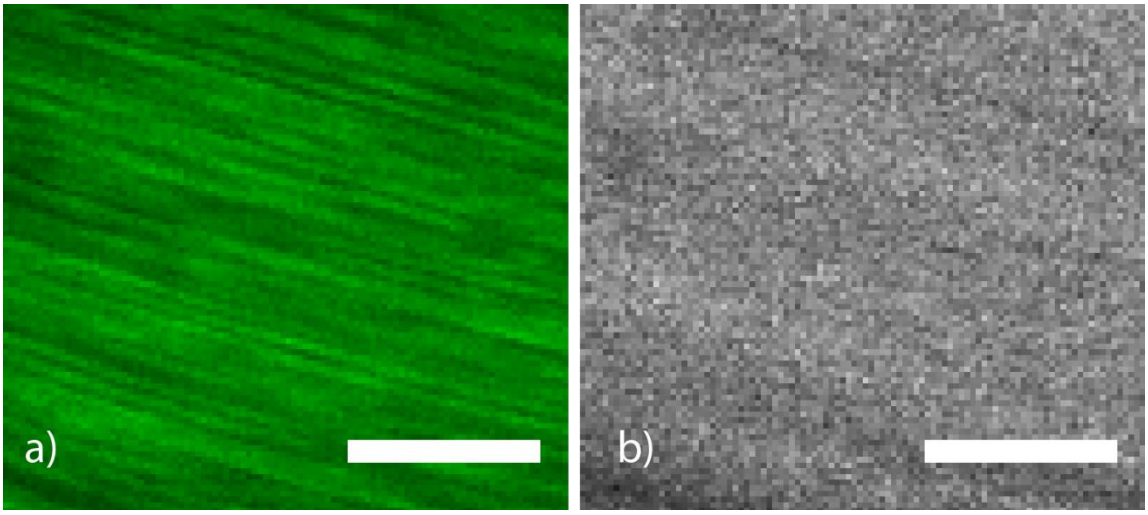

Fig. 3.2 SHG and IS detail of fibres. The crop images of (a) SHG and (b) IS signal from the same sample illustrates the difficulties to identify collagen structures in IS images. On the one hand only contours can be identified in the IS image, but on the other hand many individual fibers can be observed in the SHG images. This advantage appears even when using a low resolution objective. The images were acquired under horizontally polarized laser light. Scale bar = 25 µm.

3.4 Discussion and conclusion

To identify a specific feature in tissue microtome sections, IS staining is a standard approach[162]. Collagen is normally stained with Masson's trichrome, picrosirius red or labeled immunofluorescently for fluorescence microscopy, but these methods have some drawbacks when used for accurate scoring[163]. As demonstrated above, these major drawbacks are, when performed on relatively bulk dense tissue, the time delay before imaging, the difficulties in revealing the fibrillar details, high toxicity, 2-D plane limitation, and epitope accessibility. In addition, it is highly probable that the multiple sample washing and bathing steps change

the hydration level in the sample. This leads to a different tissue volume and mechanical properties[10].

On the other hand, the method of SHG microscopy utilizes the high specificity for type I collagen fibrillar structures. It reveals the collagen organisation in higher fibrillar resolution and deeper penetration depth[164]. There was no difference found when comparing the SHG images of fixed and unfixed microtome sections. This result is consistent with previous study[163]. In addition, the PSHG microscopy also showed the possibility of returning the orientation of collagen fibres instantly[105,123], although this technique requires multiple sample scanning under different laser polarization angles, and therefore an increase of the observation time and possible sample photodamage.

To minimize the observation time and possible damage of unstained, unfixed microtome sections (biopsy), intact tissue samples (tendons) or even *in vivo*, a single scan image is sometimes unavoidable. In this case, an objective quantitative tool is required to compare the fibrillar organization in such an image. This area is challenged in Chapter 4 and the solution is adopted to determine the influence of microtome sectioning to morphology of tendon.

3.5 Acknowledgement

The microtome sections were prepared and stained in cooperation with Dr. Marketa Bacakova, Department of Biomaterials and Tissue Engineering, Institute of Physiology, the Czech Academy of Sciences, Videnska 1083, 14220 Prague, Czech Republic.

Chapter 4

4 Unravelling collagen fibre orientation in tendon microtome sections

4.1 Introduction

Performing microscopy on dense bulk tissue is often restricted due to light scattering[159]. Therefore structures that contain a large amount of connective tissue or structures that cannot be directly accessed have to be cut into microtome sections (biopsies). Then, these sections are used to conclude on subject's health or age. These conclusions are often based on tissue biochemical properties or morphology. However, as stated in the previous chapters, microtome sectioning can alter the morphology[165,166], and consequently bias the results. These alternations of morphology usually happen in a homogeneous or differential, isotropic or anisotropic, uniform or non-uniform manner[165], and they are caused by a number of scenarios, for example, shrinkage at unfixed samples[135,166]. Another scenario, mostly investigated among blood vessels, includes the presence of residual stresses. These stresses remain in the sample, although the sample is not subjected to any external loads. Theoretically the stresses are completely released when the sample is cut into infinitesimal elements, but in practice most stresses are released during initial cuts[167]. Each stress release induces deformation in the sample which is projected into the spatial distribution of the extracellular matrix elements. Therefore, the image of the observed elements, for example, collagen or elastic fibres, can appear differently compare to living tissue *in vivo*[165]. To distinguish among the differences objectively, an automated 2-D or 3-D element detection technique is crucial.

In general, the orientation of microstructures in a collagen fibrous network is often calculated from polarization light microscopy images[168,169]. However, this technique requires images acquired under different polarization angles, and materials that possess birefringence. Therefore more universal techniques are developed to deal with the geometrical description of fibrous features. The most common methods rely on a convolution product of a kernel and an image and mostly uses the gradients of image intensity[170,171], fractals[172], the Hough[173], Fourier[174], Gabor[175], Wavelet transform[176], or their combination[177].

In this chapter, not only the fibre orientation analysis from a single image is introduced, but also the orientation regularity (changes in orientation of fibres with distance in longitudinal

plane) is expressed in correlogram. Finally, this technique is applied to the images of the microtome sections from the tendons to compare their fibrous networks in respect to sectioning and age.

4.2 Material and methods

4.2.1 Animal studies: microtome sections

The rabbit Achilles tendons (*tendo calcaneus communis*) were investigated from 6 New Zealand white, Czech Spot, and Belgian Hare crossbred rabbits of the age of 4 weeks, 5 weeks, 4 months, 9 months, 31 months, and 38 months old. These animals represent the main developmental stages, from newborn (up to 6 weeks) to sexual mature (5 to 7 months), and to older age (up to 5 – 7 years) rabbits[178,179]. The animals were bred in hutches and exhibited healthy physical conditions. The legs were received as animal waste product and processed immediately after slaughter. The tendons were dissected from both left and right hind legs and mounted with Cryomount (Histolab Products AB, Sweden) on dry ice and then cryocut into 20µm sections (zero-stress state) with a cryostat (Leica CM1850, Leica, Germany) at -24°C. The microtome sections were performed in steps of 100 µm along the 1 mm depth from the tendon's surface. All the samples were prepared for microscopy within 30 minutes after the slaughter, placed on microscopy glass and measured by the protocol in Section 4.2.2.

4.2.2 SHG microscopy of microtome sections

The experiment was conducted on the same system as in Chapter 2 and Chapter 3, i.e. a confocal scanning head (Leica TCS SP2 AOBS, Germany) mounted to the inverted DMIRE2 (Leica, Germany) microscope and coupled with a femtosecond tunable pulse laser (Ti:Sapphire Chameleon Ultra, Coherent Inc., USA). The excitation wavelength was set to 860 nm, and the incident beam reached the sample through an objective (HCX PL APO 63x/1.20 W, image resolution of 2048x2048 pixels, and pixel size of 58 nm). This spatial resolution was sufficient for the identification of individual fibres and suitable for the application of the fibre orientation analysis in Section 4.2.3. The detection of the SHG signal was in backwards, non-descanned mode. To guarantee the SHG selectivity, an IR blocking

filter (703HSP, Laser Components GmbH, Germany) and a single band-pass filter (HQ430/20 M-2P, Chroma, USA) were placed before a photomultiplier tube (PMT4) detector. The microtome sections were measured at one angle of the horizontally polarized laser beam.

4.2.3 Fibre orientation analysis and comparison

The structural organization of unstained microtome sections was quantified through the fibre orientation regularity. In this approach, the fibre orientation was given by the local tensor representation[180]. First, the image was scanned with a 16 x 16 pixel sliding window that moved over the image coordinates x, y with an 8-pixel step. Each 16 x 16 pixel window-cropped image was transformed into the frequency domain by Fast Fourier Transform (FFT). The major peak $G_{i,j}$ of the centred FFT modulus $|F_{i,j}|$ was established using reconstruction by dilation[181] of the modulus $|F_{i,j}|$ around the central pixel. The structure tensor $J_{\xi,\eta}$ was calculated from the 2nd order moments

$$J_{\xi,\eta} = \begin{bmatrix} \sum_{i,j} G_{i,j}\,(i-\bar{\imath})^2 & \sum_{i,j} G_{i,j}\,(i-\bar{\imath})(j-\bar{\jmath}) \\ \sum_{i,j} G_{i,j}\,(j-\bar{\jmath})(i-\bar{\imath}) & \sum_{i,j} G_{i,j}\,(j-\bar{\jmath})^2 \end{bmatrix} = \begin{bmatrix} J_{11} & J_{12} \\ J_{21} & J_{22} \end{bmatrix}, \qquad (4.1)$$

where $1 \le i \le 16, 1 \le j \le 16$, $\bar{\imath} = \bar{\jmath} = 8.5$, $J_{12} = J_{21}$.

Here is a 2 x 2 symmetric tensor $J_{\xi,\eta}$ for each rescaled pixel ξ,η where $\xi = \frac{x}{8}, \eta = \frac{y}{8}$. Indirectly, the matrix defines the values for hue, saturation, and value (HSV) colour format. Inspired by Jähne[180], the hue 2φ was calculated by rotating the structure tensor into the canonical coordinate system by angle $-\varphi$. The matrix multiplication yields the pixel orientation angle φ as

$$\tan 2\varphi_{(\xi,\eta)} = \frac{2J_{12}}{J_{22}-J_{11}}, \text{ where } \varphi \in <0, \pi>, \qquad (4.2)$$

the value v (pixel brightness) as the trace of the tensor,

$$v_{\xi,\eta} = J_{11} + J_{22}, \qquad (4.3)$$

and the saturation s as a coherency measure calculated from J_{11}, $J_{12,}$ J_{22} as

$$s_{\xi,\eta} = \frac{\sqrt{(J_{11}-J_{22})^2+4J_{12}^2}}{J_{11}+J_{22}}. \tag{4.4}$$

Finally, the HSV image is converted to the red-green-blue (RGB) format. The changes in colour and intensity code for the orientation irregularity.

To interpret the data objectively, the fibre organization in the image was computed through an autocorrelation approach using the aforementioned spatial variables: orientation angle $\varphi_{\xi,\eta}$, value $v_{\xi,\eta}$, and saturation $s_{\xi,\eta}$. First, the complex value $p_{\xi,\eta}$ for each pixel is calculated as trigonometric functions

$$p_{\xi,\eta} = v_{\xi,\eta}s_{\xi,\eta}\left(cos\,2\varphi_{\xi,\eta} + \boldsymbol{i}\,sin\,2\varphi_{\xi,\eta}\right), \tag{4.5}$$

where $\boldsymbol{i}$ is the imaginary unit. Then the complex $c_{k,l}$ and modulus $r_{k,l}$ autocorrelation functions for $p_{\xi,\eta}$ were calculated as

$$c_{k,l} = \sum_{r=0}^{R-1}\sum_{s=0}^{S-1} p_{r,s}\bar{p}_{r+k,s+l} \tag{4.6}$$

and

$$r_{k,l} = \sum_{r=0}^{R-1}\sum_{s=0}^{S-1}\left|p_{r,s}\right|\left|p_{r+k,s+l}\right|, \tag{4.7}$$

where $0 < k \leq R-1$, $0 < l \leq S-1$, $\bar{p}$ denotes the complex conjugate of p, $\left|p_{r,s}\right|$ and $\left|p_{r+k,s+l}\right|$ the moduli, and $p_{r,s} = 0$ if $\xi > R-1$ or $\eta > S-1$ for the zero padded $p_{r,s}$.

In the next step, the distances in the image were sectioned into 32 equal annular intervals by $d_m = \frac{x-size\ of\ the\ image}{32}$. The returned autocorrelation ratios $\frac{|c_{k,l}|}{r_{k,l}}$ were subscribed to these relevant intervals according to distance $d = \sqrt{i^2+j^2}$ where $d_m \leq d < d_{m+1}$. The resulting

values for the correlogram $C(d_m)$, where m is the interval/bin number, were calculated as the average values of the n_m ratios $\frac{|c_{k,l}|}{r_{k,l}}$ in each m, i.e.

$$C(d_m) = \sum_{d_m=1}^{m} (M)_{d_m}, \tag{4.8}$$

where

$$M = \frac{1}{n_m} \sum_{q=1}^{n_m} \left(\frac{|c_{k,l}|}{r_{k,l}} \right)_q . \tag{4.9}$$

The $\frac{|c_{k,l}|}{r_{k,l}}$ ratio was used to emphasize the role of orientations in autocorrelations. For a perfectly oriented isotropic pattern, $C(d_m)$ equals 1. The resulting graphs were fitted with an exponential model $y = Be^{-Cx} + D$ where B, C, and D are freely adjustable parameters. The coefficient of determination was calculated, and the residual plot was performed. Models that explained more than 90 % of the variability of the data were subjected to further statistical analysis.

4.2.4 Statistical analysis

The data were checked for normality (S-W test, Q-Q plot) and after that tested by the Kruskal-Wallis or One-way ANOVA followed by a post-hoc test (Dunn and Sidak, Tukey's HSD respectively)[182]. If not stated otherwise, the results are published as means with sample standard deviations. The significant value for rejecting the null hypothesis is set to p-value < 0.05. The data analysis was performed in Microsoft Visual C++ 2013 (Microsoft, USA) and Matlab 2015a (Mathworks, USA). The statistical evaluations were performed by using Matlab 2015a.

4.3 Results

4.3.1 Unstained microtome sections and orientation regularity analysis

The images of unstained microtome sections indicated that the collagen structural organization is age dependent (Fig. 4.1 – Top row). The images of microtome sections from the young animals seemed to have less regular pattern of collagen fibres then the sections from the older animals. The oldest animals possessed the collagen fibres of a straight flat pattern. To express the organization in the microtome sections quantitatively, the orientation of fibres was calculated by the algorithm in Section 4.2.3 and then visualized as the pseudo-HSV-colour coded images (Fig. 4.1 – Bottom row).

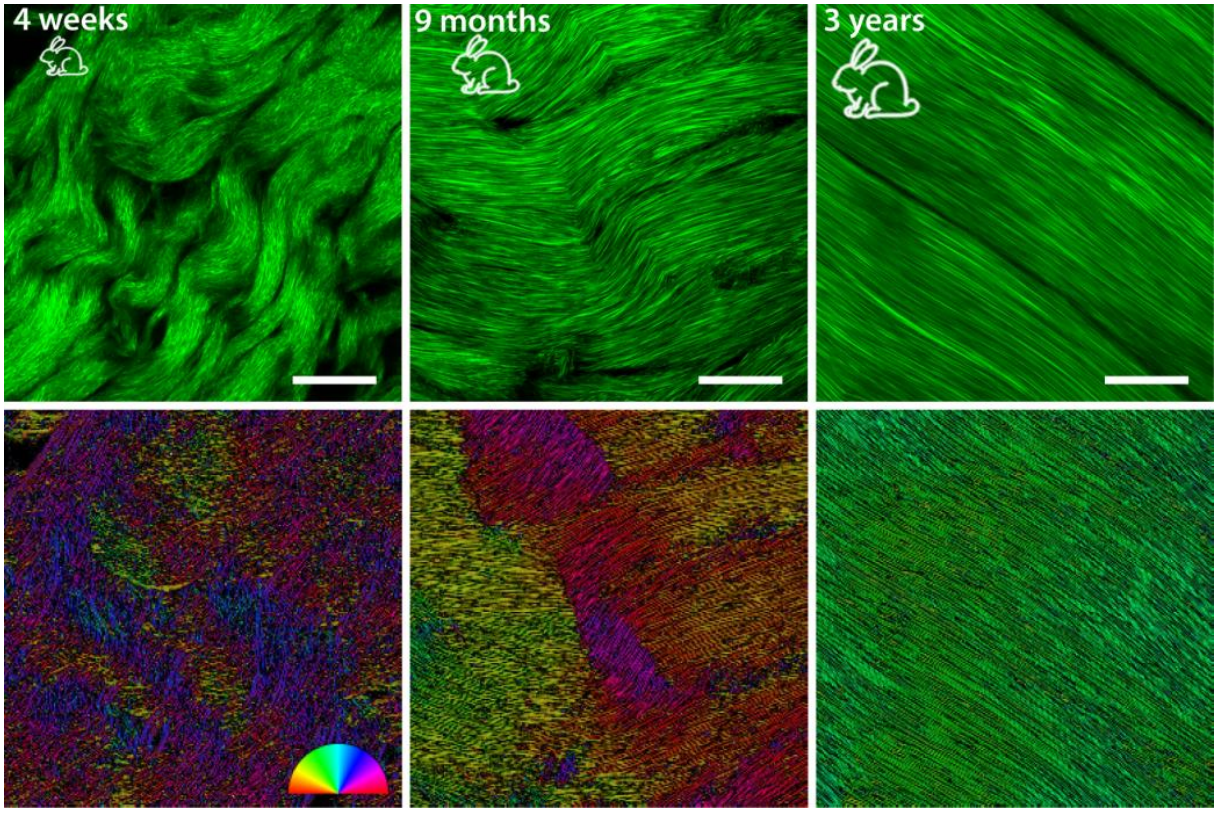

Fig. 4.1 SHG images of aging rabbit tendons and colour coded analysis. Top row: SHG images of the microtome sections displayed differences in the structural pattern between 4-week, 9-month and 3-year-old animals. Bottom row: pseudo-coloured RGB images returned by the fibre orientation regularity analysis (Section 4.2.3) of the corresponding top row images. The different colour tone symbolizes the change in orientation of the fibres. The higher is the intensity, the more uniform is the structural pattern in the 16 x 16 pixel analysed window. Scale bar = 25 μm.

The colourful images with rapid colour changes were returned for the younger animals. In contrast, almost single-colour images were returned for the oldest animals. This analysis confirmed the assumption which was based on the original images. Furthermore, the numerical results were used for the quantification of the orientation regularity.

The orientation regularity is represented by a converging graph in correlogram. The correlograms indicated that the fibres in the microtome sections from the very young animals change directions rapidly with distance and these changes do not follow a periodic, regular, crimp pattern. On the other hand the fibres in microtome sections from the older animals are perfectly aligned within the longitudinal axis of the tendon, i.e. the value in correlogram is close to one and does not change with distance (Fig. 4.2 (a)).

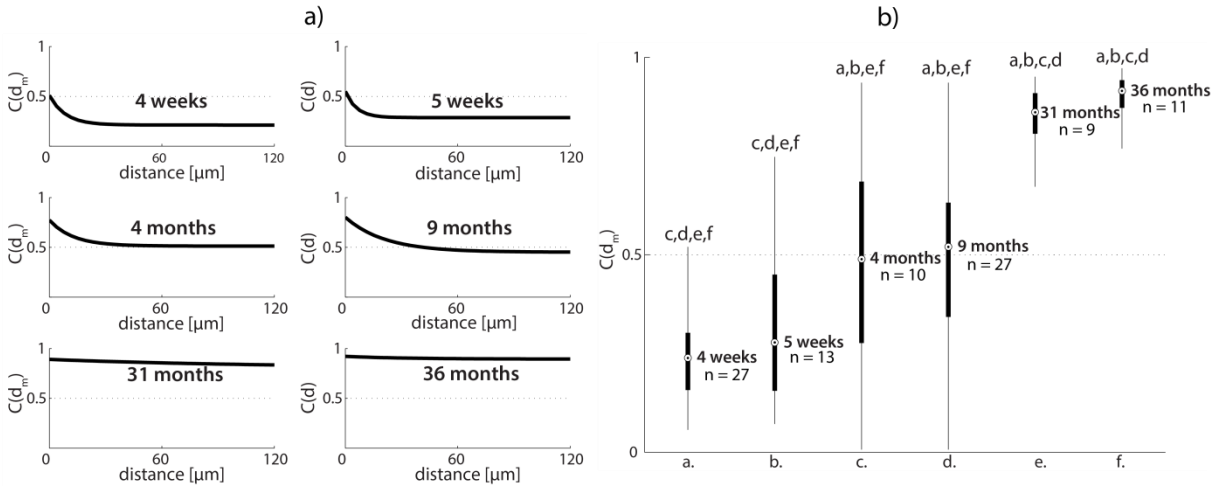

Fig. 4.2 Orientation regularity correlograms. (**a**) The orientation regularity disappears with distance and starts at lower levels of $C(d_m)$ in the microtome sections from the younger animals. The fibre structures remain within the expected, longitudinal axis of tendon in the sections from the older animals. (**b**) The main three developmental stages (Section 4.2.1) are clearly visible from the box-and-whisker plot. The significant difference between the groups is indicated above each boxplot. The target mark highlights medians, the black boxes 25th and 75th percentiles and the whiskers maximum/minimum. *n* equals to the number of analysed images.

The overall trend for the three main developmental stages is clearly visible from the data distribution presented in the box-and-whisker plot (Fig. 4.2 – (b)). The plot suggests that with increasing age of tendon the orientation regularity inclines towards perfect fibrillar orientation anisotropy in the microtome sections.

4.4 Discussion and conclusion

The results revealed significant differences between the collagen fibres orientation in the young and old animals. The orientation regularity differed especially among the main developmental stages. This is of great importance for biomechanical constitutive models that simulate the mechanical properties of connective tissue. These models often contain a parameter that represents the microscopic information about the fibre organization[183,184]. This information can be directly projected into the scaffold design because regenerative medicine requires scaffolds with a specific orientation[185]. The orientation vector field is commonly presented by a colour-coded scheme[186]. For example, a simple RGB map offers one colour for each circular sector. This simplification causes a reduction in sensitivity for orientation detection[187] and neglects the dependency of neighbouring pixels. On the other hand, our algorithm respects the coherency of the fibres by adjusting the pixel saturation and brightness. These results are then used to characterise the orientation within a pixel by a complex number. These complex numbers were used for autocorrelation functions. The autocorrelation functions described spatial inhomogeneity in the scalar fields. To prioritize the orientation, the complex autocorrelation function was divided by the modulus (saliency) autocorrelation, and the returned correlogram quantified anisotropy of the fibres within the images. This approach is fully automatic and decreases the sample photodamage and the acquisition time because the image collection is not required at different polarization angles of the incident laser beam.

Based on the results, the fibres in the samples from the young animals possessed orientation isotropy. The samples from the older animals contained exclusively anisotropic fibres. If this trend is caused by the sectioning, a possible explanation includes, for example, the presence of fibril ends which disappear in mature tissue[78] or a lower number of cross-links[29] at early developmental stages. These both would lead to a fewer connection points among the basic fibrillar collagen structures in the young animals, and therefore, more pronounced deformation after sectioning. To confirm whether the changes in the fibre orientation are triggered by sectioning, the dissected intact rabbit tendons are investigated in Chapter 5.

Chapter 4

4.5 Acknowledgement

The microtome sections were prepared with Dr. Eva Filova, Institute of Experimental Medicine, Department of Tissue Engineering, the Czech Academy of Sciences, Videnska 1083, 14220 Prague, Czech Republic. The orientation regularity analysis was completed in co-operation with Dr. Jiri Janacek, Department of Biomathematics, Institute of Physiology, the Czech Academy of Sciences, Videnska 1083, 14220 Prague, Czech Republic.

Chapter 5

5 Collagen crimps development in intact tendon

5.1 Introduction

In the previous chapter, a significant difference was found in the collagen fibre orientation among the tendon microtome sections from the young and old animals. However, it was not possible to determine whether the difference was associated with the sample processing, aging, or both. In this chapter, the dissected intact load-free tendons are investigated for the collagen fibre organization to question this problem.

The collagen fibre organisation is usually aligned longitudinally to the loading axis of tendon[188]. In this alignment, a 2-D regular zig-zag wavy pattern, termed the crimp pattern, is observed by using polarization light microscopy. The function and development of the crimp pattern remain unknown[62]. For example, it has been proposed that the crimp structure and appearance is linked to contraction of tendon fibroblasts[189] or a sudden twist in the fibrils direction that is marked by knots/hinges[190]. However, no unique specialized structure was found for the hinge region[191]. This crimp pattern is usually represented by two parameters; length and angle/height[60,192]. However, these parameters often varies among different studies depending on species, anatomical location, region within tendon, strain of the tendon or loading history[60]. A common crimp pattern oscillates with the periodicity between 10 μm and 100 μm. The variability in the crimp amplitude is lower (~ 5 μm)[193]. A certain disagreement is also found in studies which compare the crimp length and angle with respect to aging. Patterson-Kane et al. published that both the crimp length and angle had a decreasing trend with age. The angle started at 26.7 degrees for the foetal horses and reached 10.5 degrees for the old horses in the central region of superficial digital flexor tendon. The crimp length parameter was 38.7 μm for the foetal group and 17.9 μm for the old one[192]. Legerlotz et al. published crimp height and length data on mouse tail tendon fascicles[60]. The height varied from 3.04 μm (3 weeks), 4.46 μm (9 weeks), and to 3.21 μm (9 months). The measured length reached the minimum value of 100 μm at 3 weeks, then increased to 156 μm at 9 weeks and then kept decreasing to 138 μm at 6 months. These results confirm the heterogeneity of the

results and consequent discussions about the factors which influence the crimp parameters, for instance, cell-matrix interactions, cross-links increase, or exercise. To better understand the development of the crimp pattern and its impact on the mechanical behaviour of the tendon, the crimp pattern was investigated under SHG microscopy in the intact Achilles tendons. These tendons possess a well-defined loading characteristic and a clear function. In addition, the results are confronted with the results of the microtome sections in Chapter 4.

5.2 Material and methods

5.2.1 Animal studies: intact tendons

The rabbit Achilles tendons (*tendo calcaneus communis*) were investigated from 13 New Zealand white, Czech Spot, and Belgian Hare crossbred rabbits. Their age ranged from 7-day to 38-month-old to include all the developmental stages mentioned in Chapter 4, Section 4.2.1. The animals were bred in hutches and exhibited healthy physical conditions. The legs were received as animal waste product and tendons were carefully dissected from both left and right hind legs. The protocol was identical to that in Section 4.2.1, except no additional sample sectioning or other processing. All the samples were prepared for microscopy within 10 minutes after the slaughter and measured by the protocol in Section 5.2.2.

5.2.2 Tendon visualisation using SHG microscopy

The microscope image acquisition was performed on two independent systems in order to increase the robustness of the investigation. The first system (System I – previous chapters) consisted of a confocal scanning head (Leica TCS SP2 AOBS, Germany) mounted to the inverted DMIRE2 microscope (Leica, Germany) and coupled with a femtosecond tunable pulse laser (Ti:Sapphire Chameleon Ultra, Coherent Inc., USA). The laser was set to 860 nm, and the horizontally oriented linearly polarized incident beam reached the sample through an objective (HC PL APO 20x/0.7 IMM CS, image resolution 1024x1024, pixel size 732 nm). The detection of the SHG signal was in backwards, non-descanned mode. To guarantee the SHG selectivity, an IR blocking filter (703HSP, Laser Components GmbH, Germany) and a single band-pass filter (HQ430/20 M-2P, Chroma, USA) were placed before a photomultiplier tube (PMT4) detector.

The second system (System II) consists of a confocal scanning head (Zeiss LSM 510 META, Zeiss, Jena, Germany) mounted to the motorized inverted Axiovert 200M (Zeiss, Germany) and coupled with a femtosecond tunable pulse laser (Mai Tai DeepSee, Spectra-Physics, USA). The 810 nm horizontally oriented linearly polarized incident beam entered the samples through an objective (Plan-Apo 20x/0.75 dry, image resolution 2048x2048, pixel size 220 nm, Zeiss, Germany). In the emission pathway, the light was collected in the forward direction passing through an in-house built condenser with an adjustable numerical aperture (0 to 0.8)[194], the appropriate set of filters (FT 442, Zeiss, Germany and BP 405/10, Semrock, USA) and entering a multi-alkali PMT detector.

The samples were placed on microscope cover slips in their load-free state and left uncovered to prevent deformation. The intact samples were scanned by System I or System II in three central XY positions of the tendon from the top to an average depth of 100 µm.

5.2.3 Crimps analysis and comparison with microtone sections

In the intact samples, the amplitude and wavelength were extracted manually (Fig 5.1).

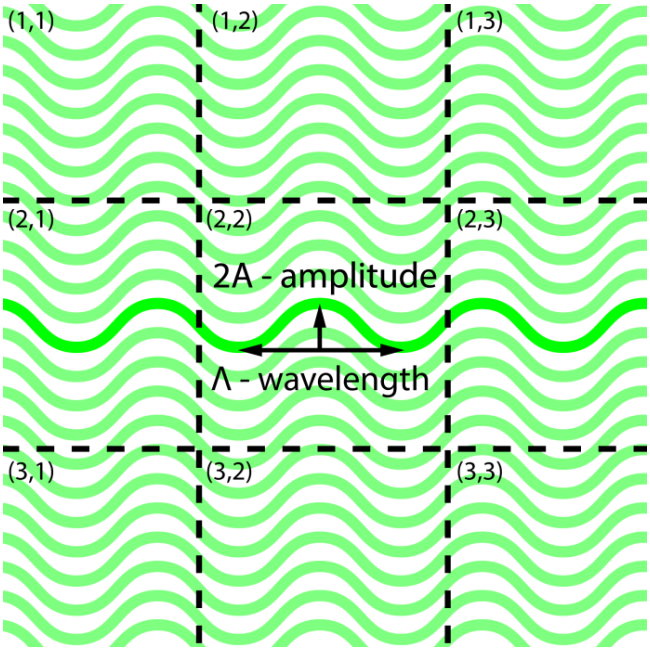

Fig. 5.1 Manual crimp analysis. The acquired images were divided by a 3 x 3 selection grid. For each field of the grid, crimp amplitudes and wavelengths were calculated from a triangle that connects three adjacent extremes (arrows) of the crimp pattern for a single fibre.

Based on this manual measurement, the mean crimp amplitude and wavelength were stated for each age group, and the results were simulated in a grayscale value image $I_{(x,y)}$ using

$$I_{(x,y)} = \sin(2\pi F(x + A\sin(\frac{2\pi y}{\Lambda}))), \quad (5.1)$$

where x, y are the coordinates of the image, F defines the thickness of the fibres, Λ is the measured wavelength of the crimp pattern, and A stands for the measured amplitude of the crimp pattern. After that, these simulated grayscale value images were analysed by the same algorithm as the images of the microtome sections in Chapter 4. The results were again expressed in correlogram. Finally, the correlograms for simulated images of the intact samples C_{sim} and microtome sections C_{sec} from Chapter 4 were compared by mean percentage difference (MPD) of the points

$$MPD = \frac{1}{n}\sum_{d=1}^{n}\frac{|C_{sec}(d)-C_{sim}(d)|}{(C_{sec}(d)+C_{sim}(d))/2} \times 100, \quad (5.2)$$

where n = 32 bins.

5.2.4 Statistical analysis

The data were checked for normality (S-W test, Q-Q plot) and after that tested by the Kruskal-Wallis or One-way ANOVA followed by a post-hoc test (Dunn and Sidak, Tukey's HSD respectively)[182]. If not stated otherwise, the results are denoted as means with sample standard deviations. The significant value for rejecting the null hypothesis is set to p-value < 0.05. The data analysis was performed in Microsoft Visual C++ 2013 (Microsoft, USA) and Matlab 2015a (Mathworks, USA). The statistical evaluations were performed by using Matlab 2015a.

5.3 Results

5.3.1 Crimp pattern development with age

The organization of the collagen fibres in the load-free intact samples possessed a 3-D frequency modulated pattern with great crystallinity. In contrast to the microtome sections in Chapter 4, a highly regular crimp pattern was identified for all the age groups including the youngest one (Fig. 5.2).

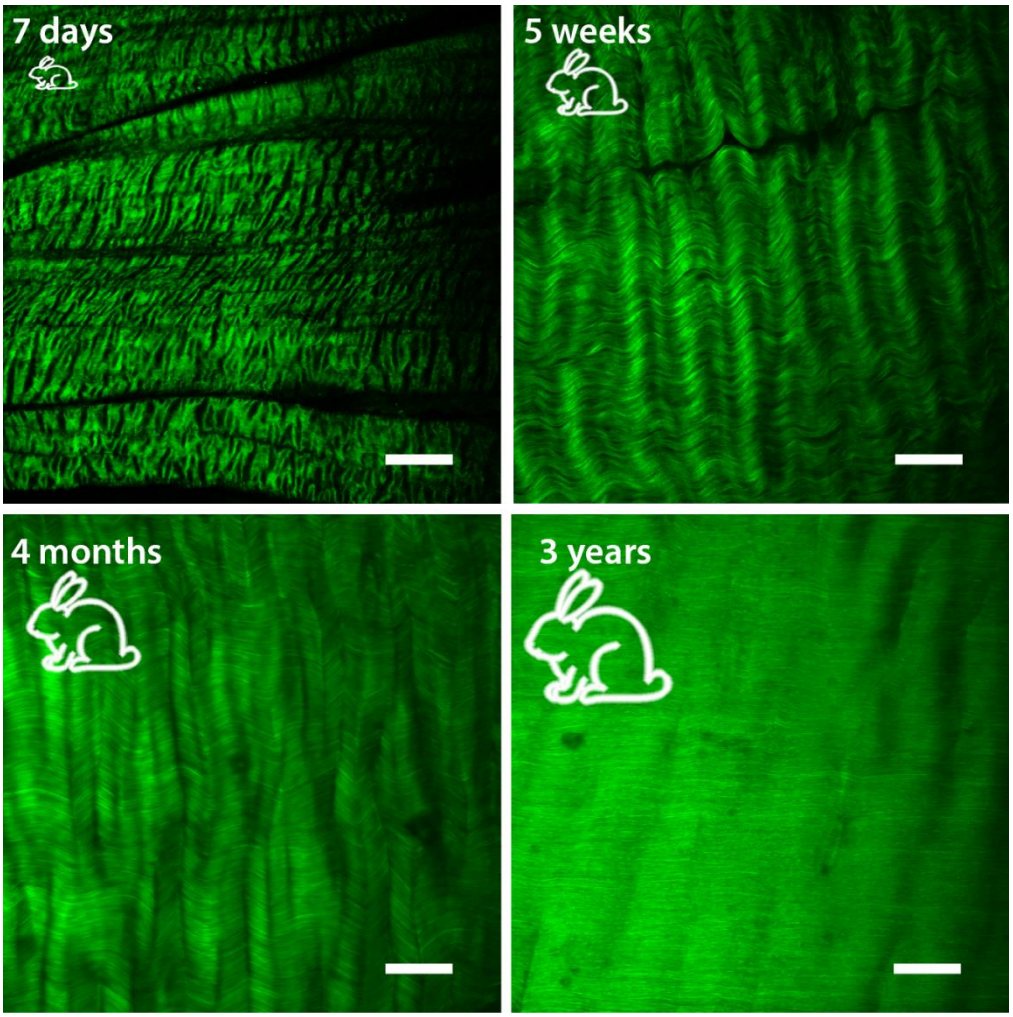

Fig. 5.2 Images of crimp pattern for different age. The global collagen orientation is predominantly arranged parallel to the longitudinal axis of the tendon in the intact samples. This axis is thought to be the main load-bearing axis, and the global orientation is naturally age-independent. In contrast, the local collagen orientation is highly age-dependent. The regular collagen crimp pattern propagates at a certain height/amplitude and periodicity/wavelength through the tendon. Scale bars = 100 µm.

The crimp pattern development with age is quantified in Table 5.1.

Table 5.1 Quantification of crimp pattern development with age. The development was quantified by the amplitude A and wavelength Λ.

Age	7 days	11 days	4 weeks[$]	5 weeks	4 months	6 months[$]	9 months	18 months[$]	36 months	38 months
Animals	2	1	2	1	1	1	2	1	1	1
Tendons	4	2	3	2	2	2	3	2	2	2
Crimps	45	154	30	152	70	28	71	18	10	90
***A* [µm]**	2.0 ± 0.6	2.3 ± 0.8	4.0 ± 1.0	6.2 ± 1.9	9.6 ± 3.3	6.2 ± 1.9	5.7 ± 2.1	4.1 ± 1.1	2.7 ± 0.9	3.0 ± 1.1
Λ [µm]	19 ± 4	37 ± 6	43 ± 5	71 ± 13	92 ± 19	91 ± 22	103 ± 23	119 ± 24	122 ± 21	122 ± 32

[$]The animals were measured by System II. Mean ± SD.

Generally, the crimp pattern started undulating with a small amplitude A = 2.0 ± 0.6 µm in the samples from the 7-day-old animal. The amplitude then increased until it reached a maximum of A = 9.6 ± 3.3 µm when the animal is 4-month-old. After that, the crimp amplitude started decreasing until it reached the value of A = 3.0 ± 1.1 µm which is very small compared to the wavelength for the 38-month-old animal. The wavelength started at its minimum for the young animals. It reached the size of Λ = 19 ± 4 µm for the 7-day-old animal and kept increasing steadily to Λ = 122 ± 32 µm for the 38-month-old animal (Fig. 5.3). Together with the low amplitude, it was sometimes very difficult to detect the unbiased crimp pattern for the old animals. In some cases, the crimps disappeared completely for the old animals.

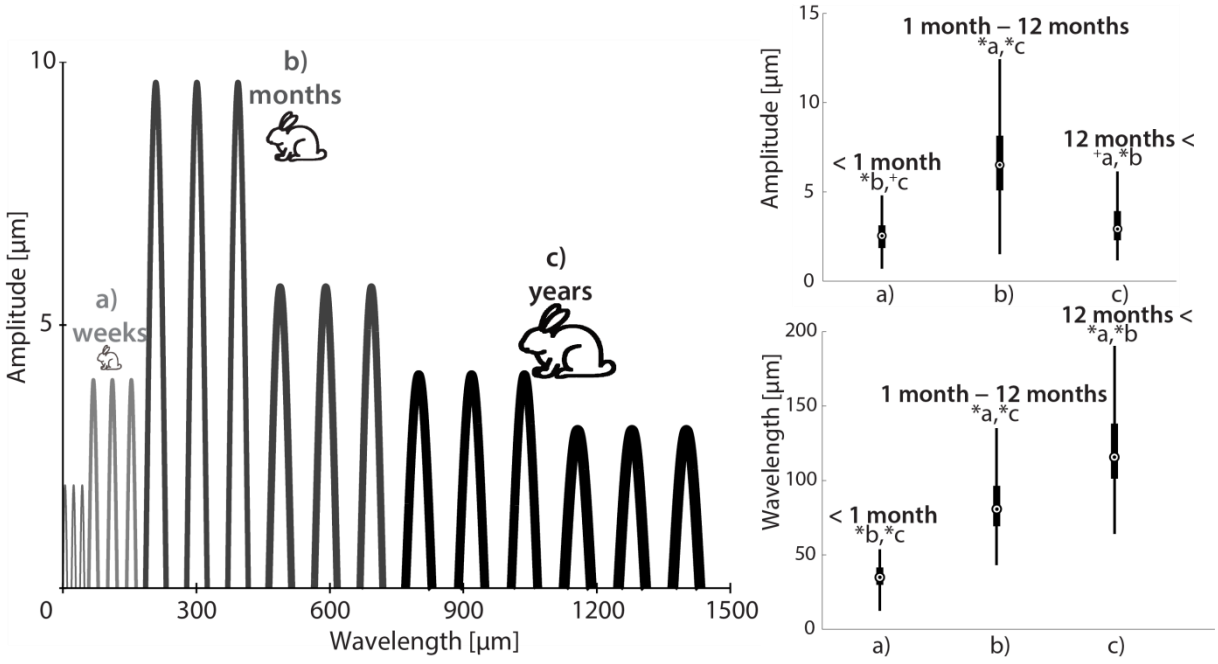

Fig. 5.3 Crimp pattern data distribution for different age groups. Left side: an illustrative comparison of amplitude/wavelength relationship with age. The rapid increase of the crimp amplitude falls on the period of initial walking and physical activity. Once it reaches its maximum at the age of sexual maturity, it starts decreasing steadily with age. Right side: animals of ten different ages were grouped into three developmental stages (Section 4.2.1), and the data are shown in a box-and-whisker plot. The amplitude variability was the highest for the sexually mature group, but for the wavelength it was for the older group. $^{+}$p-value < 0.05, *p-value < 0.01.

5.3.2 Crimp pattern simulation and comparison with microtome sections

In the next step, the mean amplitude and wavelength values acquired from the intact samples were put into Equation 5.1, and the simulated images were analysed likewise the images of the tissue microtome sections (Chapter 4). The returned correlogram for simulated images decreased rapidly for the young animals and consisted of an oscillating pattern. This confirms the possible bias when interpreting morphology from the tissue microtome sections (Fig. 5.4).

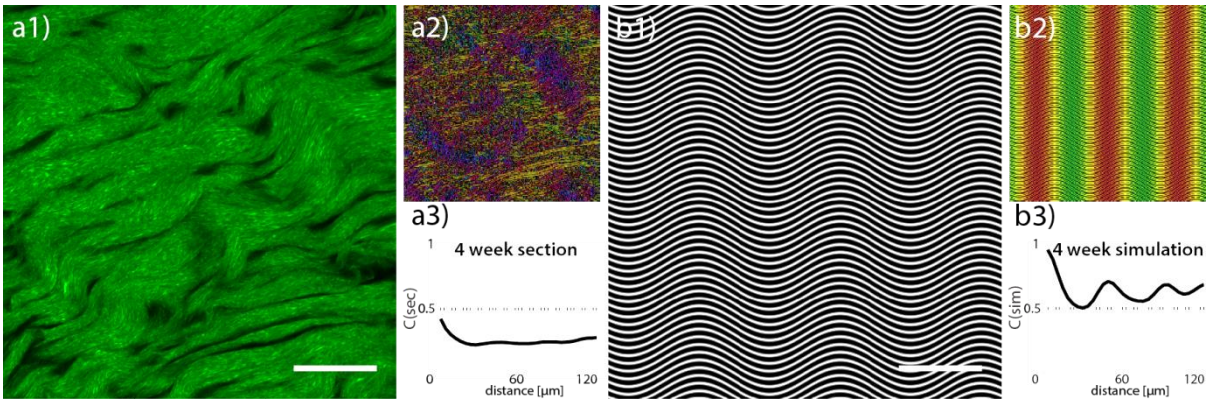

Fig. 5.4 Comparison between microtome sections and intact samples. For 4-week-old animals, the fibres in the microtome section (**a1**) change the orientation randomly and possess a little regularity (**a2**). On the contrary, the simulation preserves the crimp pattern (**b1**). The difference is also detectable by comparing the correlograms (**a3**, **b3**). The MPD returns the value of 46 % for the 4-week-old group. For the 36-week-old animals the MPD reaches only 4.3 %. It indicates that the samples from the older animals are less sensitive to the sectioning. Scale bars = 25 µm.

5.4 Discussion and conclusion

All the intact samples at the load-free state possessed strong orientation regularity of the fibres within the main load-bearing axis. The orientation regularity of the fibres undulated periodically by the crimp patterns. Even the intact samples from the very young animals displayed the crimp pattern. On the other hand, the microtone sections from the young animals had no orientation regularity, and the collagen fibres were organised randomly (Chapter 4). In addition, no regular crimp pattern was observed or identified in the young animals by the analysing algorithm (Chapter 4). When the returned correlograms were compared by the MPD, the difference between the intact and microtome section samples reached 46 % for the young animals. For the oldest animals, the MPD was only about 4 %. This result proves that sectioning modifies the morphology in tendon, moreover, that tendons from the older animals are more rigid than from the young ones. This needs to be considered, especially when examining samples from young subjects or developing tissue engineered constructs.

The crimp pattern parameters vary among the intact samples. On the one hand the amplitude of the crimp pattern exhibited a highly nonlinear dependency on age and reached its maximum at sexual maturity, but on the other hand the wavelength of the crimp pattern seemed to grow steadily with age. This finding is in contrast to what is reported by

Patterson-Kane et al. or Legerlotz et al.[60,192]. Legerlotz et al. found almost no significant differences in the amplitude of crimps, and a decrease in the wavelength at the end of the observed period. Patterson-Kane et al. reported even a more dramatic decrease in the wavelength during the observed period. This contradiction could be caused, for instance, by the sample source. In the Legerlotz et al. study, the rat tail tendon is not a typical muscle-bone connector in the way a rabbit Achilles tendon is. The Achilles tendon is a functional unit of the musculoskeletal system that must withstand enormous loading. This unit guarantees the most efficient force transfer during ontogeny, and therefore it must react to the muscle volume and power changes[42]. Coincidently, these changes have the same trend with age as demonstrated here in the development of crimp amplitude. Furthermore, the tendon water content significantly decreases with age[195]. According to the Gautieri model[10], this fact has a dramatic impact on the mechanical response as the typical stress-strain curve is linearized; no "toe" and "heel" regions are present, and also the microfibrillar stiffness increases. The stiffness of tendon also increases during the tendon mineralization which is also accompanied with the trend of the crimp pattern disappearance[62], or with the increased number of cross-links.

It is clear that the crimp pattern parameters affect the mechanical behaviour of connective tissue and develop during ontogeny. Although the exact impact on mechanical behaviour and reasons for crimp development remain unknown, the detection and modification of the crimp pattern has a massive clinical potential considering the disease diagnosis or regenerative medicine.

Chapter 6

6 Tendon mechanical testing, collagen helical pitch angle and crosslinking

6.1 Introduction

The mechanical properties of tendon were thoroughly discussed in Chapter 1, Section 1.2.2 Mechanical properties and tests. In general, tendon shows strain rate sensitivity, and therefore Young's moduli can differ among mechanical tests. Celmmer et al. also reported the dependency of Young's modulus on the cross-section area, i.e. the smaller cross-section area of fascicles, the higher Young's modulus[73]. The commonly stated values of stress reach from tens to hundreds of MPa for failure strains between 8 % and 30 %[55,73,196]. The failure strain also differs among the hierarchical levels. This variability in results brings a lot of uncertainty in characterizing tendon. Similarly, there are contradictory results reported in the literature when comparing the mechanical properties of tendon in respect of aging. On the one hand there are studies denying a significant influence of age to healing tendon[197], but on the other hand, opposite statements are published in the same journal[198]. A similar inconsistency exists when studying the morphology of tendon, e.g. the crimp pattern.

At the fibrous level, Rigby et al. highlighted the disappearance of the crimp pattern when the tendon is stretched under polarized light[59]. Diamond et al. observed the same phenomenon when imaging the fibrous constituents of tendon. The reported crimp pattern disappearance occurred among all the age groups (from 2 weeks to 29 months), but in general, the pattern disappeared at mean strain 3.65 %[199]. Hansen et al. used optical coherence tomography to investigate the crimp pattern disappearance in the rat tail tendon fascicles. In this study, the crimp pattern started disappearing individually, from the ends towards the centre, and disappeared completely before reaching 3% strain[200]. In a recent study, Legerlotz et al. also studied the response of the crimp pattern to mechanical loading. In this case, the crimp pattern in the rat tail single fascicles already disappeared at 0% to 1% strain[60].

To supplement the results on the mechanical properties and crimp pattern with information at the molecular level, for example, the collagen triple helix, X-ray diffraction crystallography is considered to be the gold standard[10]. Unfortunately, this method does not allow one to investigate tendon *in vivo*. Recently, a complementary method of polarized second harmonic

generation (PSHG microscopy) is used for biological structures[124]. The structures, named harmonophores, which fulfil molecular requirements such as a non-zero second-order susceptibility tensor $\chi^{(2)}$, can generate the second harmonic signal at 2ω of the illumination beam. The generated signal depends on the density of the molecules (harmonophores), and the strength of the exciting electric field. In addition, the SHG signal also depends on the orientation of the polarized exciting electromagnetic field in respect of the orientation of the harmonophores. This phenomenon is utilized to calculate the mean effective harmonophore orientation angle with pixel size resolution[123,201]. The reported helical pitch angle (HPA) of the collagen molecule reaches θ = 42.7° with $\Delta\theta$ = 5.9°, where $\Delta\theta$ (FWHM) represents the level of harmonophores organization[123], $\theta \approx 49°$[110], $\theta \approx 50°$[202] or $\theta = 45.82° \pm 0.46°$[107]. These values are in good agreement with X-ray crystallography data (θ = 46.34°)[107]. The above mentioned methods provide wide-scale information on collagen which is the major structural protein in tendon. However, the collagen triple helix does not act independently in tendon, and its functional stability is moderated by micro-environment, for example, cross-linking.

Most cross-linkers, for example, tyrosine and pyridinoline (emitting at the blue spectrum) or the advanced glycation end products including pentosidine (emitting at the yellow-green)[203], are fluorescent, and their accumulation influence the fluorescence lifetime of the collagen structures. So far, this phenomenon was mainly confirmed by Lutz et al. who reported an increase of long-lifetime component τ_2 for collagen autofluorescence in the *in vitro* collagen model due to cross-linking[118].

In this chapter, uniaxial tensile test is performed on the intact tendons to identify the mechanical differences among the age groups. It is expected to reach higher failure stress for the tendons from the older animals. Furthermore, it is hypothesised that the tendons from the older animals response more rapidly to a change of strain, i.e. no “toe” or “heel” region in the stress-strain curve. To investigate the crimp pattern reaction to mechanical stress, the intact tendons are stretched and simultaneously visualized by SHG microscopy. The behaviour of the tendons is also investigated by PSHG microscopy in the load-free and stretched states. This experiment is conducted to detect a decrease in the collagen HPA due to mechanical loading. Finally, the collagen micro-environment is analysed by fluorescence lifetime imaging microscopy (FLIM) to reveal an increase in collagen cross-linking with age.

6.2 Material and methods

6.2.1 Animal studies: intact tendons

The rabbit hind limb tendons (*tendo calcaneus communis* and *tendo m. flexoris digitorum*) were investigated from New Zealand white, Czech Spot, and Belgian Hare crossbred rabbits from the age of 7 days to 38 months (n = number of tendons, see below). The animals were bred in hutches and exhibited healthy physical conditions. The legs were received as animal waste product, and tendons were carefully dissected from both left and right hind legs. The protocol was identical to that in Section 5.2.1. All the samples were placed on ice and investigated within 48 hours after the slaughter. The below specified tendons were measured by the protocols in Section 6.2.2 – 6.2.3.5.

6.2.2 Macro uniaxial tensile testing of tendons

The intact tendons of 4-month-old (n = 6) and 38-month-old (n = 4) animals were compared by using Tester Tensile Instrument coupled with a microscopic video analyser as extensometer. The Tester Tensile Instrument (TTI) setup detected tension/compression forces up to the hundreds of newtons with the sensitivity of 0.01 N. The relative position of the moving grip was monitored by an inductive position sensor. The video analyser setup consisted of the microscope SZX 12 (Olympus, Japan) connected to the high performance digital 12-bit CCD camera PCO SensiCam (Kelheim, Germany). The image was acquired through the objective DF PLFL 0.3x (1376x1040 pixels, pixel size 0.05 mm, Olympus, Japan).

The intact tendon was removed from ice and its diameter measured by a calliper for the assumed circular cross-sectional area (CSA). Then the tendon ends were sealed with adhesive tape and placed into the selected TTI grips (three grips designs available). The testing protocol consisted of ultimate tensile strength test. First, the tendon was pre-stressed but still no tensile force was detected. Second, the tendon was marked with two vertical lines for extensometry. Finally, the tendon was elongated by the rate of 2 mm/s while recording force, time, and distance between the grips. Simultaneously, a video of the tensile test was being recorded at the speed of 7.8 fps.

The signal from the tension/compression sensor (S-22, max. load 500 N, Lukas Tenzo, CR) was transformed from force to engineering stress, and the distance between the grips was recalculated to engineering strain. Furthermore, the distance between the markers was measured manually by using a freehand line tool in FIJI/ImageJ (NIH) for each image. The automatic distance evaluation was run in Matlab 2015a (Mathworks, USA). The image region, where the markers appeared during the test, was selected through the rectangular tool. Then the freehand tool was used for the markers mask. This mask was placed over the image to analyse the intensity profile at the markers. The distance between the peak values was calculated for one image. After that, the new peak intensity around the mask was selected, the mask was shifted, and the intensity profile was analysed again for the new peak values. At the end, the distance of the markers in all the images was stored in a dataset, expressed as engineering strain and plotted into the stress-strain curve.

6.2.3 Microscopy and micro mechanical testing

6.2.3.1 Microscope and light source

The experiments, except Section 6.2.3.2, were conducted on the system which consisted of a confocal scanning head (Zeiss LSM 510 META, Zeiss, Germany) mounted to the motorized inverted Axiovert 200M microscope (Zeiss, Germany) and coupled with a femtosecond tunable pulse laser (Mai Tai DeepSee, Spectra-Physics, USA).

6.2.3.2 Crimp pattern behaviour: micro uniaxial tensile test and SHG microscopy

The micro uniaxial tensile test was conducted on an instrument of the in-house construction (Fig. 6.1). The instrument fits into the most commercially available microscope stages with the opening 110 mm wide and 160 mm long. The instrument's grips are driven by a couple of stepper actuators NEMA 8, Series 21000-N and provide the maximum output force of 45 N at the maximum speed of 5.1 mm/s and step resolution 3 μm (Servo-Drive, Czech Republic). The force change is detected with two force sensors LCM201-100N (Omega, USA). Each force sensor has the accuracy ± 1 N and the data output is created as the mean value of the two force sensors. The low-friction movement is ensured by two parallel rolling guideways MGN 07 C (Hiwin s.r.o., CR). Finally, the instrument is controlled by a LabVIEW 2015

interface program (National Instruments, USA) through the Arduino Uno microcontroller (Arduino, Italy).

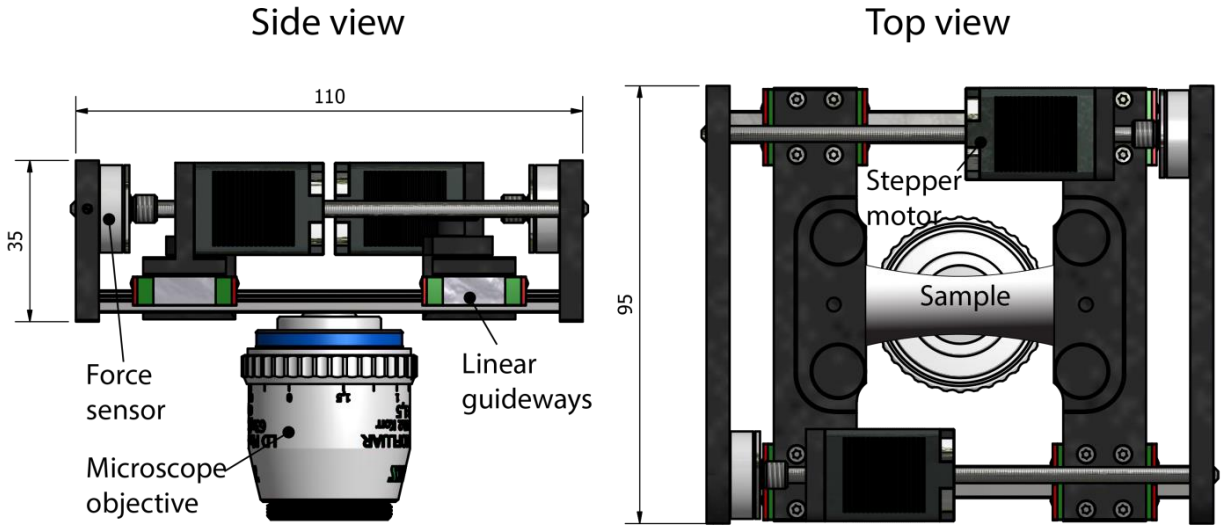

Fig. 6.1 *Micro tensile instrument. The fronts, the transversal beams, and the embedded grips of the instrument were manufactured from CERTAL® alloy (Gleich Aluminum s.r.o., CR) which offers high strength-to-density ratio, and therefore the instrument withstands high stresses at low construction weight.*

The intact Achilles tendon ends from 7-day-old (n = 7) and 38-month-old (n = 6) animals were sealed with adhesive tape and placed into the grips. Before being elongated, the tendon was imaged according to the SHG experimental protocol Section 5.2.2 – System I, but this time, the microscope was equipped with an objective (HC PL FL 10x/0.30, image resolution 1024x1024, pixel size 1.46 µm, Leica, Germany). Then the tendon was repeatedly stretched by 0.12 mm in a discontinuous manner at the speed of 0.6 mm/s. After each stretch, a new SHG image was acquired until the detected force reached positive values. After that the tendon was shorten to its original length by the reversed stretching protocol. Finally, the collagen crimp patterns were linked with the induced stresses.

6.2.3.3 Helical pitch angle measurement by PSHG microscopy

The 810 nm linearly polarized incident beam was generated in a femtosecond tunable pulse laser source (Mai Tai DeepSee, Spectra-Physics, USA). After the beam travelled through the scanning galvanometer mirrors (SGMs) and a beam splitter (BS1), it reached an in-house built automated polarization controller[194]. The controller design uses the combination of a quarter wave-plate (λ/4) and a half wave-plate (λ/2) to achieve the desired polarization angle of the incident laser beam. The rotation of the wave plates is driven by two stepper motors (Trinamic PD-110-42, Germany) that together with a transmission guarantee an angular resolution of 0.1125°. The controller receives the synchronisation TTL frame pulse from the Zeiss microscope and commands about the polarization state through the Matlab GUI interface (Mathworks, USA). The incident beam at a selected polarization state travelled through an objective (Plan-Apo 20x/0.75 dry, image resolution 2048x2048, pixel size 220 nm, Zeiss, Germany) and interacted with the sample. The light was collected behind the sample, in forward direction, by a condenser (adjustable NA up to 0.8, Zeiss, Germany), and then travelled through a band-pass filter (BP 405/10, Semrock, USA) to a multi-alkali PMT5 detector (Fig. 6.2).

The 2-D images of the tendons from 1-month-old (n = 3), 8-month-old (n = 4) and 18-month-old (n = 6) animals were acquired under 20 different polarization angles α ranging from 0 to 360 degrees with an 18-degree step. Afterwards, each pixel of the image was analysed for the HPA of the polypeptide chain of the collagen triple-helix by fitting the theoretical model[124,201]

$$I^{SHG}(\Phi,\alpha) = C^2 \sin^2[2(\Phi-\alpha)] + [A\sin^2(\Phi-\alpha) + B\cos^2(\Phi-\alpha)]^2, \qquad (6.1)$$

where Φ is the orientation angle of the helix axis, α is the incident beam polarization state with the x-axis, and $A = I_0 d_{31}$, $B = I_0 d_{33}$, $C = I_0 d_{15}$ are the free fitting parameters, where I_0 is proportional to the signal intensity, and d_{31}, d_{33}, d_{15} are the non-zero elements of the non-linear susceptibility tensor $\boldsymbol{\chi}_{ijk}^{(2)}$ (Eq. 1.3), where $\chi_{ijk}^{(2)} = 2d_{ijk}^{(2)}$. According to Amat-Roldan et al., when meeting certain conditions, it is possible to calculated the HPA θ from the parameters A and B as

$$\cos^2\theta = \frac{B}{(2A+B)}. \tag{6.2}$$

The analysis returned a HPA histogram peak value and the HPA distribution. The fitting was performed in Matlab 2015a using the *lsqcurvefit* function (Mathworks, USA).

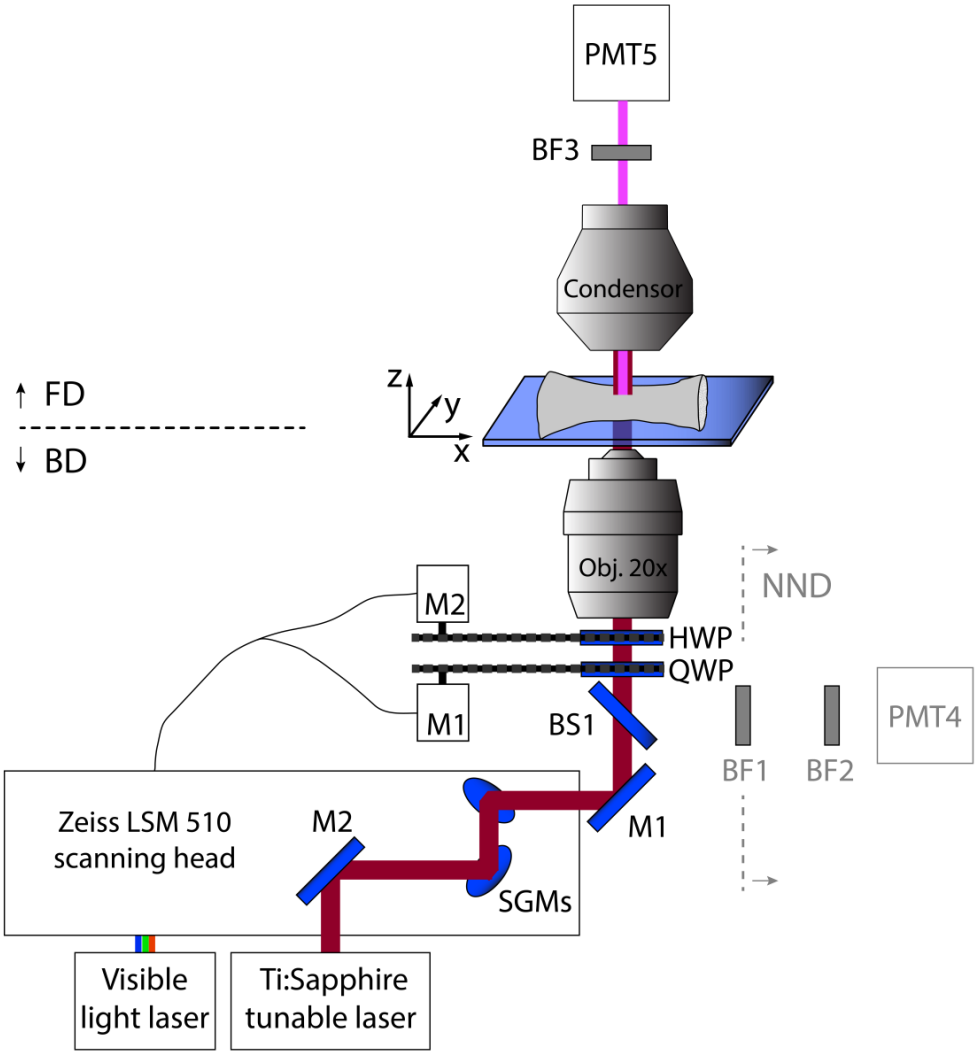

Fig. 6.2 Schematic of optical setup for PSHG microscopy. To neglect the polarization effect of the beam splitter **BS1**, the light was detected only in forward direction (**FD**). **QWP** and **HWP** represent the quarter wave-plate (λ/4) and the half wave-plate (λ/2), respectively, which are located in backward direction (**BD**). **BF3** is the band-pass filter for SHG signal detection. The other parts are identical with the Figure 2.1, Chapter 2.

6.2.3.4 Helical pitch angle dependency on mechanical loading

In this case, the tendons (*tendo m. flexoris digitorum*) from the 6-month-old (n = 6) animal were pre-stretched by the instrument in Section 6.2.3.2 until the force sensors detected positive force values. At this moment, a 2-D image was acquired to provide information about CSA, and afterwards only the line scan mode was selected together with time series acquisition (duration 100,000 s) using a 10x objective (EC Plan-Neofluar 10x/0.3, image resolution 1x512, pixel size 234 nm, Zeiss, Germany). The time series acquisition was synchronized with the polarization controller from Section 6.2.3.3, and the line scan was performed continuously. After imaging the tendon at several full rotations of the polarization controller, the tendon was stretched or released while the image acquisition continued together with the automatic change of the polarization plane. The acquired data were treated as an m-by-512 matrix, where m symbolizes the number of cycles in the time series. Then the matrix was averaged over the second dimension, and the resulted vector was plotted. Next, the manually selected regions of the plot were fitted according to the model in Section 6.2.3.3. Finally, the force change, elongation between the grips, and the HPA were presented in the graph. The experiment workflow is simplified in Figure 6.3.

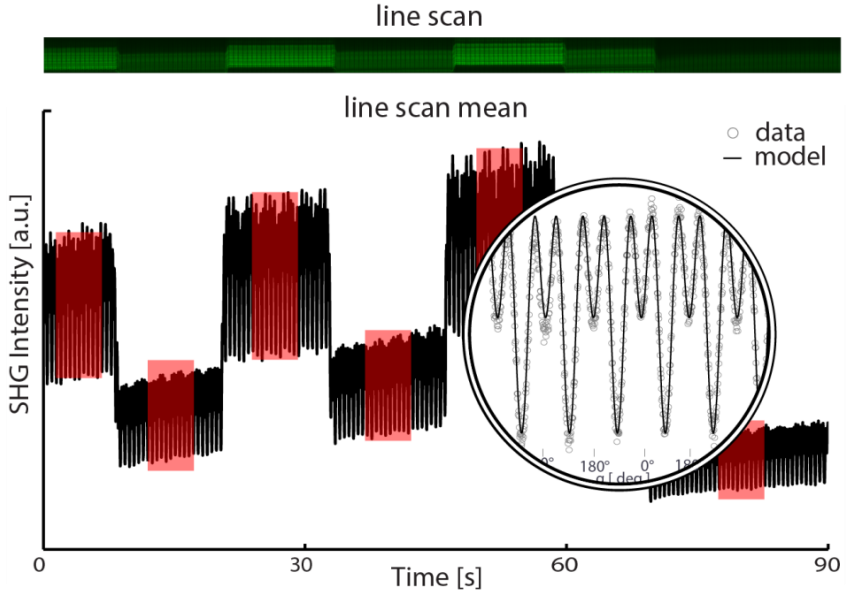

Fig. 6.3 PSHG plus micro tensile test. The green line scan ribbon represents the raw data. The mean values are plotted in the graph where each step in intensity represents a change in tension. At the end, a middle region, highlighted in red, is manually selected for the HPA analysis. The enlarged section shows the measured data, and the fitted model by Equation 6.1 and 6.2. The x-axis values α [deg.] are polarization angles relative to fibres.

6.2.3.5 Fluorescence lifetime development with age in tendon

Three different age groups (1, 6, 18 months old animals) of tendons (n = 3 for each group) were analysed for time-domain fluorescence lifetime imaging microscopy (FLIM). The experiment was conducted at the above mentioned microscope (Zeiss LSM 510 META coupled with Zeiss Axiovert 200M, Zeiss, Germany) when the tendons were excited at 810 nm by a tunable pulsed laser (Mai Tai Deep See, Spectra-Physics, USA) using the Plan-Apo 20x/0.75 dry objective (Zeiss, Germany). The incident beam was horizontally polarized along with the long axis of the tendon, i.e. x-axis of the optical system (Fig. 6.2). The emitted light was collected in backward direction and separated from the excitation light using a filter cube containing the 735 nm short pass filter, the dichroic beam splitter at FT442 (Zeiss, Germany) followed by the BP 405/10 band pass filter (Semrock, USA) for SHG image acquisition at a multi-alkali PMT4 detector or by the BP 550/200 band pass filter for collagen autofluorescence lifetime image acquisition by a GaAsP detector (H7429-40, Hamamatsu, Japan). The GaAsP detector was connected to the Becker & Hickl SPC830 card (Becker & Hickl GmbH, Germany) that allows time-correlated single photon counting. The obtained images with a resolution of 256 time channels and 128 by 128 pixels, a pixel size of 220 nm, and a pixel dwell time of 6.4 µs were accumulated for 20 s. This collection time ensured a sufficient number of photons (> 8,000) per pixel for the analysis. The analysis of the fluorescence lifetime decay curves was performed in SPCImage 5.6 (Becker & Hickl, Germany) by fitting the collected photons with the double-exponential model[129]

$$f(t) = a_1 e^{-\frac{t}{\tau_1}} + a_2 e^{-\frac{t}{\tau_2}}, \quad (6.3)$$

where τ are the lifetimes of the exponential components, and a are the amplitudes of the exponential components. The long-lifetime component τ_2 is forwarded for the statistical analysis as there is more pronounced the change in collagen autofluorescence[204]. The instrument response function was measured by generating the SHG signal in KDP crystal at the excitation wavelength of 810 nm. The accepted models reached the goodness of fit chi-square χ^2 value lower than 1.25.

6.2.4 Statistical analysis

The data were always checked for normality (S-W test, Q-Q plot) and after that tested by the Mann–Whitney U test/Independent sample t-test or Kruskal-Wallis /One-way ANOVA followed by a post-hoc test (Dunn and Sidak, Tukey's HSD respectively)[182]. If not stated otherwise, the results are published as means with sample standard deviations. The significant value for rejecting the null hypothesis was set to p-value < 0.05. The data analysis was performed in Matlab 2015a (Mathworks, USA) and ImageJ (NIH, USA). The statistical evaluations were performed by using Matlab 2015a.

6.3 Results

6.3.1 From macro to micro mechanical testing

The standard uniaxial tensile test was performed on the intact tendons. For the 4-month-old animals, the maximum reached stress was 100.0 ± 47.2 MPa (mean ± SD) at strain 2.9 ± 3.1 %. The ratio between the extensometry vs. calliper based CSAs was 1.77 ± 0.80. For the 38-month-old animals, the maximum reached stress was 127.8 ± 84.2 MPa (mean ± SD) at strain 5.9 ± 5.7 %, and the ratio was 1.80 ± 0.80. The deformation was based on the distance between the extensometry markers acquired manually. This value frequently differed from the strain calculated at the grips position or by the automatic detection method. For example, Figure 6.4 demonstrates one of the best results during the Achilles tendon tensile test, but even in this test the stress values dropped with additional deformation. The statistical comparison of the groups returned no significant difference between the maximum stresses (p-value = 0.66) and the relevant strains (p-value = 0.35). Therefore, the intact tendons behaviour was observed by combining the uniaxial tensile test and SHG microscopy.

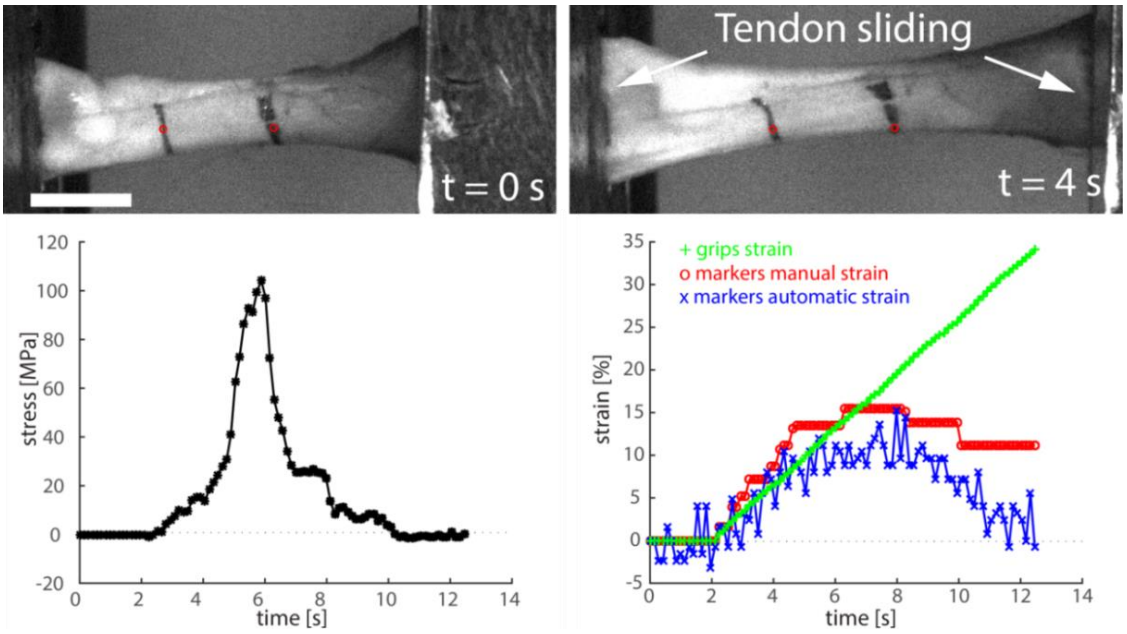

Fig. 6.4 Macro uniaxial tensile test: 4-month-old animal. (**top**) The tendon was sliding from the grips when performing the tensile test. The dark lines served as the markers for extensometry, and the red circles symbolize the spots detected by the automatic detection method. Scale bars = 5 mm. (**bottom left**) The engineering stress had a discontinuous character. (**bottom right**) The three methods used to detect the tendon elongation.

In the load-free state, the appearance of the crimp pattern was consistent with the results in Chapter 5. When the tendons from the young animals were stretched, the crimp pattern disappeared and reappeared immediately after returning to the initial elongation, i.e. the load-free state (Fig. 6.5). On the other hand, the crimp pattern was barely detectable in the tendons from the old animals and did not rearrange under mechanical load.

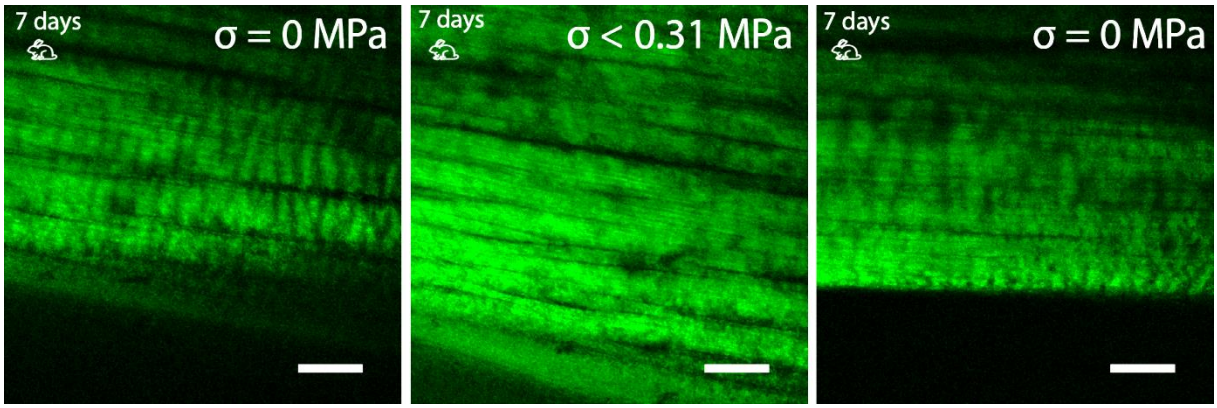

Fig. 6.5 Micro uniaxial tensile test with SHG microscopy. The crimp pattern in the 7-day-old rabbit tendon disappeared before reaching minimum resolution of the force sensors. Scale bars = 100 µm.

6.3.2 Helical pitch angle at load-free and stretched state

The PSHG microscopy at the load-free state revealed no significant difference in the HPA among the age groups, although there was a trend towards an increase of the HPA with age (Fig. 6.6).

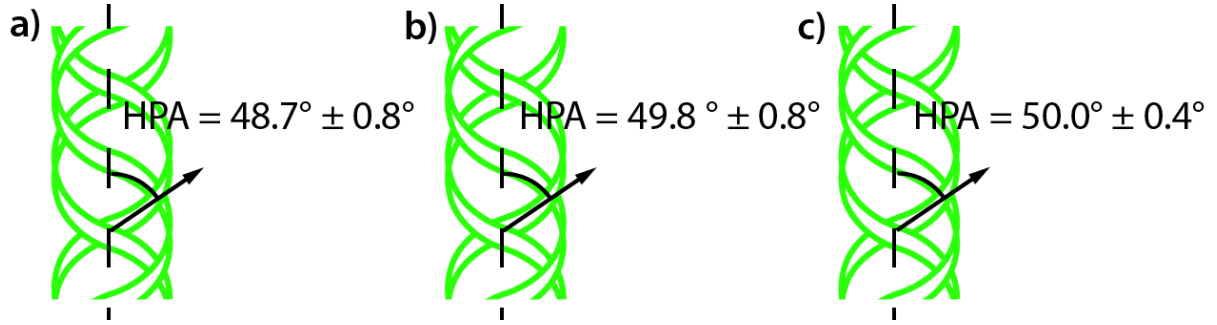

Fig. 6.6 HPA of collagen molecule in flexor. (**a**) 1-month-old animals (n = 3). (**b**) 6-month-old animals (n = 4). (**c**) 18-month-old animals (n = 6). The HPAs are stated as mean ± SD.

The response of the HPA to mechanical load was analysed with respect to a force/elongation change. There was not found a significant difference within the samples between the states of higher and lower stress (Fig 6.7). All the measurements are summarized in Figure 6.8.

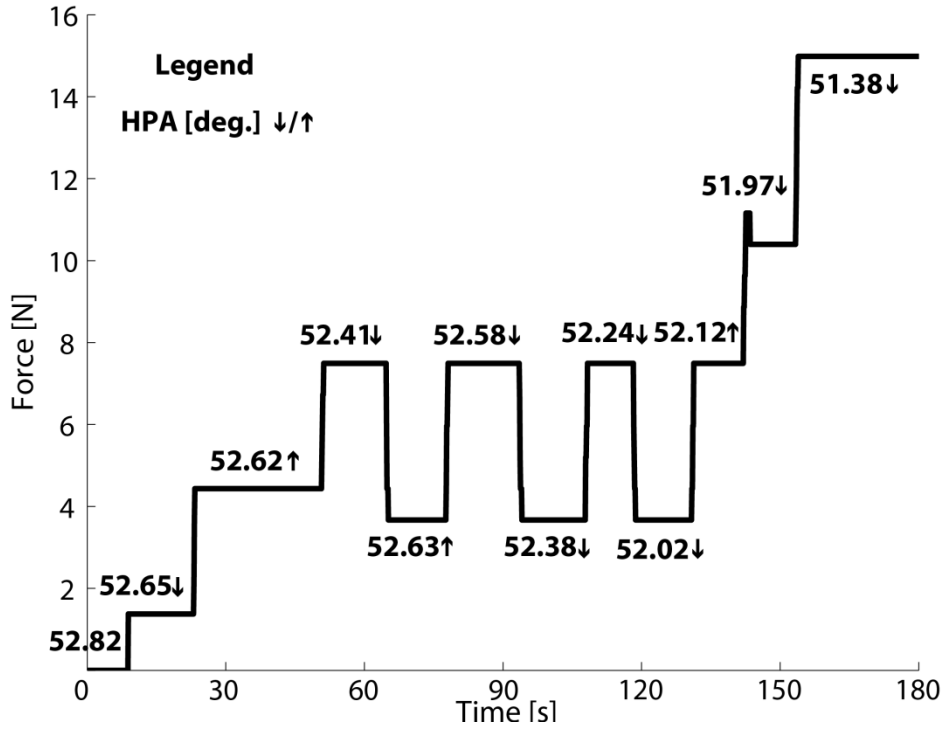

Fig. 6.7 HPA response to mechanical loading of single tendon. The arrow ↑ up or ↓ down symbolizes an increase or decrease of the HPA with respect to the previous state for the 6-month-old animal.

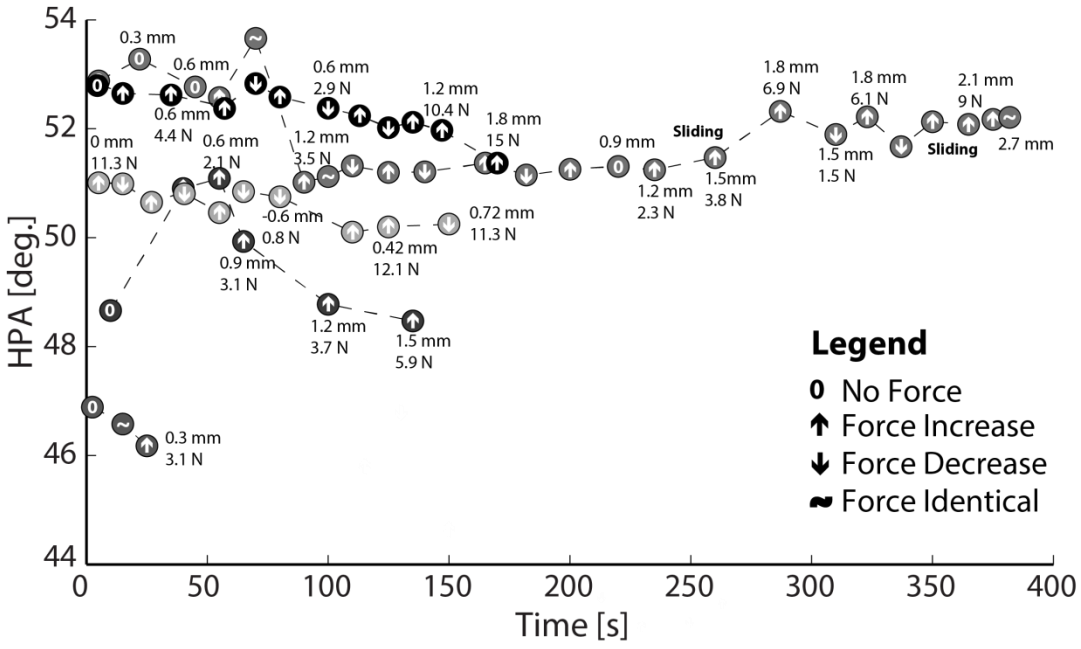

Fig. 6.8 Summary of HPA response to mechanical loading. With force increase (↑), the HPA is expected to decrease and vice versa. Each tendon sample is represented by a different shade of grey.

6.3.3 Fluorescence lifetime of tendons from young and old animals

A similar tendency as for the HPA increase in the load-free state was detectable when comparing the lifetime component τ_2. The component increased with age, and a significant difference was found between 1-month-old animals (2747 ± 73 ps; mean ± SD) and 6-month-old (3102 ± 98 ps), 18-month-old (3056 ± 28 ps) animals. The SHG images of the same region were also acquired together with the lifetime images (Fig. 6.9). In the tendons from all the age groups, collagen generated strong SHG signal and the fibres possessed usual appearance with the crimp pattern.

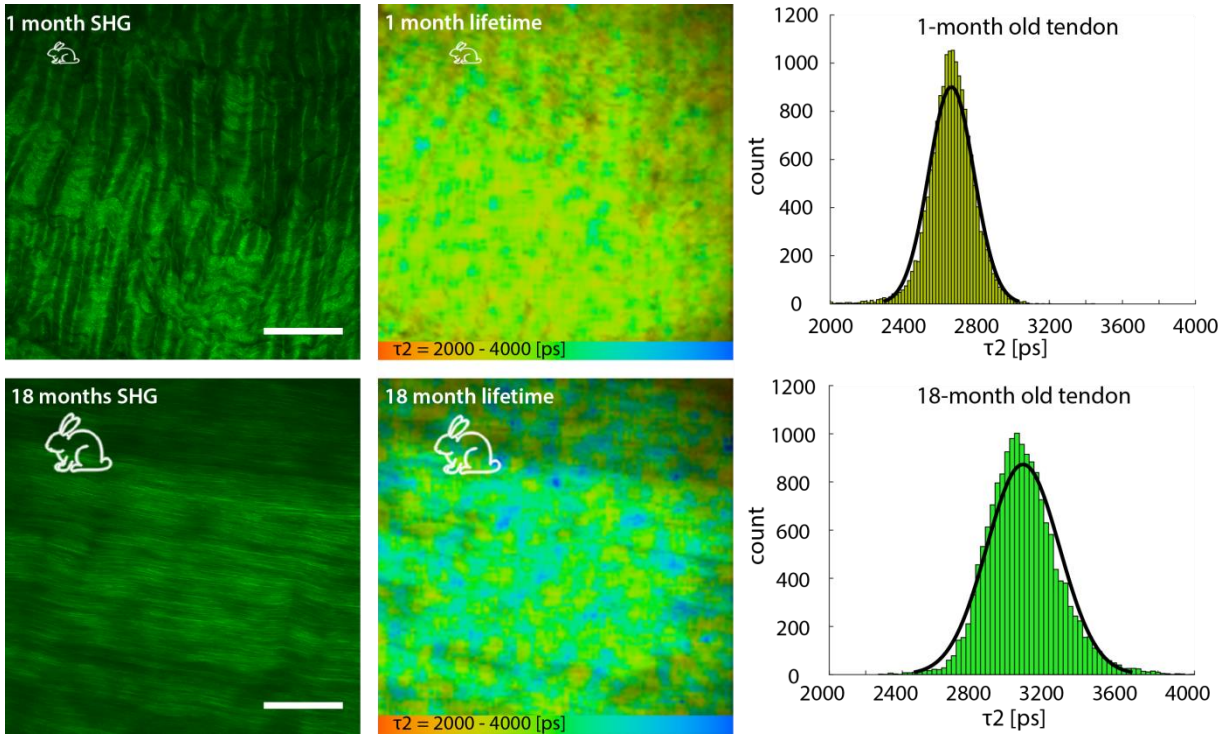

Fig. 6.9 Lifetime imaging and SHG comparison of tendons. The SHG images provided information on tendons morphology and collagen molecular quality. The lifetime images revealed the quality of the tissue micro-environment.

6.4 Discussion and conclusion

During the macro uniaxial tensile test, the maximum stresses varied form tens to hundreds of MPa. Similar values are reported in literature as stated in Section 6.1. Although the stress values were often above the published failure level, the tendon never seemed to reach yield stress and rather started sliding. The results also had high variability which was reflected in the statistical tests. The main cause of such a spread in the data could be the tendon-grip interface, extensometry, and CSA identification. The tendon-grip interface is a well-recognized disadvantage when testing soft tissue. It causes tissue slippage and stress concentration[205]. This problem can be partly avoided by using special design of the grips[206] or cryo-grips[71]. However, this solution is challenging to apply to small samples. Another grip disadvantage is the tendon placement. According to the image data from extensometry, the tendon ends in the grips were sometimes angularly rotated, and therefore subjected not only to uniaxial tension but also to torsion. Moreover, the grip-to-grip deformation did not match deformation in the middle region of the tendons. Haraldsson et al., for example, reported about 50% higher values for the grip-to-grip deformation[205]. Finally, the CSA measured by a calliper differed from the extensometry images. According to the data, this geometrical difference can be caused by flatting the tendons at the grips. Except these major factors, the results can be also influenced by testing environment[207]. To partly overcome these difficulties and investigate the response of the collagen structures in tendon to mechanical loading, the uniaxial tensile test was conducted simultaneously with SHG microscopy.

The load-free tendons from the young animals had a clear crimp pattern which disappeared at minimum resolution of the force sensors. The crimp pattern disappearance is usually ascribed to the non-linear region of the stress-strain curve, which participates greatly in the physiological loading (Chapter 1)[200]. The stress at the end of this non-linear region is usually at ones of MPa. According to the *in vivo* measurement on patellar tendon, the force never reaches zero or negative values for all the stages of hopping or standing[208]. Therefore, the significance of the crimp pattern as a mechanical buffer[209] is questionable. More likely, the crimp pattern has a preload function which fractions the amount of initial loading force from muscles. This ability could be lost as the crimp pattern disappears with age, and therefore

there is the highest occurrence of non-sport related Achilles tendon ruptures at the mean age of 53 years[210].

It was also hypothesised that age affects the HPA of the collagen molecule. The results provide no evidence to reject the null hypothesis. However, it seemed that there is a trend towards the HPA increase with age. According to the spread in the data, the susceptibility model needs to be improved, and more tendons need to be measured by PSHG microscopy. Similar results were obtained when the HPA of the collagen molecule was measured under mechanical load. In this case, the results were additionally influenced by the length of the experiment. Some of the experiments lasted minutes and drying could play a significant role.

Finally, FLIM was adopted to investigate the micro-environment of the tendons. It was revealed that the long-lifetime component τ_2 significantly increased with age when measured the autofluorescence signal. Lutz et al. reported lifetime of 2800 ps for the untreated control model *in vitro*. Almost identical lifetime was reach for the tendon from 1-month-old animals. When Lutz et al. measured lifetime of the model with increased collagen cross-linking, the obtained lifetime was 3052 ps. This value is again very close to the lifetimes of 6-month and 18-month-old tendons. Unfortunately, lifetime values are not specific and reflect the complex micro-environment including pH, viscosity, temperature, or metabolic activity[203]. Therefore, a more robust experimental design is necessary to verify the stability of the experiment and to include some additional techniques for the identification of collagen cross-linkers.

This chapter highlighted the possible causes of bias in mechanical testing of biological tissue and related low reproducibility among studies. The results on the crimp pattern confirmed the conclusion in Chapter 5. In addition, PSHG microscopy provided important data on the HPA of collagen molecule. It is necessary to state that PSHG microscopy is a powerful tool not only when judging on the HPA, but also when discriminating between type I and type II collagen[106]. The last part of this chapter uses the phenomenon of excited state decay, to quantify the parameters of micro-environment. However, this method is very prone to misinterpretation because the lifetime decay is influence by multiple variables.

6.5 Acknowledgement

The PSHG microscopy was conducted in cooperation with Dr. Rik Paesen, UHasselt .

Chapter 7

7 General conclusion

7.1 Summary

This study grasps the complexity of connective tissue and its major component type I collagen. The extended introduction offers the historical overview on collagen investigation. It summarizes the experimental insights into the triple helix organisation thanks to the invention of X-ray crystallography. The following sections target the collagen synthesis and formation of collagen in the extracellular matrix. The different types of collagen are introduced in respect of function and location. A short section is also devoted to collagen tissue aging due to cross-linking. The introduction is concluded with the sections on mechanical properties of tendon and common methods used for visualisation of connective tissue, especially the non-linear methods such as second harmonic generation (SHG).

At the beginning, the *in vitro* model was constructed to measure the production of type I collagen and visualise collagen fibres. The aim was to label only the selected extracellular proteins and to preserve morphology of the cell culture. As immunostaining (IS) offers a wide pallet of labelling protocols[150,211], several modifications were implemented to meet this target. The modifications included placement of the cell culture on ice while applying the primary antibody and fixation of the cell culture after applying the primary antibody and washing. When comparing the cell culture with and without ascorbic acid (AA) treatment, the results showed higher cell growth and collagen deposition in culture with AA treatment, but no significant difference was found between expression levels of type I collagen gene. Besides, the cell culture was studied by label-free SHG microscopy. This measurement experimentally proved that the absence of AA in the cell culture, which directly affects the hydroxylation of proline, results in the loss of SHG signal. This validates the second-order susceptibility tensor model[107], in which hydroxyproline plays a crucial role while generating the second harmonic signal. As the presence of the SHG signal depends on the inner structure, it offers not only a quantitative but also qualitative tool for type I collagen investigation. This is the main advantage of non-linear SHG microscopy over the classic IS methods when revealing

pathological conditions[146] because IS scoring is often based on subjective expertise and returns results with high variability[212]. The advantages of SHG microscopy were even more pronounced when examining microtome section of tendon. The samples did not have to undergo multiple preparation steps[160,213] that affect morphology[135] and could be optically sectioned into 3-D label-free reconstruction. Thanks to the near infrared laser source, SHG microscopy also reduces scattering, photodamage and increases penetration depth of observation. The observation can be also directly enriched for the information about the orientation of collagen fibres. This approach relies on the fact that the SHG signal depends on the molecular orientation and incident beam polarization, respectively[123]. But sometimes, the sample cannot be scanned under different polarization angles, and therefore the fibre orientation must be retrieve from a single image. For that reason, the algorithm was developed to quantitatively determine the orientation regularity of collagen fibres. The results showed that there is a significant difference in the orientation regularity of fibres between the microtome sections of the tendons from the young and old animals. The microtome sections from the young animals possessed high isotropy of fibres. On the other hand, the microtome sections from the old animals contained anisotropic fibres. The experiment on the intact tendons followed to investigate whether the differences of the orientation regularity had been caused by sectioning or by senescence. In this case, the load-free intact tendons had strong orientation regularity of the fibers within the main load-bearing axis. This fibrillar regularity was represented by periodically undulating pattern – the crimp pattern. This pattern developed with age until it almost disappeared in the tendons from the old animals. The comparison of the results proved that the microtome sectioning modified the morphology of tendons, especially in the tendons from young animals.

Although there is not a generally accepted explanation for the cause and purpose of the crimp pattern, it is supposed that it reflects both the inner physiological and morphological status and provides an optimum mechanical response. The intact tendons were mechanically tested by the uniaxial tensile test but the data had high variability, and therefore, it was impossible to decide on the significance of the crimp pattern from the mechanical point of view. This problem was mainly caused by the tendon-grip interface, extensometry, and identification of the tendon geometry. For this reason, the tendon was stretched and

simultaneously imaged by SHG microscopy. It was discovered that the crimp pattern had disappeared before reaching minimum resolution of the force sensors and reappeared immediately after returning to the initial elongation. This behaviour indicated a preload function of the crimp pattern which would lead to a lower increment of stress when activating muscles. After conducting the mechanical test with SHG microscopy, the visualization method was upgraded to polarized SHG (PSHG) microscopy. As the result, the helical pitch angle (HPA) of collagen molecule was detected for the intact tendons from animals of different age at the load-free state. This pixel resolution approach showed no change in the HPA in respect to age or mechanical loading. This finding supports the theoretical framework about the mechanical properties and stability of collagen molecule. On the other hand, fluorescence lifetime microscopy revealed significant changes in the micro-environment of tendon. These changes in fluorescence lifetime were probably caused by collagen cross-linkers which act as a reinforcement component that directly affect the mechanical properties of tendon.

7.2 Future perspectives

Although collagen has been studied for more than hundred years, complex understanding of interactions is still absent. The *in vitro* models are usually constructed in static conditions, and therefore the cell-extracellular matrix communication is relatively limited in such models. From the biomechanical point of view, the cell-extracellular matrix interactions play a crucial role in signalling and remodelling, hence the dynamic model is required. Thanks to the label-free imaging methods, different parameters of the dynamic model can be observed directly and correlated with conventional techniques. The conventional techniques can be also augmented with 3D super-resolution microscopy. This new approach can provide resolution of tens of nanometres with high structural specificity. The mechanical properties of biological structures in such models are usually difficult to determine, however, the increasing popularity of atomic force microscopy (AFM), miniature electronics and increasing computational power will optimize this concept for mechanical testing of *in vitro* models.

Even more challenging task is to detect biological structures in bulk dense tissue or safely *in vivo*. The density of tissue usually prevents an antibody or even radiation to interact with the sample. In the microtome sections, this problem can be overcome by clearing protocols.

Unfortunately, these protocols usually involve multiple-step sample preparation which can influence morphology and cannot be utilized for *in vivo* measurements. A possible solution for this problem can be miniature endoscopic microscopy or even autonomous nanoscopic probes. In a similar way, the measurement of mechanical properties on microtome sections or *in vivo* could be conducted. Overall, the measuring instrument could contain biochemical, morphological and mechanical laboratory-on-a-chip which will be placed into the location of interest. Unfortunately, these approaches are still beyond the current technological limits, and therefore the main focus is on developing and improving the techniques from Chapter 6.

The developed protocols of SHG, PSHG, fluorescence lifetime (FLIM), and two-photon excitation fluorescence microscopy (TPEM) together with mechanical testing are currently used to assign transformations of the individual components of connective tissue to specific treatment or disease. The ongoing projects are targeting the investigation on decellularized porcine vessels or idiopathic *pes equinovarus* (clubfoot). The decellularized porcine vessels are used as grafts for tissue engineering. The native and differently decellularized vessels are compared for mechanical and morphological properties including label-free investigation on different types of collagen and elastic fibres. In contrast, clubfoot is a congenital deformity of foot and possible pathologic mechanisms of its formation are searched by the correlation of label-free visualisation, biomechanical testing, cell type identification and *in vitro* dynamic model construction, and mass spectrometry.

Chapter 8

8 References

8.1 Reference list

1. **Y. C. Fung**, *Biomechanics: Mechanical Properties of Living Tissues*, Springer New York (2013).
2. **B. Brodsky, J. A. Werkmeister, and J. A. M. Ramshaw**, "Collagens and Gelatins," in *Biopolymers Online*, Wiley-VCH Verlag GmbH & Co. KGaA (2005).
3. **E. J. Kucharz**, *The Collagens: Biochemistry and Pathophysiology*, Springer Berlin Heidelberg (1992).
4. **A. Authier**, *Early Days of X-ray Crystallography*, OUP Oxford, Oxford (2013).
5. **L. Pauling, and R. B. Corey**, "The Structure of Fibrous Proteins of the Collagen-Gelatin Group," *Proceedings of the National Academy of Sciences of the United States of America* **37**(5), 272-281 (1951).
6. **M. D. Shoulders, and R. T. Raines**, "Collagen structure and stability," *Annu Rev Biochem* **78**, 929-958 (2009).
7. **A. Bhattacharjee, and M. Bansal**, "Collagen Structure: The Madras Triple Helix and the Current Scenario," *IUBMB Life* **57**(3), 161-172 (2005).
8. **A. Rich, and F. H. C. Crick**, "The Structure of Collagen," *Nature* **176**(4489), 915-916 (1955).
9. **A. D. Paepe, and F. Malfait**, "Bleeding and bruising in patients with Ehlers–Danlos syndrome and other collagen vascular disorders," *British Journal of Haematology* **127**(5), 491-500 (2004).
10. **A. Gautieri, S. Vesentini, A. Redaelli, and M. J. Buehler**, "Hierarchical Structure and Nanomechanics of Collagen Microfibrils from the Atomistic Scale Up," *Nano Letters* **11**(2), 757-766 (2011).
11. **F. H. Silver, J. W. Freeman, and G. P. Seehra**, "Collagen self-assembly and the development of tendon mechanical properties," *Journal of Biomechanics* **36**(10), 1529-1553 (2003).

12. **X. Cheng, U. A. Gurkan, C. J. Dehen, M. P. Tate, H. W. Hillhouse, G. J. Simpson, and O. Akkus**, "An electrochemical fabrication process for the assembly of anisotropically oriented collagen bundles," *Biomaterials* **29**(22), 3278-3288 (2008).
13. **D. L. Christiansen, E. K. Huang, and F. H. Silver**, "Assembly of type I collagen: fusion of fibril subunits and the influence of fibril diameter on mechanical properties," *Matrix Biology* **19**(5), 409-420 (2000).
14. **A. Aparecida de Aro, C. Vidal Bde, and E. R. Pimentel**, "Biochemical and anisotropical properties of tendons," *Micron* **43**(2-3), 205-214 (2012).
15. **C. Couppé, P. Hansen, M. Kongsgaard, V. Kovanen, C. Suetta, P. Aagaard, M. Kjær, and S. P. Magnusson**, "Mechanical properties and collagen cross-linking of the patellar tendon in old and young men," *Journal of Applied Physiology* **107**(3), 880-886 (2009).
16. **C. H. Kong, X. Y. Lin, C. C. Woo, H. C. Wong, C. N. Lee, A. M. Richards, and V. A. Sorokin**, "Characteristics of aortic wall extracellular matrix in patients with acute myocardial infarction: tissue microarray detection of collagen I, collagen III and elastin levels," *Interact Cardiovasc Thorac Surg* **16**(1), 11-15 (2013).
17. **Y. Li, G. Fessel, M. Georgiadis, and J. G. Snedeker**, "Advanced glycation end-products diminish tendon collagen fiber sliding," *Matrix Biol* **32**(3-4), 169-177 (2013).
18. **J. E. Marturano, J. F. Xylas, G. V. Sridharan, I. Georgakoudi, and C. K. Kuo**, "Lysyl oxidase-mediated collagen crosslinks may be assessed as markers of functional properties of tendon tissue formation," *Acta Biomater* **10**(3), 1370-1379 (2014).
19. **J. Myllyharju, and K. I. Kivirikko**, "Collagens, modifying enzymes and their mutations in humans, flies and worms," *Trends Genet* **20**(1), 33-43 (2004).
20. **B. Buckingham, and K. M. Reiser**, "Relationship between the content of lysyl oxidase-dependent cross-links in skin collagen, nonenzymatic glycosylation, and long-term complications in type I diabetes mellitus," *J Clin Invest* **86**(4), 1046-1054 (1990).
21. **K. Gelse, E. Poschl, and T. Aigner**, "Collagens--structure, function, and biosynthesis," *Adv Drug Deliv Rev* **55**(12), 1531-1546 (2003).

22. **R. Cicchi, N. Vogler, D. Kapsokalyvas, B. Dietzek, J. Popp, and F. S. Pavone**, "From molecular structure to tissue architecture: collagen organization probed by SHG microscopy," *Journal of Biophotonics* **6**(2), 129-142 (2013).
23. **J. P. Bilezikian, L. G. Raisz, and G. A. Rodan**, *Principles of Bone Biology, Two-Volume Set*, Elsevier Science (2002).
24. **F. S. van Dijk, P. H. Byers, R. Dalgleish, F. Malfait, A. Maugeri, M. Rohrbach, S. Symoens, E. A. Sistermans, and G. Pals**, "EMQN best practice guidelines for the laboratory diagnosis of osteogenesis imperfecta," *Eur J Hum Genet* **20**(1), 11-19 (2012).
25. **M. KJÆR**, "Role of Extracellular Matrix in Adaptation of Tendon and Skeletal Muscle to Mechanical Loading," *Physiological Reviews* **84**(2), 649-698 (2004).
26. **S. R. Lamande, and J. F. Bateman**, "Procollagen folding and assembly: The role of endoplasmic reticulum enzymes and molecular chaperones," *Seminars in Cell & Developmental Biology* **10**(5), 455-464 (1999).
27. **T. Starborg, N. S. Kalson, Y. Lu, A. Mironov, T. F. Cootes, D. F. Holmes, and K. E. Kadler**, "Using transmission electron microscopy and 3View to determine collagen fibril size and three-dimensional organization," *Nat Protoc* **8**(7), 1433-1448 (2013).
28. **D. J. S. Hulmes**, "Collagen Diversity, Synthesis and Assembly," in *Collagen* P. Fratzl, Ed., pp. 15-47, Springer US, New York (2008).
29. **N. C. Avery, and A. J. Bailey**, "Enzymic and non-enzymic cross-linking mechanisms in relation to turnover of collagen: relevance to aging and exercise," *Scandinavian Journal of Medicine & Science in Sports* **15**(4), 231-240 (2005).
30. **S. Kyle, A. Aggeli, E. Ingham, and M. J. McPherson**, "Production of self-assembling biomaterials for tissue engineering," *Trends in Biotechnology* **27**(7), 423-433 (2009).
31. **L. Bozec, G. van der Heijden, and M. Horton**, "Collagen fibrils: nanoscale ropes," *Biophys J* **92**(1), 70-75 (2007).
32. **V. Ottani, D. Martini, M. Franchi, A. Ruggeri, and M. Raspanti**, "Hierarchical structures in fibrillar collagens," *Micron* **33**(7–8), 587-596 (2002).

33. **K. Okuyama**, "Revisiting the Molecular Structure of Collagen," *Connective Tissue Research* **49**(5), 299-310 (2008).

34. **A. J. Bailey, T. J. Sims, E. N. Ebbesen, J. P. Mansell, J. S. Thomsen, and L. Mosekilde**, "Age-Related Changes in the Biochemical Properties of Human Cancellous Bone Collagen: Relationship to Bone Strength," *Calcified Tissue International* **65**(3), 203-210 (1999).

35. **M. van der Rest, and R. Garrone**, "Collagen family of proteins," *The FASEB Journal* **5**(13), 2814-2823 (1991).

36. **M. M. H. Marijianowski, P. Teeling, J. Mann, and A. E. Becker**, "Dilated cardiomyopathy is associated with an increase in the type I/type III collagen ratio: A quantitative assessment," *Journal of the American College of Cardiology* **25**(6), 1263-1272 (1995).

37. **T. Wang, Q. Gu, J. Zhao, J. Mei, M. Shao, Y. Pan, J. Zhang, H. Wu, Z. Zhang, and F. Liu**, "Calcium alginate enhances wound healing by up-regulating the ratio of collagen types I/III in diabetic rats," *International Journal of Clinical and Experimental Pathology* **8**(6), 6636-6645 (2015).

38. **G. A. Holzapfel**, "Collagen in Arterial Walls: Biomechanical Aspects," in *Collagen* P. Fratzl, Ed., pp. 285-324, Springer US (2008).

39. **J. L. Lauer-Fields, D. Juska, and G. B. Fields**, "Matrix metalloproteinases and collagen catabolism," *Biopolymers* **66**(1), 19-32 (2002).

40. **R. B. Svensson, H. Mulder, V. Kovanen, and S. P. Magnusson**, "Fracture mechanics of collagen fibrils: influence of natural cross-links," *Biophys J* **104**(11), 2476-2484 (2013).

41. **A. Goldin, J. A. Beckman, A. M. Schmidt, and M. A. Creager**, "Advanced Glycation End Products: Sparking the Development of Diabetic Vascular Injury," *Circulation* **114**(6), 597-605 (2006).

42. **J. M. Haus, J. A. Carrithers, S. W. Trappe, and T. A. Trappe**, "Collagen, cross-linking, and advanced glycation end products in aging human skeletal muscle," *J Appl Physiol* **103**(6), 2068-2076 (2007).

43. **M. Saito, and K. Marumo**, "Collagen cross-links as a determinant of bone quality: a possible explanation for bone fragility in aging, osteoporosis, and diabetes mellitus," *Osteoporosis International* **21**(2), 195-214 (2010).

44. **M. J. Buehler**, "Nanomechanics of collagen fibrils under varying cross-link densities: atomistic and continuum studies," *J Mech Behav Biomed Mater* **1**(1), 59-67 (2008).

45. **K. M. Reiser, M. A. Amigable, and J. A. Last**, "Nonenzymatic glycation of type I collagen. The effects of aging on preferential glycation sites," *J Biol Chem* **267**(34), 24207-24216 (1992).

46. **G. Fessel, C. Gerber, and J. G. Snedeker**, "Potential of collagen cross-linking therapies to mediate tendon mechanical properties," *Journal of Shoulder and Elbow Surgery* **21**(2), 209-217 (2012).

47. **S. P. Veres, J. M. Harrison, and J. M. Lee**, "Cross-link stabilization does not affect the response of collagen molecules, fibrils, or tendons to tensile overload," *J Orthop Res* **31**(12), 1907-1913 (2013).

48. **T. Goldberg, W. Cai, M. Peppa, V. Dardaine, B. S. Baliga, J. Uribarri, and H. Vlassara**, "Advanced glycoxidation end products in commonly consumed foods," *J Am Diet Assoc* **104**(8), 1287-1291 (2004).

49. **K. M. Reiser, S. M. Hennessy, and J. A. Last**, "Analysis of age-associated changes in collagen crosslinking in the skin and lung in monkeys and rats," *Biochim Biophys Acta* **926**(3), 339-348 (1987).

50. **P. Zioupos, J. Currey, and A. Hamer**, "The role of collagen in the declining mechanical properties of aging human cortical bone," *Journal of biomedical materials research* **45**(2), 108-116 (1999).

51. **M. Saito, and K. Marumo**, "Effects of Collagen Crosslinking on Bone Material Properties in Health and Disease," *Calcified Tissue International* **97**(3), 242-261 (2015).

52. **R. Singh, A. Barden, T. Mori, and L. Beilin**, "Advanced glycation end-products: a review," *Diabetologia* **44**(2), 129-146 (2001).

53. **M. Kjær, and S. P. Magnusson**, "Mechanical Adaptation and Tissue Remodeling," in *Collagen* P. Fratzl, Ed., pp. 249-267, Springer US (2008).

54. **J. H. C. Wang, Q. Guo, and B. Li**, "Tendon Biomechanics and Mechanobiology—A Minireview of Basic Concepts and Recent Advancements," *Journal of Hand Therapy* **25**(2), 133-141 (2012).

55. **J. H. C. Wang**, "Mechanobiology of tendon," *Journal of Biomechanics* **39**(9), 1563-1582 (2006).

56. **M. Franchi, A. Trire, M. Quaranta, E. Orsini, and V. Ottani**, "Collagen structure of tendon relates to function," *ScientificWorldJournal* **7**, 404-420 (2007).

57. **D. Docheva, S. A. Muller, M. Majewski, and C. H. Evans**, "Biologics for tendon repair," *Adv Drug Deliv Rev* **84**, 222-239 (2015).

58. **P. Kannus**, "Structure of the tendon connective tissue," *Scandinavian Journal of Medicine & Science in Sports* **10**(6), 312-320 (2000).

59. **B. J. Rigby, N. Hirai, J. D. Spikes, and H. Eyring**, "The Mechanical Properties of Rat Tail Tendon," *J Gen Physiol* **43**(2), 265-283 (1959).

60. **K. Legerlotz, J. Dorn, J. Richter, M. Rausch, and O. Leupin**, "Age-dependent regulation of tendon crimp structure, cell length and gap width with strain," *Acta Biomater* **10**(10), 4447-4455 (2014).

61. **S. J. Kew, J. H. Gwynne, D. Enea, M. Abu-Rub, A. Pandit, D. Zeugolis, R. A. Brooks, N. Rushton, S. M. Best, and R. E. Cameron**, "Regeneration and repair of tendon and ligament tissue using collagen fibre biomaterials," *Acta Biomater* **7**(9), 3237-3247 (2011).

62. **M. Raspanti, M. Reguzzoni, M. Protasoni, and T. Congiu**, "Mineralization-related modifications in the calcifying tendons of turkey (Meleagris gallopavo)," *Micron* **71**, 46-50 (2015).

63. **G. Riley**, "The pathogenesis of tendinopathy. A molecular perspective," *Rheumatology* **43**(2), 131-142 (2004).

64. **F. S. Chuen, C. Y. Chuk, W. Y. Ping, W. W. Nar, H. L. Kim, and C. K. Ming**, "Immunohistochemical characterization of cells in adult human patellar tendons," *J Histochem Cytochem* **52**(9), 1151-1157 (2004).

65. **J. Kondratko-Mittnacht, S. Duenwald-Kuehl, R. Lakes, and R. Vanderby Jr**, "Shear load transfer in high and low stress tendons," *Journal of the Mechanical Behavior of Biomedical Materials* **45**, 109-120 (2015).

66. **K. Legerlotz, G. P. Riley, and H. R. C. Screen**, "GAG depletion increases the stress-relaxation response of tendon fascicles, but does not influence recovery," *Acta Biomaterialia* **9**(6), 6860-6866 (2013).

67. **C. T. Lim, E. H. Zhou, A. Li, S. R. K. Vedula, and H. X. Fu**, "Experimental techniques for single cell and single molecule biomechanics," *Materials Science and Engineering: C* **26**(8), 1278-1288 (2006).

68. **A. C. Lorenzo, and E. R. Caffarena**, "Elastic properties, Young's modulus determination and structural stability of the tropocollagen molecule: a computational study by steered molecular dynamics," *Journal of Biomechanics* **38**(7), 1527-1533 (2005).

69. **M. De Zee, F. Bojsen-Møller, and M. Voigt**, "Dynamic viscoelastic behavior of lower extremity tendons during simulated running," *Journal of Applied Physiology* **89**(4), 1352-1359 (2000).

70. **C. N. Maganaris, and J. P. Paul**, "In vivo human tendon mechanical properties," *J Physiol* **1**, 307-313 (1999).

71. **A. C. Devkota, and P. S. Weinhold**, "Mechanical response of tendon subsequent to ramp loading to varying strain limits," *Clinical Biomechanics* **18**(10), 969-974 (2003).

72. **M. J. Buehler**, "Hierarchical Nanomechanics of Collagen Fibrils: Atomistic and Molecular Modeling," in *Collagen: Structure and Mechanics* P. Fratzl, Ed., pp. 175-247, Springer US, Boston, MA (2008).

73. **J. Clemmer, J. Liao, D. Davis, M. F. Horstemeyer, and L. N. Williams**, "A mechanistic study for strain rate sensitivity of rabbit patellar tendon," *Journal of Biomechanics* **43**(14), 2785-2791 (2010).

74. **C.-Y. Huang, V. M. Wang, E. L. Flatow, and V. C. Mow**, "Temperature-dependent viscoelastic properties of the human supraspinatus tendon," *Journal of Biomechanics* **42**(4), 546-549 (2009).

75. **E. M. Spiesz, and P. K. Zysset**, "Structure–mechanics relationships in mineralized tendons," *Journal of the Mechanical Behavior of Biomedical Materials* **52**, 72-84 (2015).

76. **C. Vergari, P. Pourcelot, L. Holden, B. Ravary-Plumioën, G. Gerard, P. Laugier, D. Mitton, and N. Crevier-Denoix**, "True stress and Poisson's ratio of tendons during loading," *Journal of Biomechanics* **44**(4), 719-724 (2011).

77. **J. E. Sanders, and B. S. Goldstein**, "Collagen fibril diameters increase and fibril densities decrease in skin subjected to repetitive compressive and shear stresses," *Journal of Biomechanics* **34**(12), 1581-1587 (2001).

78. **P. P. Provenzano, and R. Vanderby Jr**, "Collagen fibril morphology and organization: Implications for force transmission in ligament and tendon," *Matrix Biology* **25**(2), 71-84 (2006).

79. **T. J. Wess**, "Collagen Fibrillar Structure and Hierarchies," in *Collagen: Structure and Mechanics* P. Fratzl, Ed., pp. 49-80, Springer US, Boston, MA (2008).

80. **C. W. Kolz, T. Suter, and H. B. Henninger**, "Regional mechanical properties of the long head of the biceps tendon," *Clinical Biomechanics* **30**(9), 940-945 (2015).

81. **H. S. Gupta**, "Nanoscale Deformation Mechanisms in Collagen," in *Collagen: Structure and Mechanics* P. Fratzl, Ed., pp. 155-173, Springer US, Boston, MA (2008).

82. **R. B. Svensson, T. Hassenkam, P. Hansen, M. Kjaer, and S. P. Magnusson**, "Tensile Force Transmission in Human Patellar Tendon Fascicles Is Not Mediated by Glycosaminoglycans," *Connective Tissue Research* **52**(5), 415-421 (2011).

83. **M. P. E. Wenger, L. Bozec, M. A. Horton, and P. Mesquida**, "Mechanical Properties of Collagen Fibrils," *Biophys J* **93**(4), 1255-1263 (2007).

84. **P. Moreira, N. Zemiti, C. Liu, and P. Poignet**, "Viscoelastic model based force control for soft tissue interaction and its application in physiological motion compensation," *Computer Methods and Programs in Biomedicine* **116**(2), 52-67 (2014).

85. **H. Delingette**, "Toward realistic soft-tissue modeling in medical simulation," *Proceedings of the IEEE* **86**(3), 512-523 (1998).

Chapter 8

86. **A. D. Lantada, and P. L. Morgado**, "Rapid prototyping for biomedical engineering: current capabilities and challenges," *Annual review of biomedical engineering* **14**, 73-96 (2012).

87. **P. Fratzl**, *Collagen: Structure and Mechanics*, Springer US (2008).

88. **R. Sopakayang, and R. De Vita**, "A mathematical model for creep, relaxation and strain stiffening in parallel-fibered collagenous tissues," *Medical engineering & physics* **33**(9), 1056-1063 (2011).

89. **T. J. Carter, M. Sermesant, D. M. Cash, D. C. Barratt, C. Tanner, and D. J. Hawkes**, "Application of soft tissue modelling to image-guided surgery," *Medical engineering & physics* **27**(10), 893-909 (2005).

90. **J. A. Weiss, J. C. Gardiner, and C. Bonifasi-Lista**, "Ligament material behavior is nonlinear, viscoelastic and rate-independent under shear loading," *Journal of Biomechanics* **35**(7), 943-950 (2002).

91. **B. Ahn, and J. Kim**, "Measurement and characterization of soft tissue behavior with surface deformation and force response under large deformations," *Medical Image Analysis* **14**(2), 138-148 (2010).

92. **K. Chino, and H. Takahashi**, "The association of muscle and tendon elasticity with passive joint stiffness: In vivo measurements using ultrasound shear wave elastography," *Clinical Biomechanics* **30**(10), 1230-1235 (2015).

93. **S. J. Obst, R. Newsham-West, and R. S. Barrett**, "In vivo measurement of human achilles tendon morphology using freehand 3-D ultrasound," *Ultrasound in medicine & biology* **40**(1), 62-70 (2014).

94. **C. Pierre-Jerome, V. Moncayo, and M. R. Terk**, "MRI of the Achilles tendon: A comprehensive review of the anatomy, biomechanics, and imaging of overuse tendinopathies," *Acta Radiologica* **51**(4), 438-454 (2010).

95. **P. Kälebo, L. Å. Goksör, L. Swärd, and L. Peterson**, "Soft-Tissue Radiography, Computed Tomography, and Ultrasonography of Partial Achilles Tendon Ruptures," *Acta Radiologica* **31**(6), 565-570 (1990).

96. **L. Fu, and M. Gu**, "Fibre-optic nonlinear optical microscopy and endoscopy," *Journal of microscopy* **226**(3), 195-206 (2007).

97. **M. A. Al-Rawhani, J. Beeley, and D. R. Cumming**, "Wireless fluorescence capsule for endoscopy using single photon-based detection," *Scientific reports* **5**, (2015).

98. **R. W. Boyd**, *Nonlinear Optics*, Elsevier Science (2008).

99. **D. B. Murphy**, *Fundamentals of Light Microscopy and Electronic Imaging*, Wiley (2002).

100. **P. Fratzl, K. Misof, I. Zizak, G. Rapp, H. Amenitsch, and S. Bernstorff**, "Fibrillar structure and mechanical properties of collagen," *Journal of structural biology* **122**(1), 119-122 (1998).

101. **B. d. C. Vidal**, "Image analysis of tendon helical superstructure using interference and polarized light microscopy," *Micron* **34**(8), 423-432 (2003).

102. **W. M. Petroll, H. D. Cavanagh, and J. V. Jester**, "Dynamic three-dimensional visualization of collagen matrix remodeling and cytoskeletal organization in living corneal fibroblasts," *Scanning* **26**(1), 1-10 (2004).

103. **K. M. Hanson, and C. J. Bardeen**, "Application of nonlinear optical microscopy for imaging skin," *Photochem Photobiol* **85**(1), 33-44 (2009).

104. **T. Verbiest, K. Clays, and V. Rodriguez**, *Second-order Nonlinear Optical Characterization Techniques: An Introduction*, CRC Press (2009).

105. **R. M. Williams, W. R. Zipfel, and W. W. Webb**, "Interpreting second-harmonic generation images of collagen I fibrils," *Biophys J* **88**(2), 1377-1386 (2005).

106. **P. J. Su, W. L. Chen, T. H. Li, C. K. Chou, T. H. Chen, Y. Y. Ho, C. H. Huang, S. J. Chang, Y. Y. Huang, H. S. Lee, and C. Y. Dong**, "The discrimination of type I and type II collagen and the label-free imaging of engineered cartilage tissue," *Biomaterials* **31**(36), 9415-9421 (2010).

107. **P. J. Su, W. L. Chen, Y. F. Chen, and C. Y. Dong**, "Determination of collagen nanostructure from second-order susceptibility tensor analysis," *Biophys J* **100**(8), 2053-2062 (2011).

108. **G. Cox, E. Kable, A. Jones, I. Fraser, F. Manconi, and M. D. Gorrell**, "3-dimensional imaging of collagen using second harmonic generation," *J Struct Biol* **141**(1), 53-62 (2003).

109. **I. Rocha-Mendoza, D. R. Yankelevich, M. Wang, K. M. Reiser, C. W. Frank, and A. Knoesen**, "Sum Frequency Vibrational Spectroscopy: The Molecular Origins of the Optical Second-Order Nonlinearity of Collagen," *Biophys J* **93**(12), 4433-4444 (2007).

110. **F. Tiaho, G. Recher, and D. Rouède**, "Estimation of helical angles of myosin and collagen by second harmonic generation imaging microscopy," *Optics Express* **15**(19), 12286-12295 (2007).

111. **W. H. Stoothoff, B. J. Bacskai, and B. T. Hyman**, "Monitoring Tau-Tubulin Interactions Utilizing Second Harmonic Generation in Living Neurons," *Journal of biomedical optics* **13**(6), 064039-064039 (2008).

112. **F. S. Pavone, and P. J. Campagnola**, *Second Harmonic Generation Imaging*, CRC Press, Boca Raton, London, NY (2013).

113. **P. J. Campagnola, A. C. Millard, M. Terasaki, P. E. Hoppe, C. J. Malone, and W. A. Mohler**, "Three-dimensional high-resolution second-harmonic generation imaging of endogenous structural proteins in biological tissues," *Biophys J* **82**(1), 493-508 (2002).

114. **A. Zoumi, A. Yeh, and B. J. Tromberg**, "Imaging cells and extracellular matrix in vivo by using second-harmonic generation and two-photon excited fluorescence," *Proceedings of the National Academy of Sciences* **99**(17), 11014-11019 (2002).

115. **W. R. Zipfel, R. M. Williams, R. Christie, A. Y. Nikitin, B. T. Hyman, and W. W. Webb**, "Live tissue intrinsic emission microscopy using multiphoton-excited native fluorescence and second harmonic generation," *Proceedings of the National Academy of Sciences* **100**(12), 7075-7080 (2003).

116. **Y. Wu, and J. Y. Qu**, "Two-photon autofluorescence spectroscopy and second-harmonic generation of epithelial tissue," *Opt Lett* **30**(22), 3045-3047 (2005).

117. **S. Zhuo, J. Chen, T. Luo, H. Chen, and J. Zhao**, "High-contrast multimodel nonlinear optical imaging of collagen and elastin," *Journal of Physics: Conference Series* 1476 (2007).

118. **V. Lutz, M. Sattler, S. Gallinat, H. Wenck, R. Poertner, and F. Fischer**, "Impact of collagen crosslinking on the second harmonic generation signal and the fluorescence lifetime of collagen autofluorescence," *Skin Research and Technology* **18**(2), 168-179 (2012).

119. **H. Liu, H. Liu, X. Deng, M. Chen, X. Han, W. Yan, and N. Wang**, "Raman spectroscopy combined with SHG gives a new perspective for rapid assessment of the collagen status in the healing of cutaneous wounds," *Analytical Methods* **8**(17), 3503-3510 (2016).

120. **Z. Liu, Z. A. Satira, X. Wang, X. Xu, X. Chen, K. Wong, S. Chen, J. Xin, and S. T. C. Wong**, "Fiber bundle based endomicroscopy prototype with two collection channels for simultaneous coherent anti-Stokes Raman scattering and second harmonic generation imaging," *Multiphoton Microscopy in the Biomedical Sciences XIV* **8948**, (2014).

121. **W. L. Chen, P. S. Hu, A. Ghazaryan, S. J. Chen, T. H. Tsai, and C. Y. Dong**, "Quantitative analysis of multiphoton excitation autofluorescence and second harmonic generation imaging for medical diagnosis," *Comput Med Imaging Graph* **36**(7), 519-526 (2012).

122. **A.-M. Pena, T. Boulesteix, T. Dartigalongue, and M.-C. Schanne-Klein**, "Chiroptical effects in the second harmonic signal of collagens I and IV," *Journal of the American Chemical Society* **127**(29), 10314-10322 (2005).

123. **S. Psilodimitrakopoulos, D. Artigas, G. Soria, I. Amat-Roldan, A. M. Planas, and P. Loza-Alvarez**, "Quantitative discrimination between endogenous SHG sources in mammalian tissue, based on their polarization response," *Optics Express* **17**(12), 10168-10176 (2009).

124. **I. Amat-Roldan, S. Psilodimitrakopoulos, P. Loza-Alvarez, and D. Artigas**, "Fast image analysis in polarization SHG microscopy," *Optics Express* **18**(16), 17209-17219 (2010).

Chapter 8

125. **C. G. Galbraith, and J. A. Galbraith**, "Super-resolution microscopy at a glance," *Journal of Cell Science* **124**(10), 1607-1611 (2011).

126. **T. S. Blacker, Z. F. Mann, J. E. Gale, M. Ziegler, A. J. Bain, G. Szabadkai, and M. R. Duchen**, "Separating NADH and NADPH fluorescence in live cells and tissues using FLIM," *Nat Commun* **5**, (2014).

127. **M. A. Yaseen, S. Sakadžić, W. Wu, W. Becker, K. A. Kasischke, and D. A. Boas**, "In vivo imaging of cerebral energy metabolism with two-photon fluorescence lifetime microscopy of NADH," *Biomedical optics express* **4**(2), 307-321 (2013).

128. **B. R. Masters, and P. So**, *Handbook of Biomedical Nonlinear Optical Microscopy*, Oxford University Press (2008).

129. **W. Becker**, *The Bh TCSPC Handbook*, Becker & Hickl (2014).

130. **J. Adur, G. Barbosa, V. Pelegati, M. Baratti, C. Cesar, V. Casco, and H. Carvalho**, "Multimodal and non-linear optical microscopy applications in reproductive biology," *Microscopy research and technique*, (2016).

131. **S. J. Baldwin, L. Kreplak, and J. M. Lee**, "Characterization via atomic force microscopy of discrete plasticity in collagen fibrils from mechanically overloaded tendons: Nano-scale structural changes mimic rope failure," *Journal of the Mechanical Behavior of Biomedical Materials* **60**, 356-366 (2016).

132. **S. J. Wilkinson, and D. W. L. Hukins**, "Determination of collagen fibril structure and orientation in connective tissues by X-ray diffraction," *Radiation Physics and Chemistry* **56**(1–2), 197-204 (1999).

133. **C. Boote, S. Hayes, S. Jones, A. J. Quantock, P. M. Hocking, C. F. Inglehearn, M. Ali, and K. M. Meek**, "Collagen organization in the chicken cornea and structural alterations in the retinopathy, globe enlarged (rge) phenotype—An X-ray diffraction study," *Journal of structural biology* **161**(1), 1-8 (2008).

134. **D. F. Holmes, H. K. Graham, J. A. Trotter, and K. E. Kadler**, "STEM/TEM studies of collagen fibril assembly," *Micron* **32**(3), 273-285 (2001).

135. **J. Janacek, M. Kreft, V. Cebasek, and I. Erzen**, "Correcting the axial shrinkage of skeletal muscle thick sections visualized by confocal microscopy," *J Microsc* **246**(2), 107-112 (2012).

136. **C. Oostendorp, P. J. Uijtdewilligen, E. M. Versteeg, T. G. Hafmans, E. H. van den Bogaard, P. K. de Jonge, A. Pirayesh, J. W. Von den Hoff, E. Reichmann, W. F. Daamen, and T. H. van Kuppevelt**, "Visualisation of newly synthesised collagen in vitro and in vivo," *Sci Rep* **6**(18780), (2016).

137. **E. Filova, F. Straka, T. Mirejovsky, J. Masin, and L. Bacakova**, "Tissue-engineered heart valves," *Physiol Res* **58**(2), S141-158 (2009).

138. **S. Murad, D. Grove, K. Lindberg, G. Reynolds, A. Sivarajah, and S. Pinnell**, "Regulation of collagen synthesis by ascorbic acid," *Proceedings of the National Academy of Sciences* **78**(5), 2879-2882 (1981).

139. **J. Du, J. J. Cullen, and G. R. Buettner**, "Ascorbic acid: Chemistry, biology and the treatment of cancer," *Biochimica et Biophysica Acta (BBA) - Reviews on Cancer* **1826**(2), 443-457 (2012).

140. **H. I. Roach, K. Hillier, and J. R. Shearer**, "Ascorbic acid requirements for collagen synthesis (proline hydroxylation) during long-term culture of embryonic chick femurs," *Biochimica et Biophysica Acta (BBA) - General Subjects* **842**(2), 139-145 (1985).

141. **L. Mardones, F. A. Zúñiga, M. Villagrán, K. Sotomayor, P. Mendoza, D. Escobar, M. González, V. Ormazabal, M. Maldonado, G. Oñate, C. Angulo, I. I. Concha, A. M. Reyes, J. G. Cárcamo, V. Barra, J. C. Vera, and C. I. Rivas**, "Essential role of intracellular glutathione in controlling ascorbic acid transporter expression and function in rat hepatocytes and hepatoma cells," *Free Radical Biology and Medicine* **52**(9), 1874-1887 (2012).

142. **L.-Å. Fransson, and K. Mani**, "Novel aspects of vitamin C: how important is glypican-1 recycling?," *Trends in Molecular Medicine* **13**(4), 143-149 (2007).

143. **S. R. Pinnell**, "Regulation of collagen biosynthesis by ascorbic acid: a review," *The Yale journal of biology and medicine* **58**(6), 553 (1985).

144. **K. E. Kubow, R. Vukmirovic, L. Zhe, E. Klotzsch, M. L. Smith, D. Gourdon, S. Luna, and V. Vogel**, "Mechanical forces regulate the interactions of fibronectin and collagen I in extracellular matrix," *Nature Communications* **6**, 8026 (2015).

145. **P. Bianchini, and A. Diaspro**, "Three-dimensional (3D) backward and forward second harmonic generation (SHG) microscopy of biological tissues," *Journal of Biophotonics* **1**(6), 443-450 (2008).

146. **P. J. Campagnola, and C. Y. Dong**, "Second harmonic generation microscopy: principles and applications to disease diagnosis," *Laser & Photonics Reviews* **5**(1), 13-26 (2011).

147. **A. Deniset-Besseau, J. Duboisset, E. Benichou, F. Hache, P.-F. Brevet, and M.-C. Schanne-Klein**, "Measurement of the Second-Order Hyperpolarizability of the Collagen Triple Helix and Determination of Its Physical Origin," *The Journal of Physical Chemistry B* **113**(40), 13437-13445 (2009).

148. **O. Frank, M. Heim, M. Jakob, A. Barbero, D. Schafer, I. Bendik, W. Dick, M. Heberer, and I. Martin**, "Real-time quantitative RT-PCR analysis of human bone marrow stromal cells during osteogenic differentiation in vitro," *J Cell Biochem* **85**(4), 737-746 (2002).

149. **L. Zhang, X. Ren, E. Alt, X. Bai, S. Huang, Z. Xu, P. M. Lynch, M. P. Moyer, X. F. Wen, and X. Wu**, "Chemoprevention of colorectal cancer by targeting APC-deficient cells for apoptosis," *Nature* **464**(7291), 1058-1061 (2010).

150. **M. W. Glynn, and A. K. McAllister**, "Immunocytochemistry and quantification of protein colocalization in cultured neurons," *Nature protocols* **1**(3), 1287-1296 (2006).

151. **J. S. Bonifacino, and R. Rojas**, "Retrograde transport from endosomes to the trans-Golgi network," *Nat Rev Mol Cell Biol* **7**(8), 568-579 (2006).

152. **E. G. Canty, and K. E. Kadler**, "Procollagen trafficking, processing and fibrillogenesis," *J Cell Sci* **118**(Pt 7), 1341-1353 (2005).

153. **P. Contard, L. Jacobs, J. S. Perlish, and R. Fleischmajer**, "Collagen fibrillogenesis in a three-dimensional fibroblast cell culture system," *Cell and Tissue Research* **273**(3), 571-575 (1993).

154. **M. F. Graham, A. Willey, J. Adams, D. Yager, and R. F. Diegelmann**, "Role of ascorbic acid in procollagen expression and secretion by human intestinal smooth muscle cells," *J Cell Physiol* **162**(2), 225-233 (1995).

155. **J. Bordeaux, A. W. Welsh, S. Agarwal, E. Killiam, M. T. Baquero, J. A. Hanna, V. K. Anagnostou, and D. L. Rimm**, "Antibody validation," *Biotechniques* **48**(3), 197 (2010).

156. **Y. Wu, D. S. Puperi, K. J. Grande-Allen, and J. L. West**, "Ascorbic acid promotes extracellular matrix deposition while preserving valve interstitial cell quiescence within 3D hydrogel scaffolds," *Journal of tissue engineering and regenerative medicine*, (2015).

157. **P. Stoller, K. M. Reiser, P. M. Celliers, and A. M. Rubenchik**, "Polarization-modulated second harmonic generation in collagen," *Biophys J* **82**(6), 3330-3342 (2002).

158. **C. Y. Park, J. K. Lee, and R. S. Chuck**, "Second Harmonic Generation Imaging Analysis of Collagen Arrangement in Human Cornea," *Investigative Ophthalmology & Visual Science* **56**(9), 5622-5629 (2015).

159. **V. Ntziachristos**, "Going deeper than microscopy: the optical imaging frontier in biology," *Nat Meth* **7**(8), 603-614 (2010).

160. **K. D. Micheva, and S. J. Smith**, "Array Tomography: A New Tool for Imaging the Molecular Architecture and Ultrastructure of Neural Circuits," *Neuron* **55**(1), 25-36 (2007).

161. **N. R. Melvin, and R. J. Sutherland**, "Quantitative Caveats of Standard Immunohistochemical Procedures: Implications for Optical Disector–based Designs," *Journal of Histochemistry and Cytochemistry* **58**(7), 577-584 (2010).

162. **G. Griffiths, B. Burke, and J. Lucocq**, *Fine Structure Immunocytochemistry*, Springer Berlin Heidelberg (2012).

163. **M. Strupler, A.-M. Pena, M. Hernest, P.-L. Tharaux, J.-L. Martin, E. Beaurepaire, and M.-C. Schanne-Klein**, "Second harmonic imaging and scoring of collagen in fibrotic tissues," *Optics Express* **15**(7), 4054-4065 (2007).

164. **H. S. Qian, S. M. Weldon, D. Matera, C. Lee, H. Yang, R. M. Fryer, A. B. Fogo, and G. A. Reinhart**, "Quantification and Comparison of Anti-Fibrotic Therapies by Polarized SRM and SHG-Based Morphometry in Rat UUO Model," *PLoS ONE* **11**(6), e0156734 (2016).

165. **K. A. Dorph-Petersen, J. R. Nyengaard, and H. J. Gundersen**, "Tissue shrinkage and unbiased stereological estimation of particle number and size," *J Microsc* **204**(Pt 3), 232-246 (2001).

166. **C. N. Carlo, and C. F. Stevens**, "Analysis of differential shrinkage in frozen brain sections and its implications for the use of guard zones in stereology," *J Comp Neurol* **519**(14), 2803-2810 (2011).

167. **A. Rachev, and S. E. Greenwald**, "Residual strains in conduit arteries," *Journal of Biomechanics* **36**(5), 661-670 (2003).

168. **J. P. Dickey, B. R. Hewlett, G. A. Dumas, and D. A. Bednar**, "Measuring Collagen Fiber Orientation: A Two-Dimensional Quantitative Macroscopic Technique," *Journal of Biomechanical Engineering* **120**(4), 537-540 (1998).

169. **S. Thomopoulos, J. P. Marquez, B. Weinberger, V. Birman, and G. M. Genin**, "Collagen fiber orientation at the tendon to bone insertion and its influence on stress concentrations," *Journal of Biomechanics* **39**(10), 1842-1851 (2006).

170. **W. J. Karlon, J. W. Covell, A. D. McCulloch, J. J. Hunter, and J. H. Omens**, "Automated measurement of myofiber disarray in transgenic mice with ventricular expression of ras," *The Anatomical Record* **252**(4), 612-625 (1998).

171. **T. Courtney, M. S. Sacks, J. Stankus, J. Guan, and W. R. Wagner**, "Design and analysis of tissue engineering scaffolds that mimic soft tissue mechanical anisotropy," *Biomaterials* **27**(19), 3631-3638 (2006).

172. **D. B. Thomason, O. Anderson, and V. Menon**, "Fractal analysis of cytoskeleton rearrangement in cardiac muscle during head-down tilt," *Journal of Applied Physiology* **81**(4), 1522-1527 (1996).

173. **C. Bayan, J. M. Levitt, E. Miller, D. Kaplan, and I. Georgakoudi**, "Fully automated, quantitative, noninvasive assessment of collagen fiber content and

organization in thick collagen gels," *Journal of applied physics* **105**(10), 102042 (2009).

174. **M. Sivaguru, S. Durgam, R. Ambekar, D. Luedtke, G. Fried, A. Stewart, and K. C. Toussaint**, "Quantitative analysis of collagen fiber organization in injured tendons using Fourier transform-second harmonic generation imaging," *Optics Express* **18**(24), 24983-24993 (2010).
175. **O. S. Osman, J. L. Selway, P. E. Harikumar, C. J. Stocker, E. T. Wargent, M. A. Cawthorne, S. Jassim, and K. Langlands**, "A novel method to assess collagen architecture in skin," *BMC Bioinformatics* **14**(1), 1-10 (2013).
176. **G. Castellano, L. Bonilha, L. M. Li, and F. Cendes**, "Texture analysis of medical images," *Clinical Radiology* **59**(12), 1061-1069 (2004).
177. **K. E. Frisch, S. E. Duenwald-Kuehl, R. S. Lakes, and R. Vanderby**, "Quantification of Collagen Organization Using Fractal Dimensions and Fourier Transforms," *Acta Histochemica* **114**(2), 140-144 (2012).
178. **M. Varga**, *Textbook of Rabbit Medicine*, Elsevier Health Sciences UK (2013).
179. **L. M. Houdebine, and J. Fan**, *Rabbit Biotechnology: Rabbit genomics, transgenesis, cloning and models*, Springer Netherlands (2009).
180. **B. Jähne**, *Digital Image Processing*, Springer, Berlin Heidelberg New York (2005).
181. **P. Soille**, *Morphological Image Analysis: Principles and Applications*, Springer Berlin Heidelberg (2013).
182. **T. D. Little**, *The Oxford Handbook of Quantitative Methods, Vol. 2: Statistical Analysis*, Oxford University Press, Oxford, New York (2013).
183. **F. Cacho, P. J. Elbischger, J. F. Rodríguez, M. Doblaré, and G. A. Holzapfel**, "A constitutive model for fibrous tissues considering collagen fiber crimp," *International Journal of Non-Linear Mechanics* **42**(2), 391-402 (2007).
184. **M. Sacks**, "Biaxial Mechanical Evaluation of Planar Biological Materials," *Journal of elasticity and the physical science of solids* **61**(1-3), 199-246 (2000).
185. **Y. Isobe, T. Kosaka, G. Kuwahara, H. Mikami, T. Saku, and S. Kodama**, "Oriented collagen scaffolds for tissue engineering," *Materials* **5**(3), 501-511 (2012).

186. **J. H. Gillard, A. D. Waldman, and P. B. Barker**, *Clinical MR Neuroimaging: Physiological and Functional Techniques*, Cambridge University Press (2009).

187. **T. Peeters, A. Vilanova, G. Strijkers, and B. ter Haar Romeny**, "Visualization of the fibrous structure of the heart," *Vision, Modeling and Visualization* 309-316 (2006).

188. **E. Maeda, J. C. Shelton, D. L. Bader, and D. A. Lee**, "Time dependence of cyclic tensile strain on collagen production in tendon fascicles," *Biochemical and Biophysical Research Communications* **362**(2), 399-404 (2007).

189. **A. Herchenhan, N. S. Kalson, D. F. Holmes, P. Hill, K. E. Kadler, and L. Margetts**, "Tenocyte contraction induces crimp formation in tendon-like tissue," *Biomech Model Mechanobiol* **11**(3-4), 449-459 (2012).

190. **M. Franchi, V. Ottani, R. Stagni, and A. Ruggeri**, "Tendon and ligament fibrillar crimps give rise to left-handed helices of collagen fibrils in both planar and helical crimps," *Journal of Anatomy* **216**(3), 301-309 (2010).

191. **M. Raspanti, A. Manelli, M. Franchi, and A. Ruggeri**, "The 3D structure of crimps in the rat Achilles tendon," *Matrix Biology* **24**(7), 503-507 (2005).

192. **J. C. Patterson-Kane, E. C. Firth, A. E. Goodship, and D. A. Parry**, "Age-related differences in collagen crimp patterns in the superficial digital flexor tendon core region of untrained horses," *Aust Vet J* **75**(1), 39-44 (1997).

193. **A. D. Freed, and T. C. Doehring**, "Elastic model for crimped collagen fibrils," *Journal of Biomechanical Engineering* **127**(4), 587-593 (2005).

194. **R. Paesen**, "Model development for image analysis in second harmonic imaging microscopy," *PhD thesis* Hasselt University (2016)

195. **E. Blain, Y. Zhang, D. Aeschlimann, B. Caterson, and V. Duance**, "Changes in tendon extracellular matrix composition with age," *International Journal of Experimental Pathology* **85**(1), A33-A34 (2004).

196. **S. Rigozzi, R. Muller, and J. G. Snedeker**, "Local strain measurement reveals a varied regional dependence of tensile tendon mechanics on glycosaminoglycan content," *Journal of Biomechanics* **42**(10), 1547-1552 (2009).

197. **M. R. Dressler, D. L. Butler, and G. P. Boivin**, "Age-related changes in the biomechanics of healing patellar tendon," *Journal of Biomechanics* **39**(12), 2205-2212 (2006).

198. **V. L. A. Trindade, P. A. L. S. Martins, S. Santos, M. P. L. Parente, R. M. Natal Jorge, A. Santos, L. Santos, and J. M. Fernandes**, "Experimental study of the influence of senescence in the biomechanical properties of the temporal tendon and deep temporal fascia based on uniaxial tension tests," *Journal of Biomechanics* **45**(1), 199-201 (2012).

199. **J. Diamant, A. Keller, E. Baer, M. Litt, and R. G. C. Arridge**, "Collagen; Ultrastructure and Its Relation to Mechanical Properties as a Function of Ageing," *Proceedings of the Royal Society of London. Series B. Biological Sciences* **180**(1060), 293-315 (1972).

200. **K. A. Hansen, J. A. Weiss, and J. K. Barton**, "Recruitment of tendon crimp with applied tensile strain," *Journal of Biomechanics Eng* **124**(1), 72-77 (2002).

201. **S. Psilodimitrakopoulos, S. I. C. O. Santos, I. Amat-Roldan, A. K. N. Thayil, D. Artigas, and P. Loza-Alvarez**, "In vivo, pixel-resolution mapping of thick filaments' orientation in nonfibrilar muscle using polarization-sensitive second harmonic generation microscopy," *Journal of biomedical optics* **14**(1), 014001 (2009).

202. **X. Chen, O. Nadiarynkh, S. Plotnikov, and P. J. Campagnola**, "Second harmonic generation microscopy for quantitative analysis of collagen fibrillar structure," *Nat. Protocols* **7**(4), 654-669 (2012).

203. **M. Y. Berezin, and S. Achilefu**, "Fluorescence Lifetime Measurements and Biological Imaging," *Chemical reviews* **110**(5), 2641-2684 (2010).

204. **A. Ehlers, I. Riemann, T. Anhut, M. Kaatz, P. Elsner, and K. König**, "Fluorescence lifetime imaging of human skin and hair," *Proc. of SPIE Vol* 60890N-60891 (2006).

205. **B. T. Haraldsson, P. Aagaard, M. Krogsgaard, T. Alkjaer, M. Kjaer, and S. P. Magnusson**, "Region-specific mechanical properties of the human patella tendon," *Journal of Applied Physiology* **98**(3), 1006-1012 (2005).

206. **K. Vilendrer, K. Grimes, J. Shukla, D. Strei, C. Eriksen, and T. Nickel**, "Thermo-electric grip for holding soft tissue," Google Patents (2003)

207. **J. Hashemi, N. Chandrashekar, and J. Slauterbeck**, "The mechanical properties of the human patellar tendon are correlated to its mass density and are independent of sex," *Clinical Biomechanics* **20**(6), 645-652 (2005).

208. **N. Juncosa, J. R. West, M. T. Galloway, G. P. Boivin, and D. L. Butler**, "In vivo forces used to develop design parameters for tissue engineered implants for rabbit patellar tendon repair," *Jurnal of Biomechanics* **36**(4), 483-488 (2003).

209. **M. Franchi, M. Fini, M. Quaranta, V. De Pasquale, M. Raspanti, G. Giavaresi, V. Ottani, and A. Ruggeri**, "Crimp morphology in relaxed and stretched rat Achilles tendon," *Journal of Anatomy* **210**(1), 1-7 (2007).

210. **J. Leppilahti, J. Puranen, and S. Orava**, "Incidence of Achilles tendon rupture," *Acta Orthopaedica Scandinavica* **67**(3), 277-279 (1996).

211. **F. D'Amico, E. Skarmoutsou, and F. Stivala**, "State of the art in antigen retrieval for immunohistochemistry," *Journal of Immunological Methods* **341**(1–2), 1-18 (2009).

212. **M. C. Rousselet, S. Michalak, F. Dupre, A. Croue, P. Bedossa, J. P. Saint-Andre, and P. Cales**, "Sources of variability in histological scoring of chronic viral hepatitis," *Hepatology* **41**(2), 257-264 (2005).

213. **N. Schmitz, S. Laverty, V. B. Kraus, and T. Aigner**, "Basic methods in histopathology of joint tissues," *Osteoarthritis and Cartilage* **18**, S113-S116 (2010).

References

Chapter 9

9 Curriculum vitae

9.1 Academic qualification

Master's degree	**Optomechanics** Department of Instrumentation and Control Engineering, Faculty of Mechanical Engineering, Czech Technical University, Prague, CR
Master thesis	*Design and realization of the instrument for civil samples measurement in climatic chamber.*
Bachelor's degree	**Theoretical fundamentals of mechanical engineering** Faculty of Mechanical Engineering, Czech Technical University, Prague, CR
Bachelor thesis	*Mechanical properties of vena saphena magna.*
Master's degree	**Sport Sciences** Faculty of Education and Sport, Charles University, Prague, CR
Master thesis	*Behavioural analysis of football coaches within a training session throughout different performance levels in adult category.*
Scholarship	*Including one year scholarship at Brunel University, London, UK.*

9.2 Academic experience

2011 - 2017	**Department of Biomathematics** Institute of Physiology, Czech Academy of Sciences, Prague, CR
Position	*Data processing and analysis, operating and upgrading light microscopes under Czech BioImaging facility (Leica/Nikon/Zeiss), designing experiments in microscopy (gSTED, SHG, PSHG, FLIM, PLIM, etc.).*
2010 - 2017	**Department of Biomaterials and Tissue Engineering** Institute of Physiology, Czech Academy of Sciences, Prague, CR
Position	*Statistics, correlative biomechanical testing of native and artificial materials, for example, PLA nanofibrous mats.*
2015 - 2017	**Department of Designing and Machine Components** Faculty of Mechanical Engineering, Czech Technical University, Prague, CR
Position	*Designing and computing tasks within the ATLAS – CERN ITk co-operation projects.*

Chapter 9

9.3 Selected publications

M. Bacakova, J. Pajorova, D. Stranska, **D. Hadraba**, et al., "Protein nanocoatings on synthetic polymeric nanofibrous membranes designed as carriers for skin cells," *International Journal of Nanomedicine* (accepted for publication in 12/2016).

M. Ostadal, J. Liskova, **D. Hadraba**, A. Eckhardt, "Possible Pathogenetic Mechanisms and New Therapeutic Approaches of Pes Equinovarus," *Physiological Research.* (accepted for publication in 12/2016).

J. Liskova, O. Babchenko, M. Varga, A. Kromka, **D. Hadraba**, et al., "Osteogenic cell differentiation on H-terminated and O-terminated nanocrystalline diamond films," *International Journal of Nanomedicine*, **10**, 869-84 (2015).

M. Bacakova, F. Lopot, **D. Hadraba**, et al., "Effects of fiber density and plasma modification of nanofibrous membranes on the adhesion and growth of HaCaT keratinocytes," *Journal of Biomaterials Applications* **29**(6), 837-53 (2015).

K. Novotna, M. Zajdlova, T. Suchy, **D. Hadraba**, et al., "Polylactide nanofibers with hydroxyapatite as growth substrates for osteoblast-like cells," *J Biomed Mater Res A.* **102**(11), 3918-30 (2014).

O. Fanta, **D. Hadraba**, F. Lopot, et al., "Pre-activation and muscle activity during frontal impact in relation to whiplash associated disorders," *Neuroendocrynology Letters* **34**(7), 708-16 (2013).

J. Vesely, **D. Hadraba**, H. Chlup, et al., "Constitutive Modelling and Histology of Vena Saphena," *Applied Mechanics and Materials* **465**, 249 - 254 (2013).

O. Fanta, J. Boucek, **D. Hadraba**, K. Jelen, "Influence of the front part of the vehicle and cyclist's sitting position on the severity of head injury in side collision," *Acta of Bioengineering and Biomechanics* **15**(1), 105-12 (2013).

D. Hadraba, "The effect of mechanical loading of hypokinesia on the structures of the extracellular matrix and functional changes in soft tissues," in K. Jelen, et al., *Biomechanical*

reflection of human hypokinetic stress and its identificators, Karolinum, , Chapter 2.3 (2013), ISBN 9788024621821.

K. Jelen, F. Lopot, **D. Hadraba**, H. Herman, M. Lopotova, "The Women's Pelvic Floor Biomechanics," in: Injury and Skeletal Biomechanics, (2012). ISBN: 9789535106906.

K. Jelen, O. Fanta, R. Billich, **D. Hadraba**, P. Kubovy, "Whiplash Injury and Head Injury Criterion during Deceleration," *Transactions on Transport Sciences* **4**(4), 217-224 (2011).

9.4 Selected academic conferences

2016	**MECAHITECH** Bucharest, Romania
Oral presentation	*Design and realization of the instrument for measuring building material deformation in environmental chamber.*
2015	**Photonex, Nano-Spectroscopy & Bio-Imaging** Coventry, UK
Flash presentation	*Biomechanics and label-free imaging of connective tissue.*
2014	**18th International Microscopy Congress** Prague, CR
Poster presentation	*The response of nanofibrous PLA mats to mechanical stress.*
2013	**Focus on Microscopy** Maastricht, Netherlands
Oral presentation	*Label free optical methods for evaluation of mechanically exposed proteins in vein.*

Chapter 9

9.5 Selected academic courses and short-term stay

2016	**Hyperspectral Imaging - Short-term Stay** Department of Tissue Engineering & Biophotonics King's College London, London, UK
2016	**11th Workshop on Advanced Multiphoton and Fluorescence Lifetime Imaging** Prague, CR
2014	**Transmission electron microscopy in life sciences** Prague, CR
2012	**Image acquisition and processing in biomedical microscopy** Prague, CR

9.6 Selected Grant Projects in Co-operation

956213	**Grant Agency of Charles University (main proposer)**
Topic	*The building proteins of the extracellular matrix detected by the microscopic and rheological methods.*
17-11898S	**Grant Agency of the Czech Republic**
Topic	*Nanosecond electric pulses for modulation of microtubule dynamics.*
P108/12/G108	**Grant Agency of the Czech Republic - Center of Excellence**
Topic	*Preparation, modification and characterization of materials by radiation.*